THESIS WORK FOR DUAL MASTER'S DEGREE

KIT   M.Sc. in Mechanical Engineering
ITBA   Mag. in Energy and Environment

INVESTIGATION OF A NOVEL COMPRESSION CONCEPT FOR FUEL CELL STACKS

Daniel Weis, B. Eng.
Mechanical Engineering - KIT

Tutor
Dr.-Ing. Jan Haußmann KIT/ IPEK

Co-Tutor
Jamil Kharrat, M. Sc. KIT/ IPEK
Philip Müller-Welt, M. Sc. KIT/ IPEK

Examiners
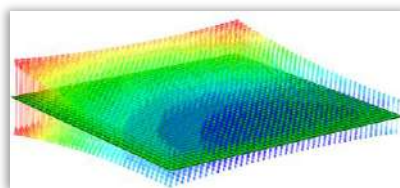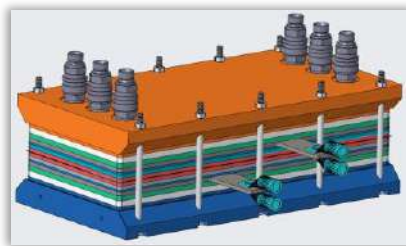Univ.-Prof. Dr.-Ing. Dr. h. c. Albert Albers KIT/ IPEK
Prof. Dr.-Ing. Robert Stieglitz KIT/ ITES

Karlsruhe
17/07/2023

Master Thesis

Investigation of a Novel Compression Concept for PEM Fuel Cell Stacks

Untersuchung eines neuartigen Verpressungskonzepts für PEM-Brennstoffzellen-Stacks

Daniel Weis, B. Eng.

Supervisor: Univ.-Prof. Dr.-Ing. Dr. h. c. Albert Albers
Co-Supervisor: Dr.-Ing. Jan Haußmann
Jamil Kharrat, M. Sc.
Philip Müller-Welt, M. Sc.

No.: 4634
Karlsruhe, July 2023

Master Thesis

Mr. Daniel Weis, B. Eng.

(Matr.-No.: 2399113)

Investigation of a Novel Compression Concept for PEM Fuel Cell Stacks

The master's thesis is to be prepared in close contact with the institute. Third-party inspection may only take place after consultation with the institute.

Issue Date: 16.01.2023   Due Date: 17.07.2023

Supervisor: Co-Supervisor:

_____   _____
(Univ.-Prof. Dr.-Ing. Dr. h. c. Albert Albers)   (Dr.-Ing. Jan Haußmann)

Author: Address:

_____   Place   76137 Karlsruhe
(Daniel Weis, B. Eng.)   Street   Winterstr. 29
                                          Phone   +49 176 81511329

Master Thesis

Task Description

for

Mr. Daniel Weis, B. Eng.

(Matr.-No.: 2399113)

Investigation of a Novel Compression Concept for PEM Fuel Cell Stacks

Within the scope of this master thesis, a compression concept of an industrial partner shall be transferred to the KIT-IPEK- fuel cell and investigated through a holistic FEM analysis.

In addition to the consideration of different spring concepts, the focus is on the analysis of the effects on the gas diffusion layer and the gaskets in the fuel cell stack.

This first requires investigations into the basic modelling of the stack and then simulative comparisons of different concepts.

The findings will then be used for specific compression settings of the test specimen to determine the optimum operating conditions in terms of power density and service life of the fuel cell.

Supervisor:	Univ.-Prof. Dr.-Ing. Dr. h. c. Albert Albers
Co-Supervisor:	Dr.-Ing. Jan Haußmann
	Jamil Kharrat, M. Sc.
	Philip Müller-Welt, M. Sc.

Declaration

I hereby certify that I have prepared this thesis independently and only with the sources and aids indicated in the bibliography.

Karlsruhe, 17th July 2023

Kurzfassung

Die Verwendung von Wasserstoff in Brennstoffzellen gewinnt aufgrund des Bedarfs an emissionsarmen Alternativen in verschiedenen technischen Bereichen immer mehr an Bedeutung. Der Schwerpunkt dieser Arbeit liegt auf der Polymerelektrolytmembran-Brennstoffzelle. Ein Parameter zur Reduzierung der Leistungsverluste ist der Anpressdruck zwischen der Bipolarplatte und der Gasdiffusionsschicht. Er wird zum einen durch die Montagekraft und zum anderen durch das Anschwellen der Membran während des Betriebs beeinflusst, welches durch Temperatur- und Feuchtigkeitsänderungen verursacht wird. Um die Verteilung des Anpressdrucks über der aktiven Fläche zu verbessern und dessen Anstieg während des Betriebs gering zu halten, wird ein neuartiges Kompressionskonzept vorgeschlagen und in einer FEM-Analyse untersucht. Verschiedene Federvarianten werden miteinander und mit der Referenz, einem Tellerfederpaket auf Zugstangen, verglichen. Die Ergebnisse zeigen, dass durch ein Konzept mit 15 kleinen Federn, bei dem der Kraftfluss an verschiedenen Stellen des Stacks in die Endplatte eintritt, eine gleichmäßige Spannungsverteilung erreicht werden kann. Der hohe Anpressdruck an den Rändern der aktiven Fläche kann durch eine geringere Durchbiegung der Endplatte reduziert werden. Dies wird erreicht, indem die Federn näher zueinander positioniert werden, so dass die inneren Federn einander berühren. Es ist eine Differenz von 0,2-0,4 MPa zwischen minimaler und maximaler Spannung entlang eines Pfades im Querschnitt erreichbar und von 0,9-1,3 MPa entlang des Längsschnitts. Es wird festgestellt, dass der Spannungsanstieg von der Montage bis zum Betrieb von der Federcharakteristik abhängt. Der maximale Anstieg am Rand der aktiven Fläche kann auf 1,7 MPa reduziert werden, und der geringste Spannungsanstieg in der Mitte der aktiven Fläche beträgt etwa 0,5 MPa. Die vorgeschlagenen Konzepte zeigen bessere Ergebnisse als die Tellerfeder-Referenz mit einer guten Spannungsverteilung. Obwohl der Spannungsanstieg bei den vorgeschlagenen Konzepten ebenfalls besser ist als beim Tellerfederpaket, ist der Wert noch nicht zufriedenstellend, da er die Porosität der GDL im Betrieb stark beeinflusst. Das vielversprechendste Federkonzept wird experimentell getestet. Die experimentellen Ergebnisse zeigen eine qualitative Übereinstimmung mit den Simulationsergebnissen.

Abstract

The usage of hydrogen in fuel cells gains more and more importance due to the need for emission-low alternatives in various technical areas. The focus of this work lies on the polymer electrolyte membrane fuel cell. One parameter to reduce performance losses is the contact pressure between the bipolar plate and the gas diffusion layer. It is influenced by first the assembly force and second the swelling of the membrane during operation which is caused by changes in temperature and humidity. To improve the stress distribution and to keep the stress increase during operation low, a novel compression concept is proposed and investigated in an FEM analysis. Different variants of springs are compared to each other and to the reference, a disc spring stack on tie rods. The results show that an even stress distribution is achievable through a concept with 15 small springs where the force flow enters the end plate at various points over the stack. High contact pressure at the edges of the active area can be reduced by reducing the end plate bending. This is achieved by moving the springs closer together so that the inner springs touch each other. A difference between minimum and maximum stress along one path in the cross-section of 0.2-0.4 MPa is achievable and of 0.9-1.3 MPa along the longitudinal section. It is found that the stress increase from assembly to operation depends on the spring characteristic. The maximum increase at the edge of the active area can be reduced to 1.7 MPa, and the smallest stress increase in the centre of the active area is around 0.5 MPa. The proposed concepts show better results than the disc spring reference with a good stress distribution. Although the stress increase in the proposed concepts is also better than in the disc spring stack the value is not yet satisfactory because it strongly influences the porosity of the GDL during operation. The most promising spring concept is tested experimentally. The experimental results show a qualitative accordance with the simulation.

Table of Contents

1   Introduction and motivation

The consistent rising of the world population leads to a constant growth of energy demand through technological development [1]. Carbon-based energy sources such as coal, oil and gas still account for a large proportion of energy production [1]. During their combustion, carbon dioxide is produced which accelerates the greenhouse effect. Up to a certain level, the greenhouse effect is necessary for life but a too-strong effect causes damage to natural global systems [1]. Switching to a low-carbon energy carrier like hydrogen from renewable energies could be a lever to reduce further emissions.

With the German government declaring to become a leading nation in hydrogen technology [2] as well as the European Union establishing a hydrogen strategy [3] in the background of the Green Deal [4] the hydrogen topic is coming to a new public and technical attention. Production, transport, usage and regulation of everything connected to hydrogen are central topics. The key factor in the area of usage is the fuel cell. Mobile applications find their place for example in the automotive sector whereas a stationary application could be a combined heat and power production [5]. The focus of both research and industry is currently the Polymer Electrolyte Membrane Fuel Cell (PEMFC) which will be introduced and explained in the following chapter. Considering only the device itself one advantage is the high efficiency in comparison to the internal combustion engine. This depends on different areas like the point of operation, also the gas flow of the reactants, the heat flux through the inner parts, pressure and temperature during the operation, electrical resistance, humidity and more [1]. More advantages are the emission poor and the low noise operation [1, 5, 6]. The only emission is water which is produced in the reaction between hydrogen and oxygen. The noise is very low because it is a catalytical reaction instead of a combustion and there are basically no moved parts in comparison to the combustion engine [1].

The focus area of this master thesis is the fuel cell stack and the dependency of the performance on the assembly process. To achieve the high efficiency an important aspect during the assembly of the fuel cell stack is the contact pressure between the parts. The contact pressure is defined on one hand by the assembly force during the stack mounting but on the other hand also by the conditions during the operation [7]. The first is controllable and configurable, the effect of the latter can only be influenced indirectly because the conditions change continually during the usage period.

Regarding the assembly force, a compromise needs to be found because it influences the electrical resistance and the gas flow at the same time [8]. The electrical resistance depends on firstly the material and its electrical conductivity, but also, and for the context more important, the contact or contact pressure between the different parts inside the stack [7], especially since the stack consists of different material layers. With a high compression force, low contact resistance is achieved. At the same time the gas diffusion layer, a porous part inside each cell responsible for the distribution of the gases, can be damaged if the assembly force is too high [8]. If it is compressed too much the gases don't reach the electrodes any more so that the reaction rate and thereby the performance decreases.

Concerning the changes in ambient conditions the for the current task most important ones are changes in temperature and humidity which lead to a swelling of the membrane, thus of the fuel cell stack [9, 10]. This swelling induces a change of contact pressure, hence a change in efficiency. To be able to run the fuel cell in an efficient point of operation the swelling needs to be compensated. The task of the given master thesis is a development of a new compression concept with springs for this very purpose to be able to keep a high performance. The development is happening in collaboration with an industrial partner who is developing and producing springs. The aim of the task is to model a fuel cell stack in a simulation software to try different concepts and compare them to a typical solution used in current processes. After the analysis of the simulation results, an experimental setup should be built to validate the simulation of the most promising concepts.

The written documentation is structured following the task. After giving some basic information about the PEM fuel cell and the state-of-the-art regarding the problem, the simulation with its presuppositions is presented and discussed as well as experimental results. Finally, a conclusion is drawn leading to further possible investigations.

2 Basics of the PEM fuel cell

To understand the origin of the problem and the necessity of the given thesis the function of the observed fuel cell will be shortly explained. With the PEM fuel cell working between 80 and 120 °C it belongs to the low-temperature fuel cells [11]. In this chapter, first, the general functionality is explained, later some relevant components and finally the assembly process and parameters that affect the performance.

2.1 Fundamentals and function

Very generally speaking, a fuel cell is a device to convert chemical energy into electrical energy. In addition to electricity water is generated and heat is produced as a waste product. To understand the electrochemical process, a schematic sketch of a cell is shown in Figure 2.1.
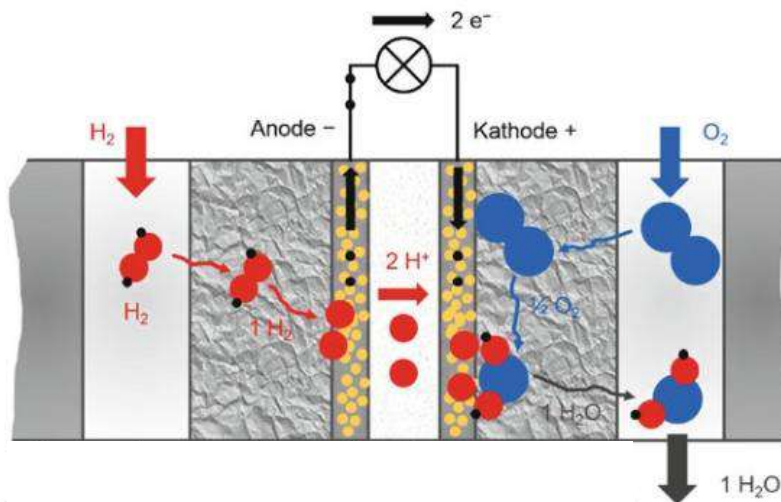

Figure 2.1: Sketch of single PEM fuel cell [1]

On one side, the anode, hydrogen is supplied, on the cathode side oxygen or in most cases air. Oxidation is happening on the anode side, leading to the following reaction:

$$H_2 \rightarrow 2H^+ + 2e^- \hspace{3cm} 2.1$$

The positive hydrogen ions cross the membrane to the cathode side whereas the negative electrons are conducted through the external circuit. Reaching the cathode side, a reduction is taking place:

$$\frac{1}{2}O_2 + 2e^- \rightarrow O^{2-}$$

<div align="right">2.2</div>

If ambient air is used, the nitrogen also enters the fuel cell but does not take part in the reaction. As a complete reaction, the two equations can be summed up:

$$H_2 + \frac{1}{2}O_2 \rightarrow H_2O$$

<div align="right">2.3</div>
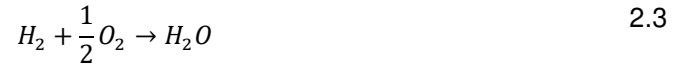
Due to the electrical isolation between the anode and cathode, there is a maximum electrical potential of 1.23 V per cell [11]. Up to a few hundred single cells are assembled in series to reach a high potential and high performance. The whole system contains next to the stack the power electronics to control the whole system and the Balance of plant consisting of elements like an air compressor, filter, tank or recirculation pump [11].

A typical stack design is shown in Figure 2.2. The stack consists of many single cells. One cell consists of one half of a Bipolar Plate (BPP) on each side, two gaskets and the Membrane Electrode Assembly (MEA) unit in the centre. The MEA is made of two Gas Diffusion Layers (GDL), two Catalyst Layers and the membrane as the core. Depending on design and material choice one single cell of an industrial fuel cell stack has a thickness between 0.8 and 1.6 mm. The maximum power can reach a few hundred kilowatts, depending on the size of the stack [6, 11].
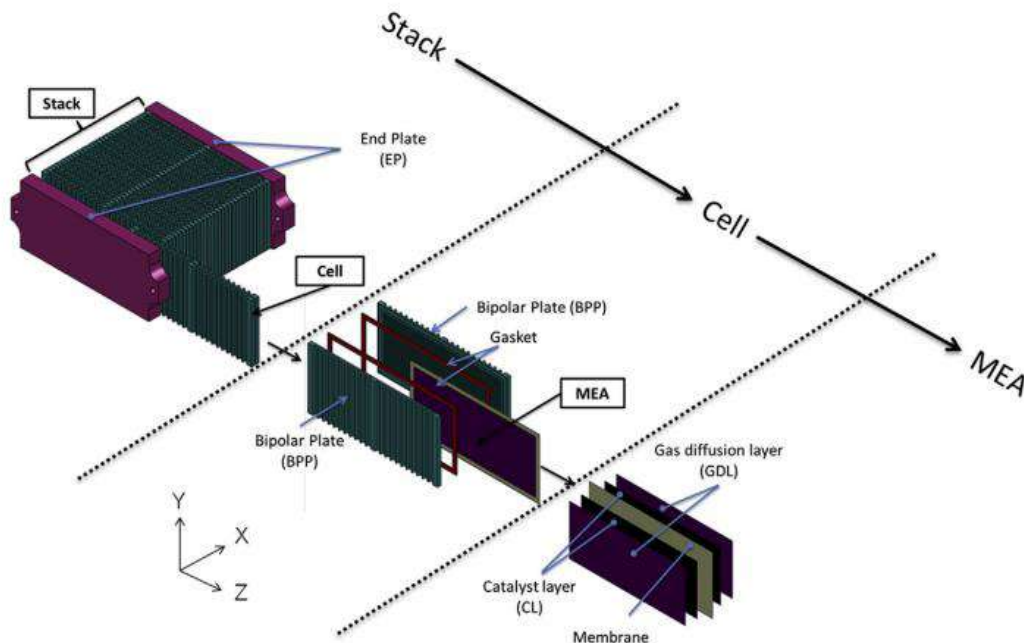

Figure 2.2: Different stack components [12]

To describe the operational behaviour of a cell it is common to use a polarization curve to plot voltage versus current or current density. A typical curve is shown in Figure 2.3.
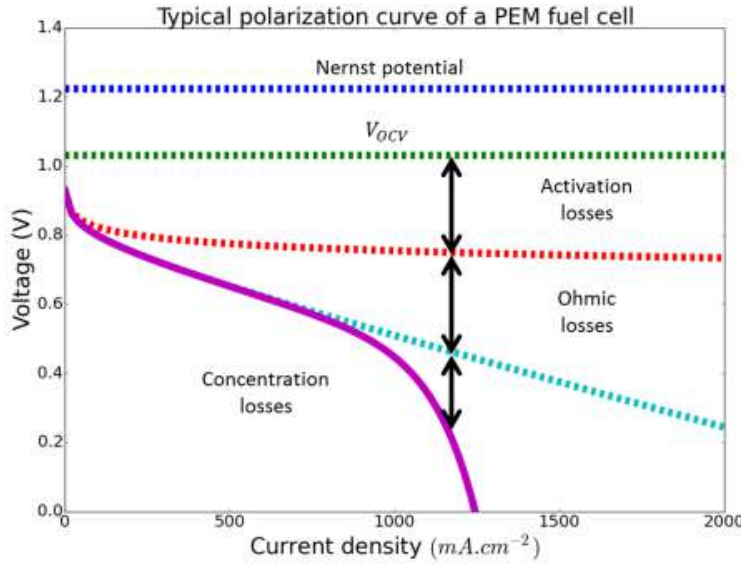

Figure 2.3: Polarization curve [13]

The reversible cell voltage of 1.23 V per cell is calculated through the free reaction enthalpy of the reaction of hydrogen with oxygen, the number of electrons per reaction and the Faraday constant [1].

$$E^0 = \frac{\Delta_R G_m^0}{z \cdot F} = \frac{237.13 \cdot 10^3 \frac{J}{mol}}{2 \cdot 96\,485 \frac{As}{mol}} = 1.23\ V$$

<div align="right">2.4</div>

This value is not achievable in practice because of diffusion losses from hydrogen migrating from anode to cathode through the membrane, electrons which are conducted through the membrane because it is not a perfect isolator or other side reactions [1]. The measurable open circuit voltage lies around 1 V and is decreasing in a non-linear way with increasing current density. The highest achievable current is present in the event of a short circuit with the voltage decreasing to 0 V. The losses leading to the voltage decrease contain next to the diffusion losses also activation, ohmic and concentration losses [14].

$$V_{irrev} = \eta_{diff} + \eta_{act} + \eta_{ohmic} + \eta_{conc}$$

<div align="right">2.5</div>

Activation losses result from the necessary activation energy and the limited reaction rate happening at the electrodes. Mainly the oxygen on the cathode side is responsible

for the losses because the reaction is slower than the hydrogen reaction on the anode [1, 14].

The ohmic losses are composed of resistance from electron conduction and ion conduction. The ionic conductivity is defined by the membrane because the ability of the protons to pass it is influenced by the thickness and the humidity of the membrane. The electronic conductivity depends on the materials of electron-conducting parts i.e., the bipolar plate, the gas diffusion layer and the catalyst layer and their interfacial connection especially between the GDL and the BPP [14]. With respect to the topic of the master thesis, the interfacial contact and thereby the ohmic losses can be influenced through the assembly force with a high force leading to less ohmic losses because GDL and BPP come better into contact.

The concentration losses dominate at high current densities when the demand for gas supply increases strongly. The feed of the gases happens too slowly to maintain the high current because the availability of hydrogen and oxygen through the gas diffusion layer (GDL) depends on diffusion [1]. If the supply is not high enough the reaction rate decreases and the voltage drops. Concentration losses can also occur when the stack is overly compressed since the porosity of the GDL is reduced drastically which is important to bear in mind with respect to the assembly force. This hinders diffusion as well and leads to a drop in performance [7].

To understand the interaction of the individual parts, the single components of the fuel cell stack and their functions are described in the following subchapters.

2.2   Components

The components of the single cell are described with their functions, typical materials and properties. The most important are the MEA, the BPP and the non-repetitive units at the end of the stack.

2.2.1   Membrane Electrode Assembly

The membrane electrode assembly (MEA) is the core of each cell, where the chemical reaction is happening. In the centre is the membrane which has the task of electrical isolation, separating the gases from each other and conducting protons from the anode to the cathode side [11, 15]. It is normally made of perfluorosulfonic acid (PFSA) which is commonly known by its trade name Nafion®. Further necessary properties are the chemical and thermal stability since it is operating in an acid environment at around 80 – 100 °C. In combination with water, the sulfonic groups are able to pass the H^+-ions across the membrane. That's why the membrane must be humid to be functional [1]. With increasing humidity, the thickness of the membrane is swelling up. According to the requested datasheet, Nafion® has a thickness change of 14 % from 50 % relative humidity (RH) and 23 °C to water soaked and 100 °C [10]. With the membrane swelling up it leads to a higher compression of the gas diffusion layer because this is the softest part in the stack. Also in the membrane itself the stress increases, leading as an extreme consequence to pinholes and a faster degradation [7]. The associated effects on the overall system functionality will be considered in detail later on. A typical thickness range of the membrane at initial conditions is between 8 and 250 μm [16]. The thinner the membrane the lower the resistance but also the more difficult the production. Care must be taken with the mechanical properties of the membrane. As Tang et al. showed in [17] the Young's modulus and proportional limit stress are affected significantly by both temperature and humidity. This is quite relevant to bear in mind as the present thesis deals with mechanical issues in the fuel cell.

The membrane is embedded between two catalyst layers and two gas diffusion layers (GDL), one on each side. The catalyst's task is to lower the activation energy for the electrochemical reaction. In most cases, it is made of platinum which is supported by a carbon structure. The place where gas, catalyst and electrolyte come together is called the three-phase interface [14]. This is where the reaction described above is happening. In order to accelerate the reaction, the surface of the catalyst has to be as large as possible. This is achieved through a porous structure of the layer with small platinum particles in the range of a few nanometres on it. The thickness of the catalyst layer lies between 5 and 15 micrometres [14].

As mentioned, the catalyst layers are surrounded by the GDL which is a porous structure made of carbon, mostly either a carbon cloth, carbon felt or carbon paper. An example

is shown in Figure 2.4. Its task is to lead the gases towards the membrane and apart from that to establish an electrical connection between the electrode (the catalyst layer) and the bipolar plate on the other side. It also drains the water which is produced on the cathode side [14, 18]. As the name already indicates, an important transport mechanism towards the membrane is diffusion, for that a big share of pores is needed [19]. The diffusion must be possible through the GDL as well as in the plane to cover the whole active area [19].
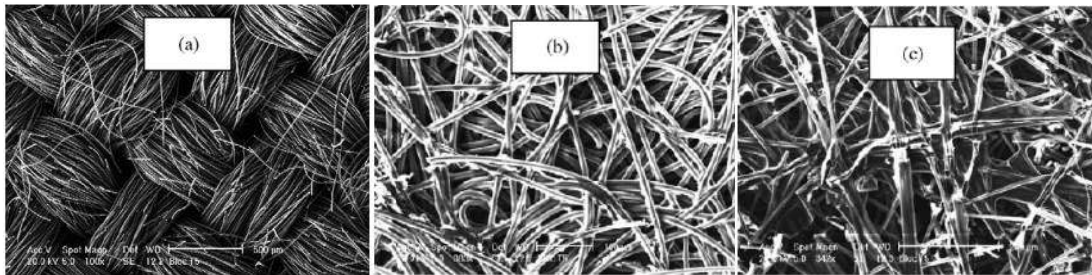
Figure 2.4: Structure of GDL (a) carbon cloth, (b) carbon felt, (c) carbon paper [18]

Because liquid water would clog the channel structure the GDL is coated with polytetra-fluoroethylene (PTFE) which enhances hydrophobic properties [6]. The thickness of the GDL is between 100 µm [6, 19] and 250 µm [19]. To establish a good electrical connection to the bipolar plate a high compression force is necessary to decrease the contact resistance. At the same time, a too-big assembly force would compress the GDL severely. Since it is built of a porous structure the porosity decreases with higher compression. With lower porosity also the permeability decreases. This means that it can no longer fully carry out its task because diffusion is hindered. The gas supply is more difficult leading to a depletion of hydrogen and air respectively in corresponding regions. This leads to a slower reaction rate, a lower voltage and a worse performance in total [7, 20]. Another aspect is that also the produced water on the cathode side is more difficult to discharge. The clogged channels also lead to hindered gas transport, a lower reaction rate and a decrease in performance [7]. Important to bear in mind is that the GDL, once it has been overcompressed, does not deform back completely, but retains a plastic strain [7]. To conclude, it is essential to find a compromise with the magnitude of the pressure on the GDL in certain tolerances both in the assembly process and during operation for improved contact resistance on one side and good diffusion properties on the other side [7].

Together the membrane, catalyst and GDL form the MEA which is surrounded by two bipolar plates. Often there is a sub-gasket which laminates the membrane at its edges to prevent corrosion in the bipolar plate due to the acid membrane environment [19]. The corrosion would accelerate the degradation. Apart from that it also fixes the membrane in its place.

The structure and the tasks of the BPP will be elaborated in the next subchapter.

2.2.2   Bipolar Plate

The main tasks of the bipolar plate (BPP) are to conduct the electrons through the stack and to spread the gas over the complete area of the active zone through the integrated flow field structure. The flow field should be designed in a way that the gases flow uniformly across the electrode [6]. Typically, there are two types of bipolar plates (BPP). The first type is made of graphite composite, the second of metallic material, mostly stainless steel. In the case of metallic BPPs, the two halves are welded together for example through laser welding [19]. As shown in Figure 2.5 there are two outer and one inner channel area. The outer channel areas of the BPP have hydrogen (on the anode side) and oxygen (on the cathode side) flowing through them. The inner part is flooded by a coolant that has the task to dissipate the heat which is generated during the reaction.
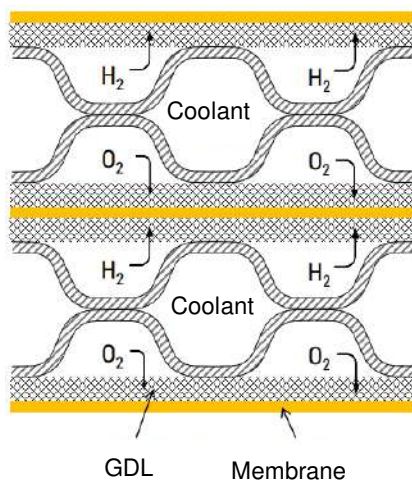
Figure 2.5: Principle sketch of two BPPs with MEA in between [21]

Apart from that, the BPP delivers the mechanical stiffness and gives stability to the whole cell. Out of the tasks of the BPP the requirements can be derived. A low electrical

resistance improves the efficiency of the stack. At the same time, high chemical resistance is obligatory. Also, the hydrogen embrittlement must not be neglected which would negatively influence the material properties [11].

Because of the direct contact between the bipolar plate and GDL, the BPP is responsible for the evenly distributed pressure over the surface of the GDL [1]. With the periodic alternation of land and channel structure in the BPP the pressure also alternates in certain degrees. Under high pressure, the GDL can invade in the channel area [22].

Using metallic BPPs it is possible to achieve very thin thicknesses. This leads to a higher gravimetric and volumetric power density. Therefore, this option is preferred in mobile applications. The major advantage of graphite composite BPPs is their low susceptibility to corrosion. This results in longer service life, an important factor in stationary continuous operation [11].

Electrically, the bipolar plates are connected in series so that the voltage of each cell adds up to the stack voltage [19]. This enforces the same current in each cell and thus the same demand for hydrogen and oxygen in each cell. An uneven gas distribution leads to a higher reaction rate in the areas with more gas to maintain the total current. This can lead to hotspots damaging the membrane [23]. Therefore, even gas distribution plays an important role in the design of BPPs.

In Figure 2.6 an industrial metal bipolar plate is shown. The flow field structure is clearly visible. On each side are three manifolds for inlet and outlet. The big ones at the top and the bottom are for the gases, hydrogen and air respectively. Through the small manifold in the middle the coolant is fed.
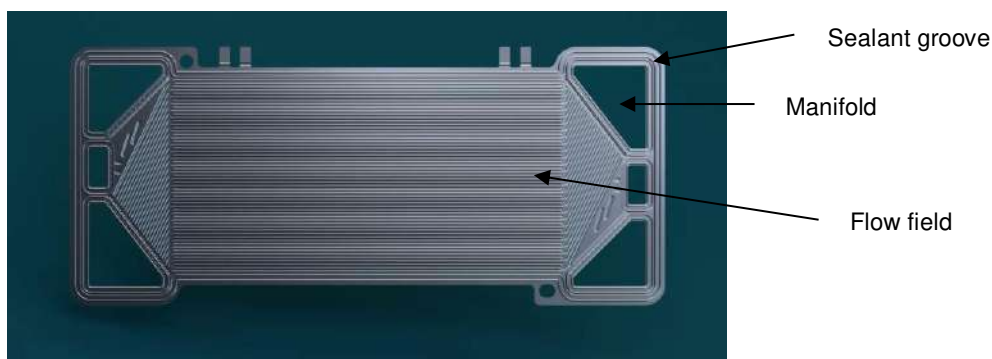
Figure 2.6: Bipolar plate [24]

Around the manifold and along the edge of the BPP a sealant groove is visible. For each cell a gasket is necessary to prevent the gases from leaking and mixing. Another task of the gasket is to compensate differences due to production and assembly tolerances. Of course, also chemical and thermal stability is necessary [11].

In Figure 2.7 a bipolar plate with a gasket is shown. In this case, the gasket is applied directly to the BPP. There are also other possibilities like applying it on the MEA or having it as an extra part. Regarding the assembly speed, it is better to have the gasket preassembled [11].
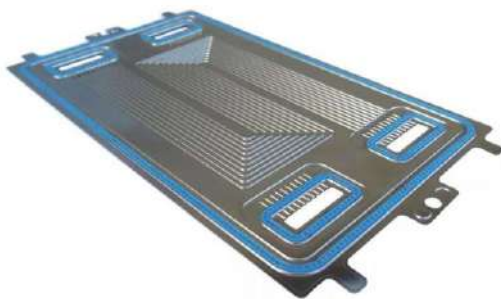
Figure 2.7: Bipolar plate with gasket [25]

The MEA with the gasket and the BPPs is making up a single cell. Many cells together form the fuel cell stack. At the end of the stack, there are some parts which – in comparison to the single fuel cell – are only needed at the top and bottom of the stack. These will be explained briefly in the next section.

2.2.3   Non-repetitive units

At each end of the stack, there are non-repetitive units like the current collector or the end plates (EP). The elements are demonstrated in Figure 2.8. The current collector is located between the last bipolar plate and the end plate. Its task is to conduct the current from the BPP through a cable to the load e.g., an electrical motor. It is therefore made of highly conductive material, usually copper [11].

At the top and bottom, there is an end plate as the closing part of the stack. Its task is of mechanical nature, distributing the pressure in as uniform a manner as possible over the

active area. The homogeneity is important to keep degradation low. In the end plate also the connections for the gas and coolant supply are integrated. It can be made of metal or plastic [11]. In the case of a metallic end plate, an insulation plate is necessary between current collector and end plate to allow safe handling.
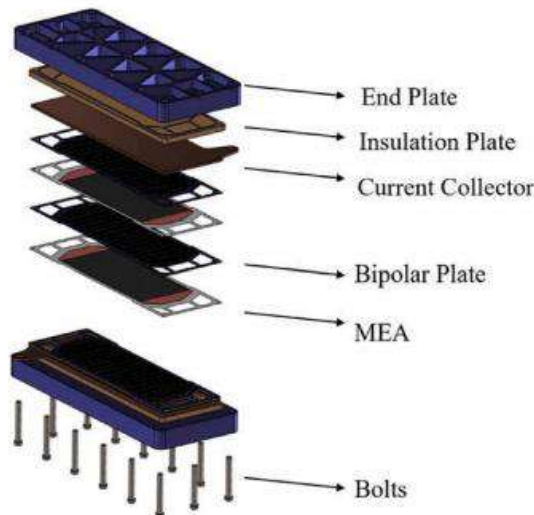

Figure 2.8: End plates, insulation plate and current collector with tie rod assembly [7]

Through tie rods or assembly belts attached to the end plates, the assembly pressure is put on and all the parts are held in position.

In the assembly process a few steps are worked through. Depending on some parameters the performance of the complete stack is influenced. This will be highlighted in the next section.

2.3   Assembly process

In the assembly process first of all the lower end plate and current collector are placed in the mounting device. The next steps are sketched in Figure 2.9, where the following parts are added in the correct order: a BPP, a gasket, the MEA, a gasket and the next BPP [26]. If the gasket and the BPP are preassembled of course the two steps are combined into one. According to the dimensioning of the power of the fuel cell stack, the necessary number of single cells is stacked on top of each other. As last step, the upper

current collector and end plate are mounted. For the correct positioning of all the parts, some guiding elements can support the handling [26].
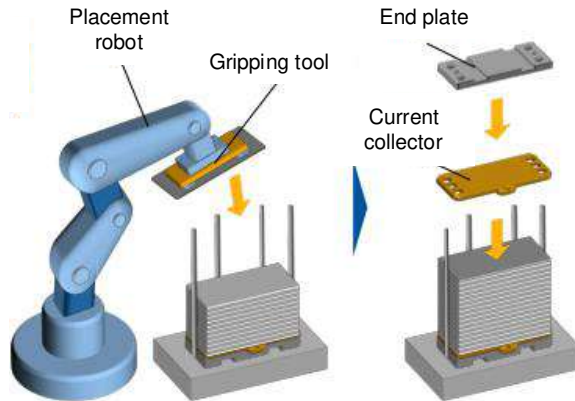
Figure 2.9: Mounting of single cells (adapted from [26])

As next step, the whole stack is compressed through a regulated power press as shown in Figure 2.10. It applies pressure over the whole end plate and lowers the contact resistance between the single parts [26]. In the context of the assembly, the compression force is the parameter with the highest influence on the performance [7, 14]. The effects are discussed later in this section.
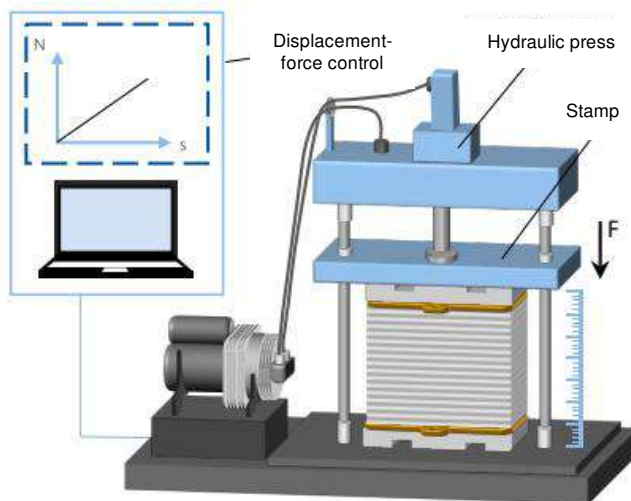
Figure 2.10: Compression of fuel cell stack (adapted from [26])

To keep the parts in their position with the desired contact pressure the end plates are clamped with either tie rods or belts, visible in Figure 2.11. Tie rods are easier to handle in the process but belts lead to a more uniform pressure distribution [26]. After the

compression, the tightness of all the components is measured. In the final step monitoring units are mounted, the whole stack is placed in a housing, and in the following production process, the balance of plant can be connected [26].
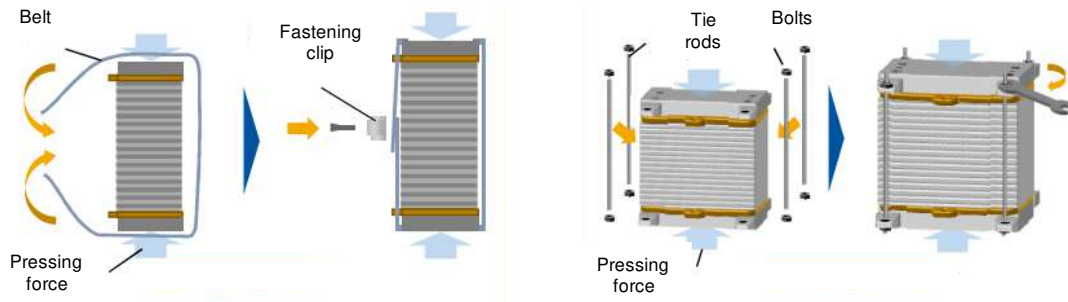
Figure 2.11: Clamping of the stack. Left: Assembly belt, right: Tie rods (adapted from [26])

As the assembly force compresses the parts in the stack, some properties change that affect directly the ability to transport reactants, heat, water and electricity [7]. In general, two unwanted cases can be observed. Either the assembly force is too small or it is too big.

In case the assembly force is too small, also the contact force in the stack later on is too small. This can lead as an extreme consequence to leakage of air, hydrogen or coolant because the sealing properties are no longer guaranteed [7]. If hydrogen and air are mixed in appropriate quantities, flammable and explosive mixtures may result. Even if the gasket is working properly still the contact resistance can increase sharply if GDL and BPP are not or not completely in contact and thereby leading to a worse performance because of the high ohmic losses [20].

These challenges can be responded to with a high assembly force. At the same time, high compression forces lead to increased concentration losses. This is because the GDL is made of a porous structure through which the gases from the flow field in the bipolar plate diffuse to the three-phase interface where the catalytical reaction takes place. The porosity decreases the higher the GDL is compressed hindering the gases to pass. This leads to an insufficient supply to maintain the voltage resulting in a drop of performance. For that reason, a compromise regarding the assembly force is necessary. With the membranes swelling up during the operation of the stack the contact pressure between the parts increases which also leads to a further compression of the GDL with the same consequences.

According to different literature values, an appropriate mean value for the contact pressure over the active area is between 1 [27] and 1.5 MPa [8, 20, 28]. Irmscher showed that the optimal assembly pressure also depends on the GDL type and figured out values between 0.4 and 2.7 MPa. For the GDL type chosen for the simulation, the values lie between 0.6 and 1.7 MPa [29] which overlap with the other authors. Ahmad et al. used a target value of 1.62 MPa [30] which is also in the same range as the previous values. If the flow field structure of the BPP is taken into account the porosity of the GDL under land and channel differ perceptibly, meaning that also the stress varies [22]. If the influence of the channel structure is not in the focus it is sufficient to consider the mean value.

Next to the assembly force magnitude, the uniformity of the pressure distribution has similar effects on the performance. Since the individual cells are connected in series, the voltage adds up, but the current is the same everywhere and is determined by the worst cell [7]. A uniform load distribution both through the stack and across the active area guarantees similar reaction behaviour and a constant current rate.

Depending on the way the assembly load is put on, the load distribution differs. A point load on the edge of the end plate through for example tie rods leads to a higher pressure in the sealing area on the edge and a lower pressure in the centre of the stack. A line load or surface load creates a more even distribution [7].

In summary, the goal is to maintain the pressure on the GDL as constant as possible between the assembly process and operation and at the same time achieve a uniform pressure distribution across the active area. How this is addressed in current industrial products and what a future approach might look like to improve this, is discussed in the next chapter.

3 Current handling and concept elaboration to mitigate membrane swelling

The swelling of the membrane during operation is inevitable and there are existing concepts to deal with the expansion but there is not a lot of public information available on current methods. In this chapter, some methods found about the state-of-the-art will be presented first and in the second section possible spring concepts will be introduced and explained in order to understand the later simulations.

3.1 State-of-the-art to handle the stack swelling

Jörissen and Garche mention briefly that springs or hydraulic cushions are used in PEM-FCs to keep a uniform force distribution, especially during temperature variation [19]. The hydraulic cushions have the disadvantage of a higher system expenditure. There are some patents that show the use of spring systems in fuel cells. Two examples are shown in Figure 3.1 where first, a set of big coned disc springs is positioned at the bottom of the stack (part 42 in the left sketch) [31] and second, an external spring system is installed to compensate the movement of the stack during operation [32]. Another possibility is shown in Figure 3.2 where an internal metallic pressure bellows is inserted below the end plates to maintain a uniform surface pressure over the active area [33].

Scholta et al. developed a generic fuel cell stack which contains a pressure plate with helical springs [34]. A model of the end plate unit is shown in Figure 3.3 on the left. This has the advantage of even pressure distribution but contains many extra parts like the pressure plate which is moved through a piston plate inside the end plate.
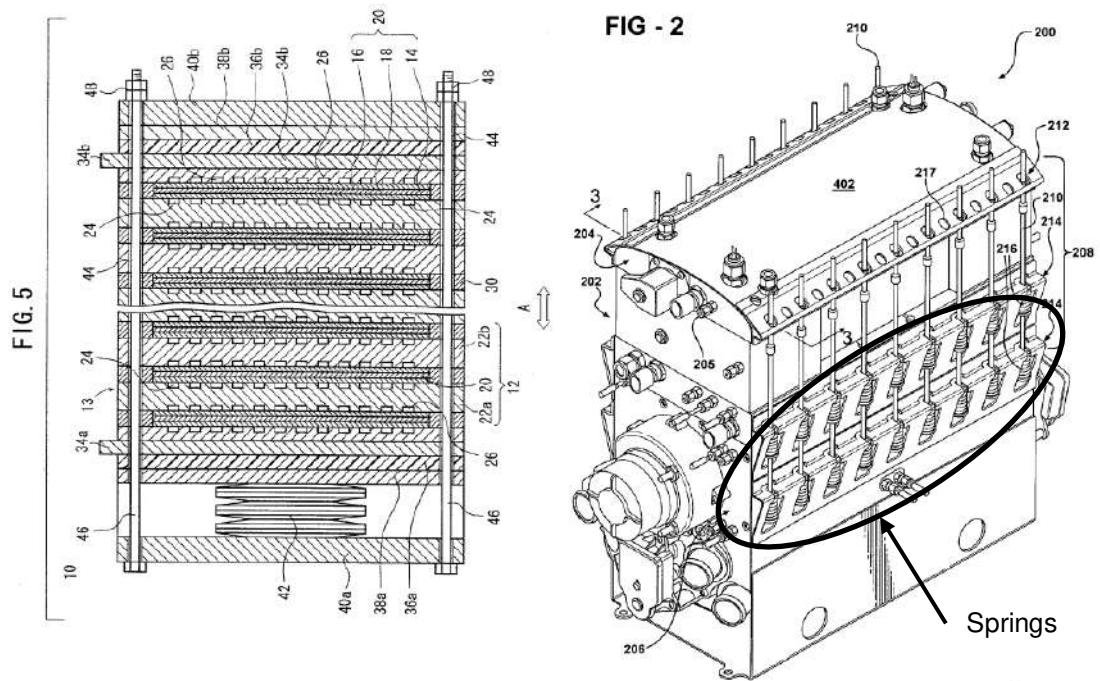
Figure 3.1: Left: Coned disc springs for absorption of expansion [31], Right: Compression retention system with external springs [32]
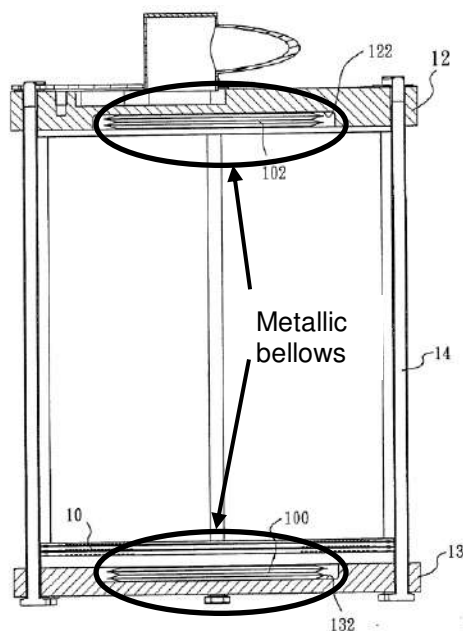
Figure 3.2: Metallic pressure bellows [33]

Another proposal was designed by Wang et al., shown in Figure 3.3 on the right-hand side. Here, a hydraulic cushion is integrated into both end plates with a very thin

thickness to the cell stack. Through the even distribution inside the hydraulic chamber, the pressure is distributed uniformly across the active area. The pressure is generated through a pump [35]. The disadvantage of this design is the increased complexity of the whole system.
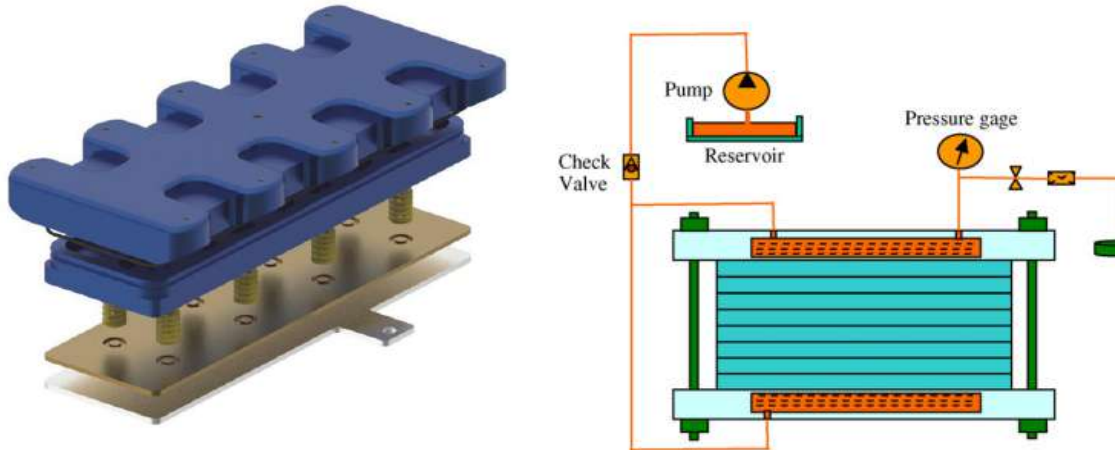
Figure 3.3: Left: End plate at anode side with springs and spring plate [34], Right: Hydraulic pressure pocket [35]

Borgardt recommends the use of screws combined with spring elements [36]. Her work refers to electrolysers but since the structure and functionality are very similar this can be transferred to fuel cells as well. An example can be seen in Figure 3.4 and Figure 3.5.
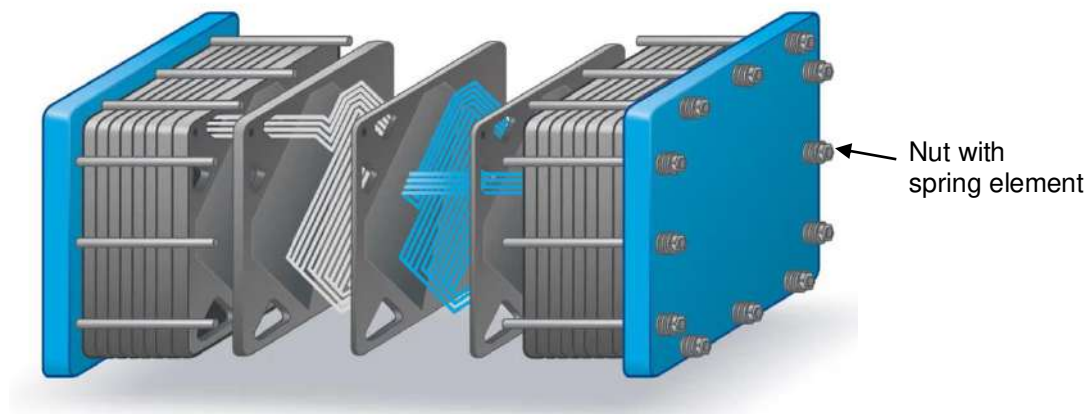
Figure 3.4: Usage of nuts with spring elements on end plate [37]
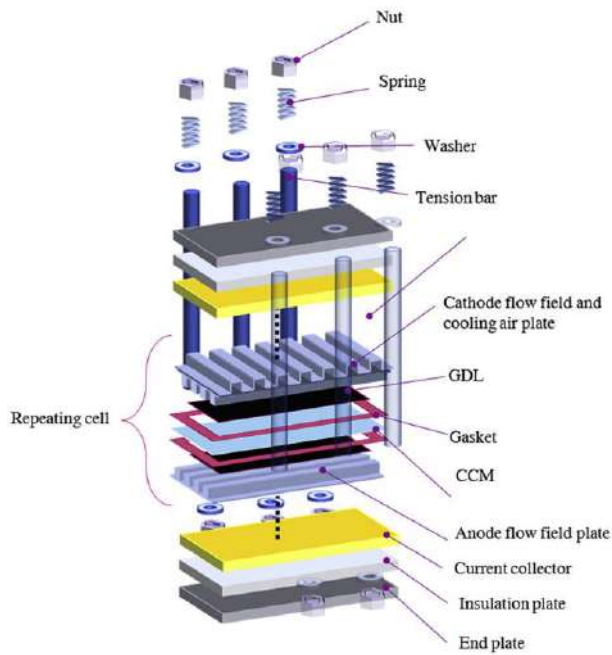
Figure 3.5: Model of PEMFC with springs and washers in assembly group [30]

Zhang et al. calculate an optimal position for Belleville springs (or disc springs) to reduce the end plate deformation [38]. Asghari et al. also use a set of Belleville springs on each tie rod to smoothen the assembly load and absorb expansion through thermal load [8]. Bendzulla mentions the use of disc springs in combination with tie rods as well [39].

In the product catalogues of spring manufacturers, fuel cells are mentioned several times as being an area of application. The Solon Manufacturing Co. for example explains the use of washers and Belleville spring stacks in PEMFCs. They offer the service of designing customized solutions [40]. The company Spirol offers pre-stacked disc springs for fuel cells and electrolysers to keep the stacking effort of disc springs low in an assembly line of a fuel cell stack [41]. At last, also the company Schnorr has disc springs for fuel cells and electrolysers in its program [42].

With all of this background information and especially the industrial availability, the decision is taken to implement a stack of disc springs on each tie rod of the fuel cell. According to the necessary force on each tie rod of the existing fuel cell model, the springs are calculated to represent the state-of-the-art.

3.2   Elaboration of possible future spring concepts

As shown in the previous section, there are several possibilities to smoothen the stress distribution over the MEA in the fuel cell and to compensate the swelling during operation. The most common variant with the disc spring stack on top of the tie rods is very easy to mount but the stress differences between the edge and the centre of the MEA are still significant. Other variants have a lot smoother output but lead to a great system complexity which is more vulnerable to failure. That's why new concepts are elaborated to unite the two requirements of uniform stress distribution and simplicity. After the introduction of the fuel cell model, the forces acting on the springs due to assembly and operation are calculated. Then the design proposals are presented. The springs are calculated in collaboration with a spring manufacturer.

3.2.1   Introduction of fuel cell model

At IPEK, the institute the thesis is realised in, a fuel cell stack concept was developed on which the novel concept elaboration is based on. Because for the dimensioning of a new spring concept some parameters of the model are needed, it is presented here. The complete model is shown in Figure 3.6. It contains one single fuel cell. Because of the symmetry, every part exists on anode and cathode side. The two bipolar plates are shown in red in the centre with the MEA unit in between. They are followed by cooling plates and the current collector plates in grey. Indicated with the green colour is a heating unit to simulate different operating conditions. At the end of the stack are the insulation plates in white and finally the end plates. The top end plate contains the connectors for hydrogen, air and coolant. The assembly pressure is held by ten tie rods.
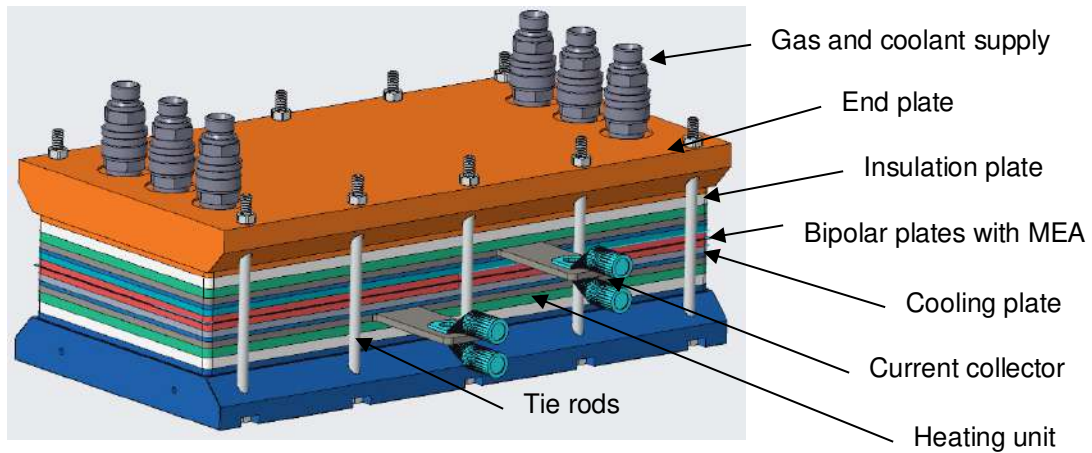
Figure 3.6: CAD model of single fuel cell [43]

The size of the end plates is 240 mm by 454 mm, the tie rods have a distance of 100 mm from each other. The active area containing GDL, membrane and catalytic layer has a length of 224 mm and a width of 128.5 mm with a total area of 28 784 mm^2. It is shown in Figure 3.7.
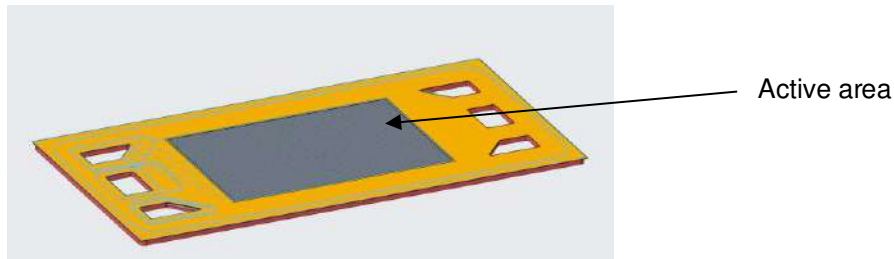
Figure 3.7: Bipolar plate with MEA area in grey [43]

For the simulation of the spring concept, it is necessary to consider the swelling of a full stack. Therefore, an output power of 150 kW is chosen with a total of 456 cells according to Scholta et al. [34]. A possible membrane could be a membrane by Gore, named M775.15 with a thickness of 15.5 µm [44]. The GDL is assumed to be the carbon paper type Toray TGP-H-030 with a thickness of around 0.11 mm [45].

3.2.2   Assembly and operating forces

The relevant forces for the dimensioning of the spring concept are divided into three separate calculations. First, the necessary force for the contact pressure between BPP

and GDL. Second, the force for compressing the gasket and third the force acting on the stack through the swelling of the membrane. The three forces can be summed up because their acting is equivalent to parallel springs.

3.2.2.1   Contact force between BPP and GDL

For the contact pressure between BPP and GDL a target mean value of about 1.5 MPa stress in the compression direction in the GDL is aimed for according to the sources rolled out in section 2.3. With the formula

$$p = \frac{F}{A} \hspace{4cm} \text{3.1}$$

pressure, force and area are connected. The necessary force to establish good contact between BPP and GDL can be calculated to

$$F_{contact} = p_{contact} \cdot A_{membrane} = 1.5\,MPa \cdot 28\,784\,mm^2 = 43\,176\,N. \hspace{1cm} \text{3.2}$$

3.2.2.2   Force for compression of gasket

The gasket needs to be compressed to be able to fulfil its function. According to [46], a gasket should be compressed to a minimum of 10 % and a maximum of 50 %. That's why a target value of around 30 % is aimed for.

Because the current CAD model does not contain the model of the gasket a simple sketch is drawn to be able to take it into account. First, the gasket at the edge of the BPP is considered. The sealant groove is 4.8 mm broad and has a depth of 2.7 mm. With the height of half the MEA unit in between, the thickness of the compressed gasket should be

$$2.7\,mm + 0.11\,mm + \frac{0.0155}{2}\,mm = 2.818\,mm. \hspace{2cm} \text{3.3}$$

With the compression factor of 30 % an initial height of

$$\frac{2.818\,mm}{0.7} = 4.025\,mm \hspace{3cm} \text{3.4}$$

is calculated. A final value of 4.05 mm is chosen to consider the thickness of the sub-gasket, which is in the range of 25 µm [47]. To fill the whole groove of the BPP it is necessary that the cross-section of the compressed and the uncompressed gasket has the same area. This means that a width of

$$b_{1,initial} = \frac{h_{1,comp} \cdot b_{1,comp}}{h_{1,initial}} = \frac{2.82\ mm \cdot 4.8\ mm}{4.05\ mm} = 3.34\ mm \tag{3.5}$$

is necessary for the uncompressed gasket.

The sealant grooves around the gaskets at the manifolds have a depth of 1.3 mm and a width of 2.9 mm. Assuming the top of the frame gasket and the manifold gasket are on the same level the manifold gasket has an initial height of 2.65 mm. With the same condition of the equal area size between compressed and uncompressed gasket an initial width of

$$b_{2,initial} = \frac{h_{2,comp} \cdot b_{2,comp}}{h_{2,inital}} = \frac{1.42\ mm \cdot 2.9\ mm}{2.65\ mm} = 1.55\ mm \tag{3.6}$$

is calculated. Both widths are rounded off to be able to have some tolerance for the compression of the MEA unit. So finally, a value of 3.3 mm for the frame gasket and 1.5 mm for the manifold gasket are defined. An image of a quarter bipolar plate with the gasket in position is shown in Figure 3.8.

As material 60 Shore A EPDM (ethylene propylene diene monomer rubber) is chosen according to Alizadeh et al [27]. This is an elastomer frequently used as sealant material [19]. It does not follow Hook's law, for that the stress-strain curve is given in Figure 3.9. To determine the compression force, an FEM simulation is run with a sample piece of the gasket with the material properties of EPDM. The material is implemented as hyperelastic material with a Neo-Hookean fitting as proposed in [27].
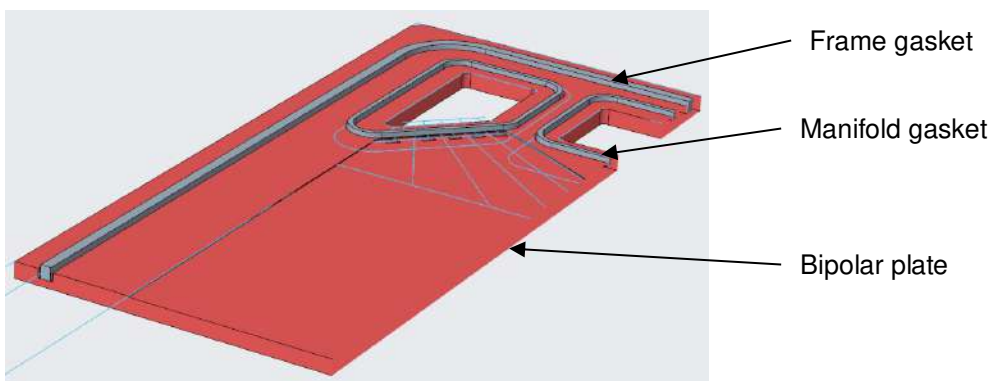
Figure 3.8: Bipolar plate with designed gasket (adapted from [43])

In the sample piece, a gasket length of 10 mm is clamped between two equivalent pieces of a bipolar plate. An example is shown in Figure 3.10. The edges of the gasket are constrained so that they can only move in compression direction. The two pieces are

pressed together so that the stress in the compression direction can be extracted to calculate the necessary force.
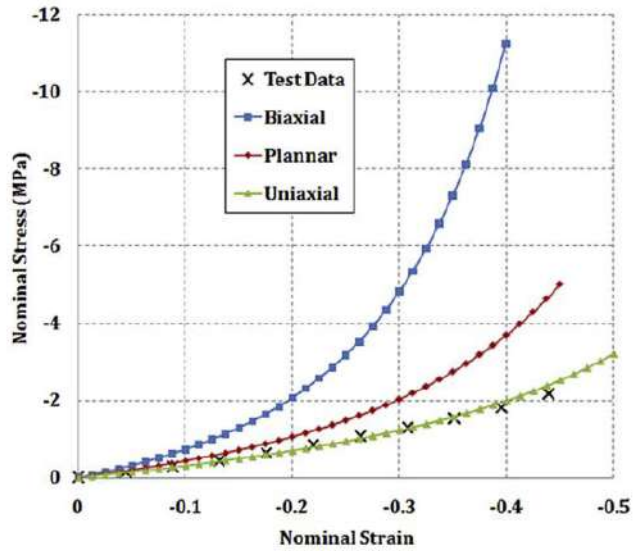
Figure 3.9: Material data of 60 Shore A EPDM [27]
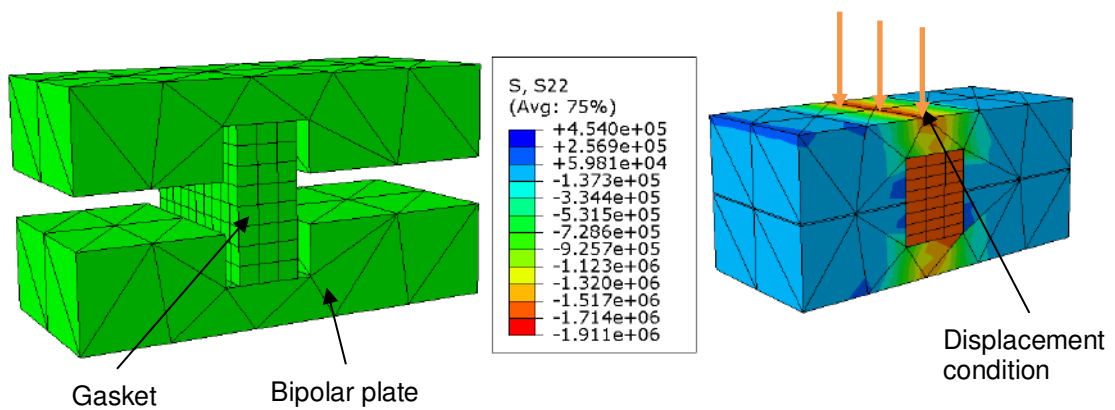
Figure 3.10: Left: sample piece of uncompressed gasket, right: compressed gasket

The measured stress inside the gasket is 1.5 MPa. The specific force for the compression of one centimetre of gasket can be calculated to

$$f_{gasket,frame} = \sigma_{gasket,frame} \cdot A_{gasket,frame} = 1.5\, MPa \cdot 10\, mm \cdot 4.8\, mm = 72\, N. \qquad 3.7$$

For the gasket around the manifolds the same method is applied. There the measured stress is 3 MPa and the specific force is

$$f_{gasket,manifold} = \sigma_{gasket,manifold} \cdot A_{gasket,manifold} = 3\, MPa \cdot 10\, mm \cdot 2.9\, mm = 87\, N. \qquad 3.8$$

The total length of the frame gasket is 119.36 cm and of the manifold gasket 111.9 cm. Through that the total force for the compression of the gasket is

$$F_{gasket,frame} = f_{gasket,frame} \cdot l_{gasket,frame} = 72\frac{N}{cm} \cdot 119.36\, cm = 8\,594\, N \qquad 3.9$$

$$F_{gasket,manifold} = f_{gasket,manifold} \cdot l_{gasket,manifold} = 87\frac{N}{cm} \cdot 111.9\, cm = 9\,735\, N \qquad 3.10$$

$$F_{gasket,total} = F_{gasket,frame} + F_{gasket,manifold} = 8\,594\, N + 9\,735\, N = 18\,329\, N \qquad 3.11$$

3.2.2.3   Force through membrane swelling

The last relevant force for the spring concept appears during operation when the membrane swells due to temperature and humidity rise. The swelling ratio β of one membrane is 14 % from 50 % relative humidity and 23 °C to a water-soaked state and 100 °C [10]. With a total number of 456 cells and a thickness of 15 µm per membrane (see section 3.2.1) the total rise of the stack is

$$u_{Stack} = t_{membrane} \cdot N \cdot \beta = 15\, \mu m \cdot 456 \cdot 0.14 = 0.96\, mm. \qquad 3.12$$

The pressure rise initiated through the swelling is taken from literature values. Borgardt finds that a pressure between 0.7 and 1.15 MPa can be generated [36]. Mason et al. measure a rise of 1.1 MPa [48]. Out of these values, a pressure rise of 1 MPa is assumed, thus leading to an equivalent force of

$$F_{swelling} = p_{swelling} \cdot A_{membrane} = 1\, MPa \cdot 28\,784\, mm^2 = 28\,784\, N. \qquad 3.13$$

In total a force of

$$F_{tot} = F_{contact} + F_{gasket} + F_{swelling} = 43\,176\, N + 18\,329\, N + 28\,784\, N = 90\,289\, N \qquad 3.14$$

will act on the spring design. In the following section, the designs of the new concepts will be rolled out.

3.2.3   Design proposals

There are two design proposals shown in a sketch in Figure 3.11 that are feasible after consultation with the spring manufacturer. The first is a spring plate, shaped with bending tools and welded together at its ends. The second is a spring made through a deep drawing process. Because of the remaining metal bridges on the bottom, this variant is called spring with bridge structure.
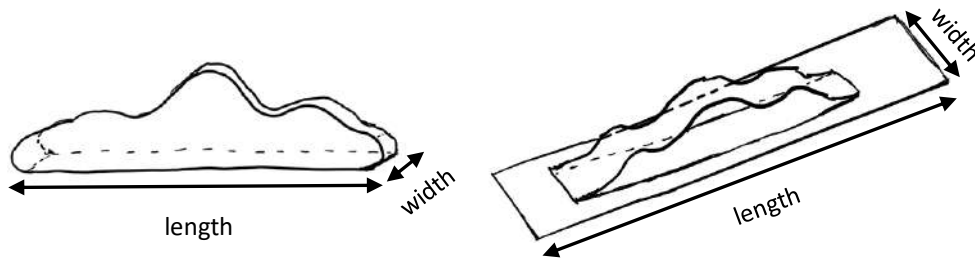

Figure 3.11: Sketches of the spring designs. Left: welded spring belt, right: spring with bridge structure

The idea of the characteristic curve is to be degressive with the aim that the rise of the force between assembly and operation is as small as possible. The assembly force is 61.5 kN as calculated in section 3.2.2. The expected total force through the membrane swelling is around 90.3 kN but depends on each specific spring concept. The maximum height change of the stack is 0.96 mm, this is the distance the springs need to compensate. A qualitative characteristic curve with the degressive course is shown in Figure 3.12.
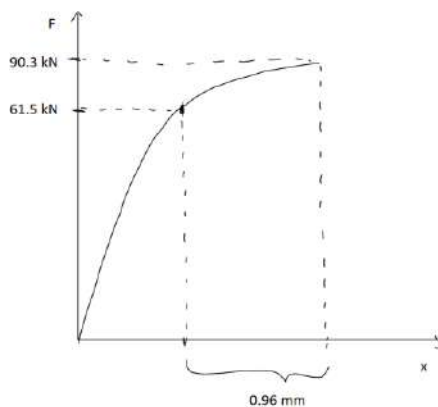
Figure 3.12: Qualitative characteristic curve of spring design

The general shape is calculated by the spring manufacturer. The task of the thesis is to propose different variations that are simulated and compared with each other. An approach is to test the extreme sizes of the springs to see how they differ from each other. All the proposals are shown in Table 3.1.

Concept 1:

- Welded spring belt design in size of end plate i.e., 240 mm long and 450 mm wide

- Highest point of the spring is in the middle of the stack, swelling occurs also in the middle

    o Likely, that the pressure rise is compensated better than with a spring concept on the edges of end plate

- Through size of spring, a completely evenly distributed contact pressure between spring and end plate is likely which should lead to a uniform pressure distribution in the MEA

- Assembly belts with five belts instead of tie rods would have to be used

Concept 2:
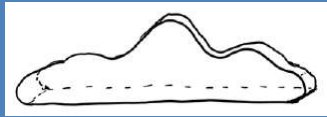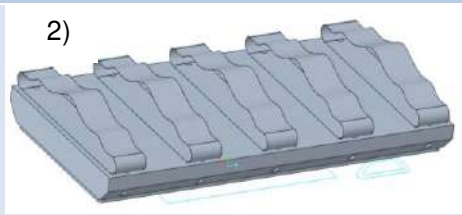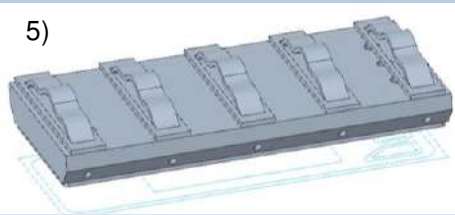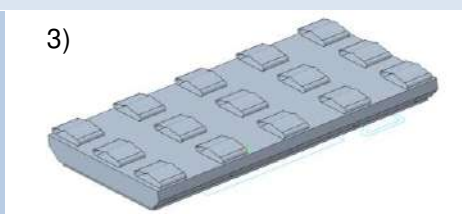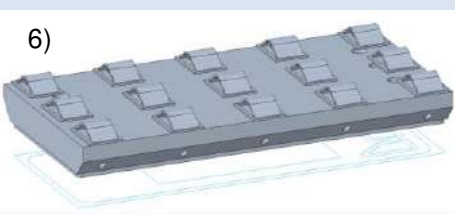
- Welded spring belt design, 5 springs: length 240 mm and width 40 mm

- Force only enters end plate through the location where it is applied (in contrast to concept 1)

- Springs can be moved closer together or further apart from each other to change the distribution over the active area

- Assembly belts would have to be used

Concept 3:

- Welded spring belt design

- Each of the 5 springs from concept 2 is divided into three smaller springs, results in total of 15 springs

- Length: 60 mm, width: 40 mm

• Additional possibility of changing the stiffness of particular springs to exert a higher force in specific point

Table 3.1: Proposed spring concepts

Descrip-tion	Design with welded spring belt	Design with bridge structure
Biggest possible spring	1)	
5 big springs	2)	5)
15 medium-sized springs	3)	6)
Smallest springs, spread over active area	4)	7)
Smallest springs, spread over complete EP		8)

Concept 4:

- Welded spring belt design

- Concept with the smallest springs, total of 154 springs spread over the active area

- Length: 14 mm, Width: 5 mm

- Springs don't have to be placed on top of end plate but can be put inside as an extra spring plate

  o   Because of that also possibility of using tie rods

- Spreading springs only over active area because swelling only occurs there, only there compensation is necessary

- Possibility to change stiffness of the single springs over width or length to influence pressure distribution

The next four concepts are similar to the first four but instead of the welded spring belt the design with the bridge structure is used.

Concept 5, 6 and 7:

- Equivalents of concept 2, 3 and 4, respectively

Concept 8:

- Same spring size as concept 7

- Covers complete size of end plate with a total number of 516 springs

  o   Same area as in concept 1 is covered

  o   Possibility of taking force of gasket into account and the stiffness could also be changed to adjust pressure distribution

With the concepts varying in size, it can be classified as a variation of shape according to Albers [49]. Since the designs both welded spring plate and spring with bridge structure work as a mechanical spring it is a variation of shape rather than a variation of principle.

After a first calculation of the spring concepts through the spring manufacturer the concepts with the small springs are disqualified. This is because the plastic deformation of the springs is too high with respect to the expected forces. That's why only variant 1, 2, 3, 5 and 6 can be tested. The characteristic curves of the concepts are shown in Figure 3.13. Variant 1 and 2 have a very linear process. Variant 3 has a very fine degressive share towards higher compression. In variant 5, the degressive part becomes clearer and finally, variant 6 has a very distinct flattening course with a maximum force at 1.1 mm which decreases again at higher compression.
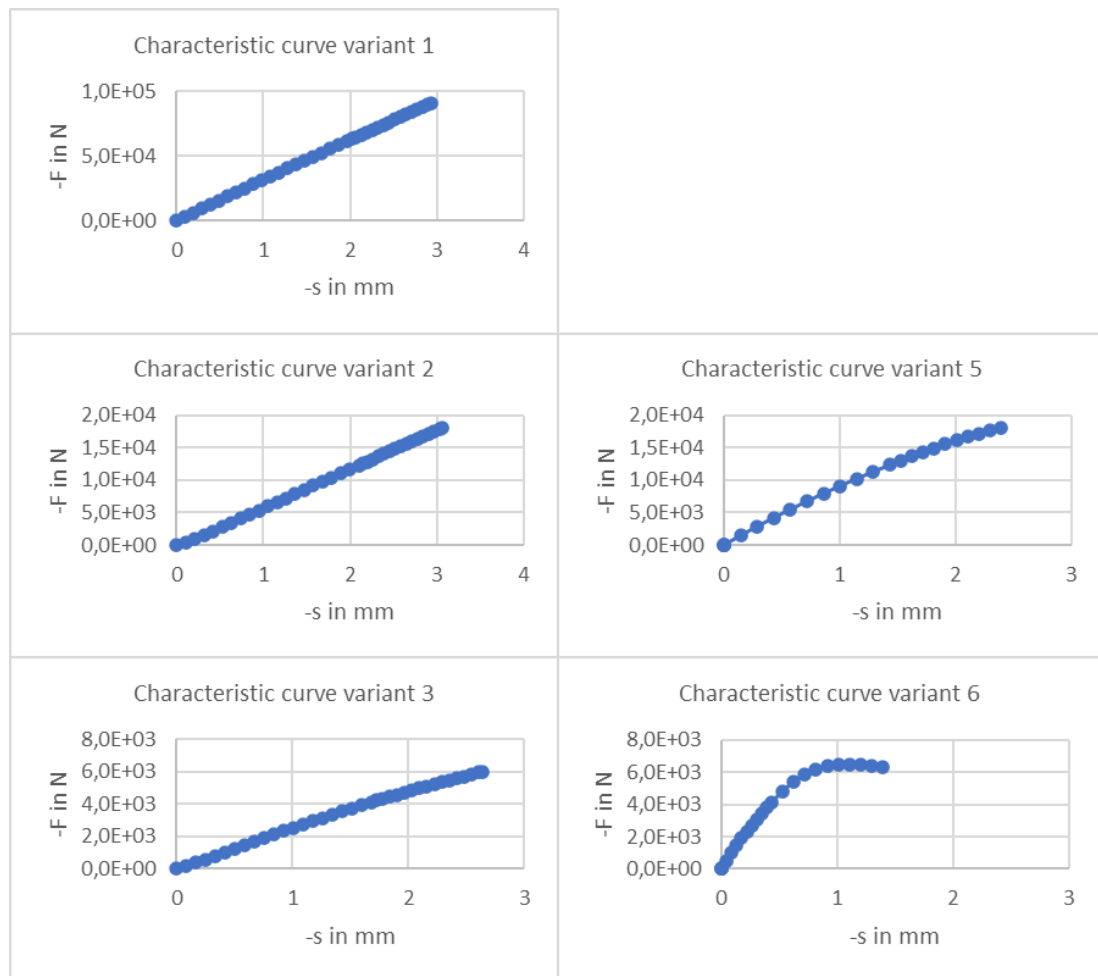
Figure 3.13: Characteristic curves of the spring concepts

Because the springs in the concepts with more than one spring are connected in parallel, the approximate force per spring can be calculated by dividing the total stack force by the number of springs. The forces for each variant together with the unloaded overall height are listed in Table 3.2.

With the data provided through the spring manufacturer the spring characteristics can later be implemented in the simulation software to analyse their behaviour.

Table 3.2: Spring properties for each concept

	Description	Max. Force in kN	Unloaded height in mm
Variant 1	Biggest possible spring, welded spring belt	90.3	60
Variant 2	5 big springs, welded spring belt	18.06	61.6
Variant 3	15 medium-sized springs, welded spring belt	6.02	15.4
Variant 5	5 big springs, spring with bridge structure	18.06	28.7
Variant 6	15 medium-sized springs, spring with bridge structure	6.02	15.4

4   Simulative investigation of the spring concepts

To analyse the behaviour of the different spring concepts they are implemented in a Finite Element Method (FEM) model which is built in the commercial software Abaqus. FEM is a very useful tool to predict the level and distribution of stresses or displacements which is of high interest regarding spring concepts. Since only the mechanical impact on the fuel cell is taken into account there is no need to simulate gas flows, electrical current or heat flow. A graphical flow chart with the single steps is shown in Figure 4.1. First, the spring concepts are laid out in detail with the contact behaviour and the design of the disc spring stack. Afterwards the implementation of the simplified CAD model together with the springs is explained. With the correct conditions defined the calculation can be started to obtain the results. Important to bear in mind for the use of Abaqus is that there is no unit system. Correct results can only be obtained by consistently using the same reference. In the present project the SI units are used, so length is in meters, temperature in Kelvin, time in seconds and mass in kilograms, thereby force in Newton and stress in Pascal.
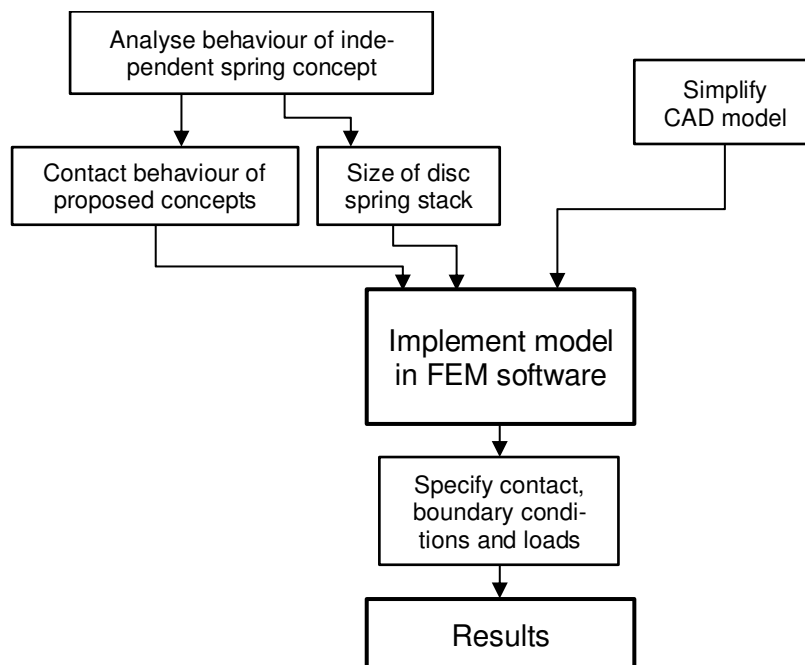
Figure 4.1: Graphical flowchart explaining the steps of the simulation

4.1   Behaviour of specific components

In this section the calculation of the disc spring stack representing the reference solution for the swelling is laid out. In a second part the analysis of the spring concepts is explained, showing the force flow through the part.

4.1.1   Disc spring stack representing the state-of-the-art

A disc spring is a circular, flat, conical disc which changes its shape under load in axial direction [50]. The most important dimensional data is shown in Figure 4.2 on the left. This is the outer diameter D_e, the inner diameter D_i, the material thickness t and the height l_0. If disc springs are stacked in the same direction, the force increases, if stacked in an alternating sense the spring deflection increases. By stacking stacks of springs as visible in Figure 4.2 on the right, both parameters can be influenced.
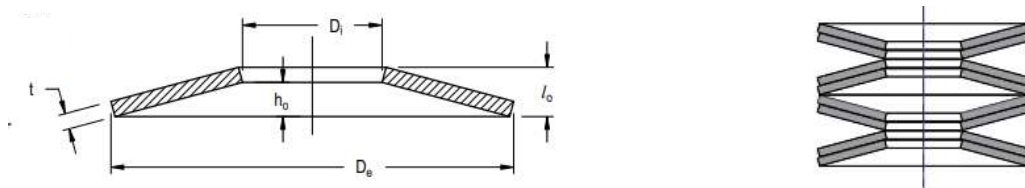
Figure 4.2: Left: Single disc spring, right: layered spring stack [50]

The disc springs would be mounted on the tie rod on the upper end plate of the fuel cell stack. The tie rods have a diameter of 8 mm, that's why according to DIN EN 16983 the inner diameter of the disc spring will be 8.2 mm [50]. There are a couple of possibilities for the outer diameter and the material thickness. To keep the spring stack as small as possible the spring with the highest permissible force is chosen, that is an outer diameter of 18 mm and a material thickness of 1 mm per disc spring. The forces and displacements for a single spring are listed in Table 4.1.

Table 4.1: Forces and displacements of single disc spring [50]

Displacement (mm)	Force (N)
0.00	0.00
0.08	345.00
0.13	559.00
0.25	1051.00
0.38	1497.00
0.50	1921.00

To be able to handle the total stack force the number of springs stacked in the same direction is calculated by dividing the total stack force by the number of tie rods and then by the maximum force per disc spring. A disc spring should only be loaded up to 75 % of the maximum displacement [50], this is in the present case a displacement of 0.38 mm with a force of 1 497 N.

$$N_{Spring,equal} = \frac{F_{tot}}{N_{tie-rods} \cdot F_{max,spring}} = \frac{90.3 \, kN}{10 \cdot 1\,497 \, N} = 6.03 \qquad 4.1$$

To choose the final number of springs the calculated number needs to be rounded up. That means seven springs per stack are needed to handle the force.

To calculate the number of alternating springs an iterative calculation is necessary. First, only the displacement of the swelling active area is known with a value of 0.96 mm as calculated in section 3.2.2.3. With that the initial number of alternated stacked springs can be calculated to

$$N_{ini,Spring,alternating} = \frac{u_{min,tot}}{u_{max,spring}} = \frac{0.96 \, mm}{0.38 \, mm} = 2.5. \qquad 4.2$$

The value must also be rounded up, so an initial number of 3 alternating spring stacks is chosen. Through the assembly force the spring stack will be precompressed and undergoes further compression through the stack swelling. With a closer look to the characteristic curve of three alternating stacks with seven springs each in Figure 4.3 it is visible that with an assembly force of 6 000 N per tie rod there will be a deflection of 0.6 mm. This means that in reality a displacement of

$$u_{tot} = 0.6 \, mm + 0.96 \, mm = 1.56 \, mm \qquad 4.3$$

is necessary.
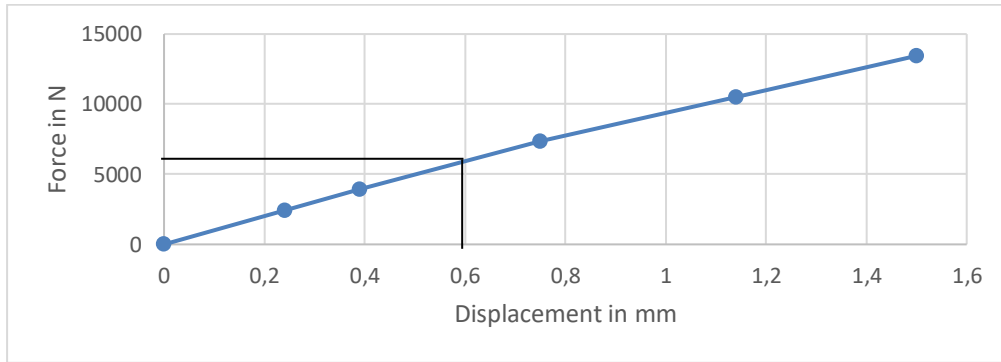
Figure 4.3: Characteristic curve of 3 stacks with 7 disc springs each

Through that the final number of alternating springs is

$$N_{Spring,alternating} = \frac{u_{tot}}{u_{max,spring}} = \frac{1.56\ mm}{0.38\ mm} = 4.1.$$

4.4

Being rounded up again there will be 5 alternating stacks with 7 springs per stack on each tie rod. The final characteristic curve is shown in Figure 4.4 and is implemented like that to represent the state-of-the-art.
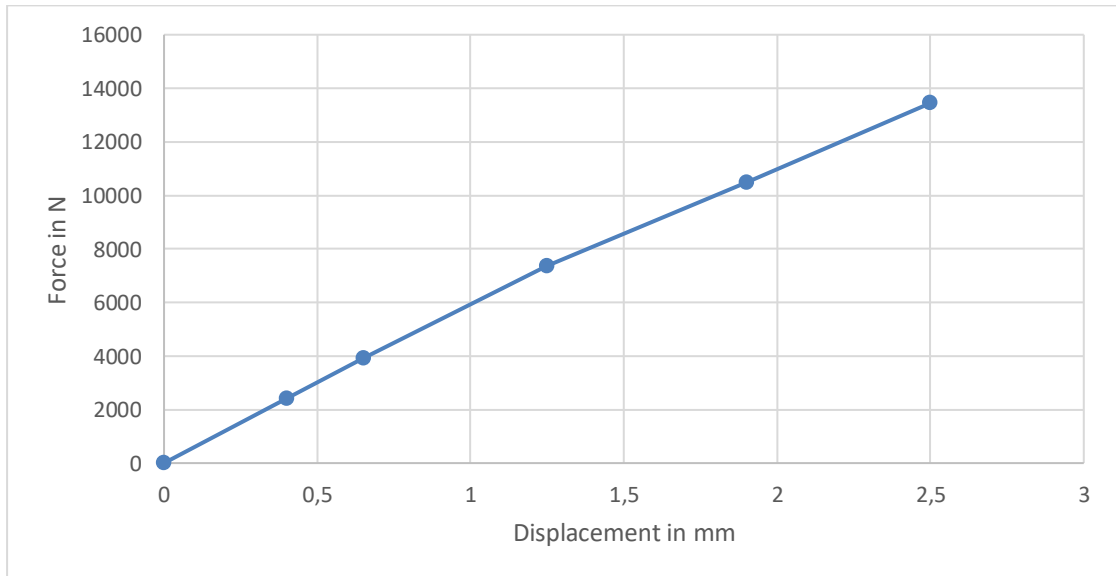

Figure 4.4: Characteristic curve of 5 stacks with 7 disc springs each

4.1.2   Springs

For the simulation the geometry of the springs is not given but only the characteristic curve for each concept. To be able to later implement the characteristic curve of each spring correctly in the FEM model, it is necessary to understand the force flow through the parts itself. To achieve that, the spring is sketched and modelled on a plate in the FEM software, then it is loaded with a displacement on top and as result the spots with contact pressure between the spring and the plate are analysed. From the geometry the length and width are known and the length of the flat bottom part, the dimensions of the bridge structure and the top radius. Because of that the rest is sketched approximately. In Figure 4.5 the undeformed and the deformed shape of the spring is shown. The deformation is shown with a scale factor of almost 10 to make it better visible. Since the values are not important at this point the legend is omitted.

Applied displacement
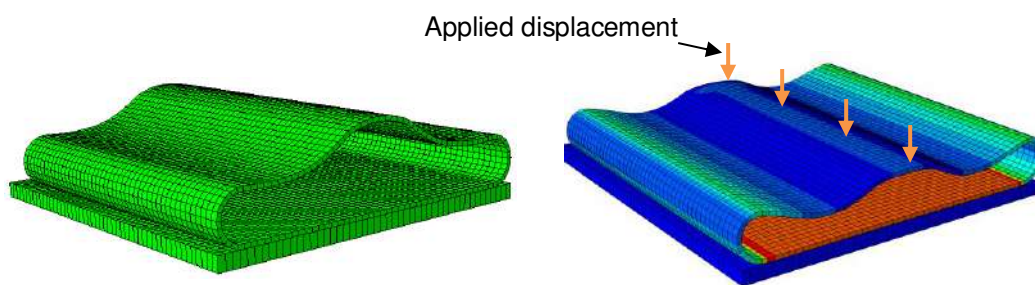
Figure 4.5: Undeformed und deformed model of spring concept 1 on a plate

Both the plate and the spring are assigned steel as material. The bottom of the plate is fixed in all directions. Since only half of the part is modelled a symmetry condition is applied on one end of spring and plate. The spring also needs a constraint in the sideways direction to not slide away. On the top edge a displacement of about 3 mm is given. Between the spring and the plate, a contact interaction is applied so that the parts cannot penetrate into each other. When analysing the contact pressure between the parts, the pressure on each node can be read. In Figure 4.6 the two parts are shown separately to make the contact surface visible. The dark blue elements are not at all in contact. Only where the two green stripes on each end are visible there is contact between the plate and the spring. This is because due to the spring deformation the flat bottom of the spring is bending very slightly upwards so that only the edges exert a pressure.
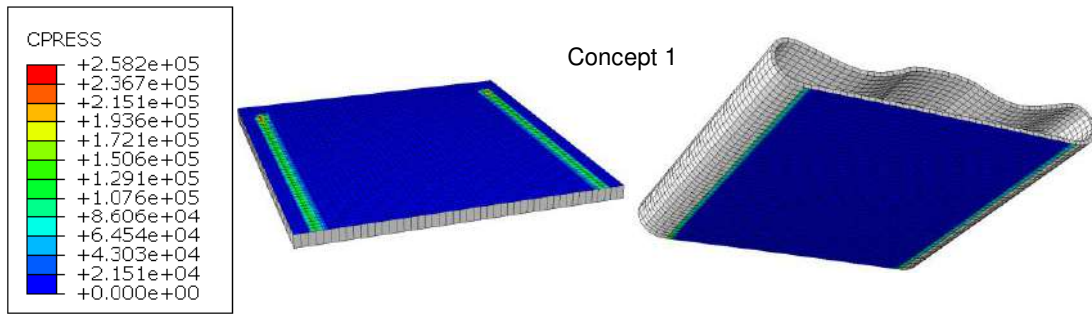
Figure 4.6: Contact pressure on plate and spring in Pa, Force transmission only in green area

When analysing spring concept 2 and 3 where the same spring shape is used but in a smaller size, very similar results are measured, as visible in Figure 4.7. The concept with the spring with a bridge structure shows also similar results.
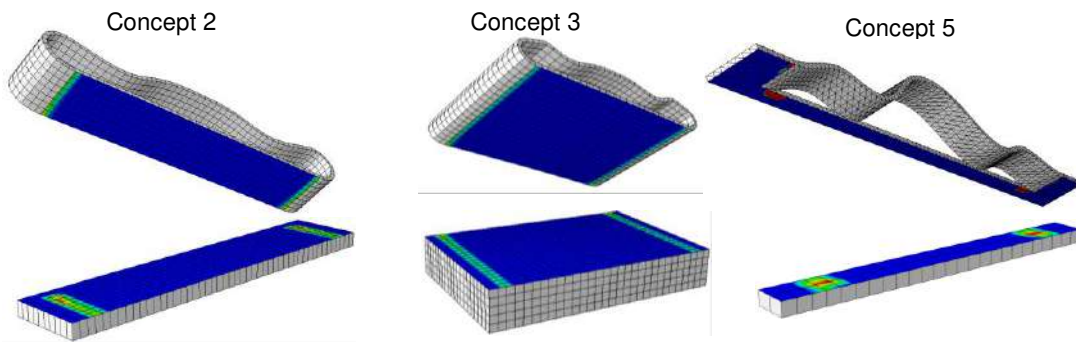

Figure 4.7: Contact pressure in concept 2, 3, 5.

To be able to make a general statement, the size of the contact pressure area is measured and compared to the complete contact area. It is visible that in each concept the complete width of the spring is in contact but only a part of the length. As example the values of the second spring concept will be given here, the remaining results are listed in Table 4.2.

The length of the total spring is 240 mm. Less the radii on both sides the flat part measures 204 mm. The places where the contact force is acting measures 10.2 mm on each side. This means that the share of the contact length is

$$f_{l,c1} = \frac{2 \cdot 10.2 \ mm}{204 \ mm} = 0.1. \hspace{2cm} 4.5$$

For the other concepts with the welded spring belt the result is also a share of roughly 10 % of the contact length. The concepts with the spring with bridge structure have a

bigger share of the contact length. The contact length in concept 5 is 35 mm on each side with a total spring length of 240 mm.

$$f_{l,c2} = \frac{2 \cdot 35 \; mm}{240 \; mm} = 0.3.$$

4.6

With these numbers the implementation of the springs can be made with 10 % of the contact length for the welded spring belts and 30 % of the contact length for the springs with bridge structure.

The springs can also be mounted by turning them upside down so that the top arc of the spring is in contact with the end plate of the fuel cell stack. For this case the force flow and the contact area are also analysed. The general boundary conditions are the same as before. In Figure 4.8 the model for this case is visible.

Applied displacement
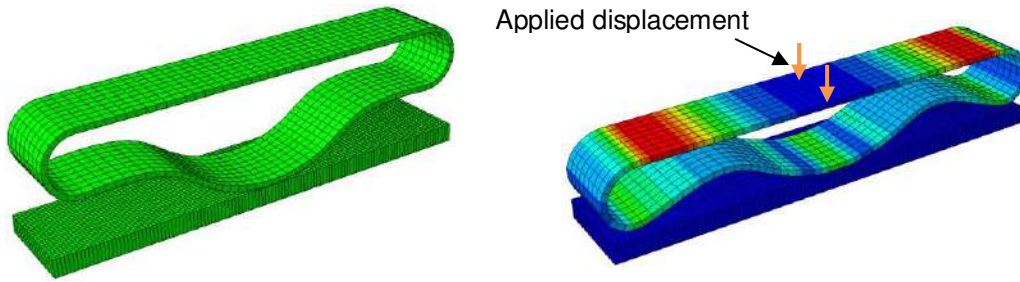
Figure 4.8: Undeformed and deformed spring with top arc in contact

The contact area this time is only at the bottom of the arc of the spring as shown in Figure 4.9. The share is calculated again exemplary for concept 2. This time the reference size is the radius of the arc with 71.3 mm whereas the length of contact is approximately 12 mm.

$$f_r = \frac{12 \; mm}{71.3 \; mm} = 0.17$$

4.7

The results for the other models are also listed in Table 4.2. Their values are as well in the range of about 20 % of the radius size so that this is considered as a good approximation. The data scatters too much to make a general statement of the share of contact length in relation to the radius but for this application it is sufficient. Apart from that the arc length was varied in different simulations to check the influence on the contact area but it didn't show any. It should also be mentioned that here there is no difference between the concepts with the welded spring belt and the one with the bridge structure.
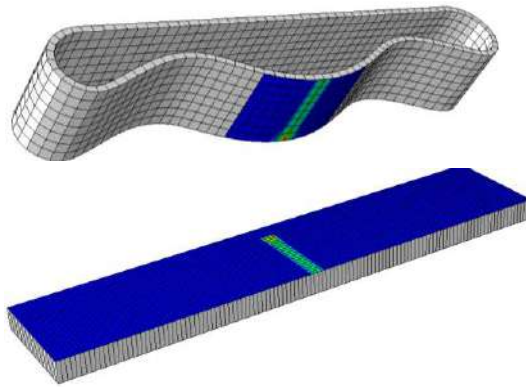
Figure 4.9: Contact pressure of concept 2 upside down

Table 4.2: Share of spring length in force transmission

	Concept 1	Concept 2	Concept 3	Concept 5	Concept 6
Share of contact length (flat side in contact with EP)	0.073	0.1	0.13	0.3	Adopted from concept 5
Share of contact length (arc in contact with EP)	0.198	0.17	0.26	0.21	Adopted from concept 5

4.2   Implementation of the fuel cell stack in FEM software

The FEM model of the fuel cell stack is based on the CAD model but it is implemented with simplifications to safe calculation resources. The simplifications are made in such a way that non-relevant information is left out so that the model is as simple as possible but at the same time as detailed as necessary. In the following section the model is explained with its properties, boundary conditions and the procedure of the simulation with its different steps.

4.2.1   Simplifications of the CAD model

The CAD model contains many different plates to simulate different states of operation as rolled out in 3.2.1. The MEA unit is the softest part, therefore it is influenced the most by the stack swelling. Through its many tasks this is the most important part with the stress profile across different planes as the central result. The bipolar plates and the end plates are important for the stress distribution but all the other parts like heating and cooling plate, current collector or insulation plate are not important for the desired results and therefore eliminated in the FEM model. The same applies for the gas supply ports on the upper end plate and the tie rods with the bolts. The tie rods will be replaced by a force to apply the pressure onto the stack.

Within the functionality of the BPP the flow field which distributes the reactants is the most important part. There are many publications that deal with stress distribution in the GDL over channel or over land in the flow field [22, 27, 51–54]. To analyse the new spring concepts the detailed look into the differences between the compression over channel or land is not necessary but rather the total stress curve between the edges of the active area. For that reason, the flow field structure is eliminated in the FEM model so that the BPP is like a flat plate apart from the manifolds and the sealing grooves. This also safes a lot of calculation time because the mesh doesn't need to take the fine structure of the flow field into account and can therefore be coarser.

Finally, all the holes in the end plates for the bolts or gas connections have been eliminated, as have the chamfers, the fillets and other inclined geometry parts that don't have a relevant function. This simplifies the mesh structure and therefore speeds up the calculation.

4.2.2   Geometry and material properties

To build up the model it is implemented in 2D first. This has the advantage that the calculation time is a lot faster. Occurring errors can be detected quicker and the corresponding boundary condition or property definition causing the error can be adapted without waiting a long time for the calculation. Another aspect to reduce the calculation time is the symmetry of the model. Only half of it needs to be sketched if a symmetry condition is applied. A screenshot of the 2D model is shown in Figure 4.10. The green parts on top and bottom are the end plates, the grey parts are the bipolar plates and the fine black

line on the lower BPP represents the MEA unit which is magnified on the right-hand side. The two sections in the light brown colour are the GDL on cathode and anode side. In the middle is the membrane with a red colour. The gasket shown in blue is inserted on the right end of the BPP in the sealing groove. On the top end of the end plate a spring is mounted representing the disc spring stack. The disc spring stack only consists of two points that are connected through a definition of the characteristic curve of the spring.
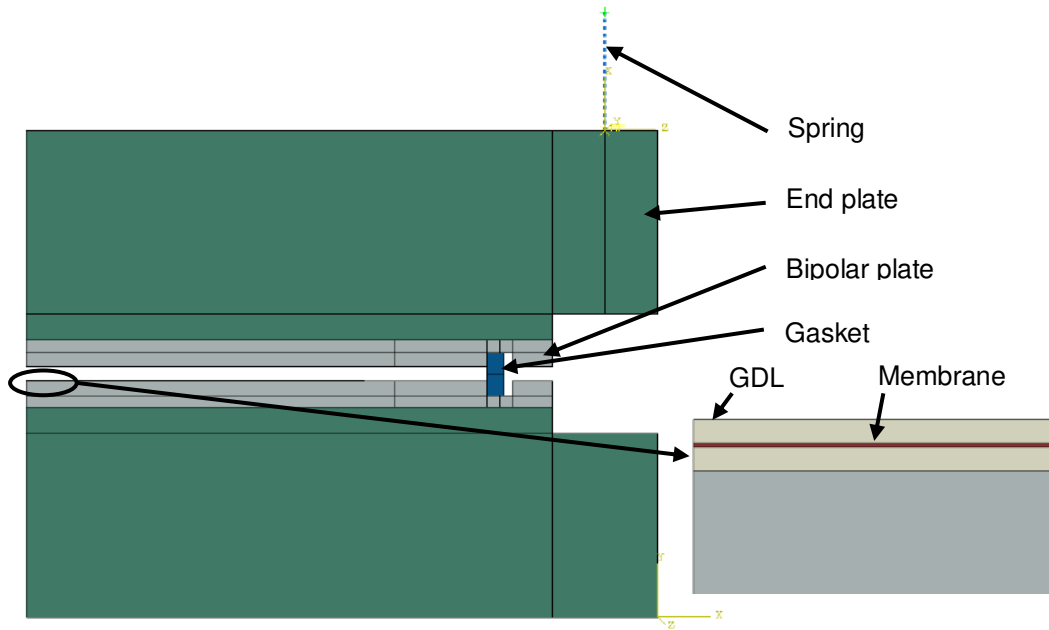
Figure 4.10: Left: 2D model of half a fuel cell, right: magnification of the MEA unit

The dimensions of the parts are taken from the CAD model. The material properties are listed in Table 4.3. The end plates are made of aluminium, the bipolar plates of stainless steel, for example steel 1.4404 (X2CrNiMo17-12-2) [19, 55]. As gasket material EPDM is chosen as already explained in chapter 3.2.2.2. The GDL is made of carbon paper. Carbon paper is a very porous material with different properties in the different planes, especially the Young's moduli vary. However, in the present case the GDL will only be compressed in vertical direction and also the results will only be relevant from this case. That's why the carbon paper can be simplified as elastic material with one Young's modulus as also done in the literature [51]. The value for the Young's modulus is taken from [9] and [56] which correspond to Toray-TGP-H-060 paper. As mentioned in [57], the Young's modulus can be transferred to the TGP-H-030 carbon paper which is used in the current model. For the membrane the material properties of Nafion® are taken. Here it is important to note that the material properties, especially the Young's modulus, are

highly dependent from temperature and relative humidity. The warmer and the more humid it is the weaker is the material. For the present project only two values are relevant. First, the ambient conditions during assembly and second, the conditions during operation mode. Tang et al. investigated the behaviour up to a temperature of 85 °C and a relative humidity of 90 % [17]. These are realistic conditions for the operation, that's why it is adopted like that.

Table 4.3: Material properties

Material	Young's modulus (MPa)	Poisson ratio	Temperature (°C)	Relative Humidity (%)	Source
Aluminium	70 000	0.33			[27]
Steel	209 000	0.3			[27]
Carbon paper	8.79	0.28			[9]
Nafion®	197	0.25	25	30	[9, 17]
	46	0.25	85	90	[9, 17]
EPDM	See Figure 3.9				

The swelling of the membrane happens during the increase of temperature and humidity. In Abaqus a coefficient for thermal expansion can be implemented but not for expansion due to humidity. That's why the two effects are combined into one artificial expansion parameter α' as also done in [54]. It can be calculated to

$$\alpha' = \frac{\frac{t_{op}}{t_{in}} - 1}{\Delta T} \qquad 4.8$$

The membrane will swell up about 14 % during the operation. With an initial thickness of 15 µm the thickness during operation is

$$t_{op} = 15\ \mu m \cdot 1.14 = 17.1\ \mu m. \qquad 4.9$$

For the calculation of α' the same temperature difference is used that is associated with the change in elastic properties, namely 60 K. With these values the coefficient is

$$\alpha' = \frac{\dfrac{17.1\ \mu m}{15\ \mu m} - 1}{60\ K} = 0.00233\ \frac{1}{K} \qquad\qquad 4.10$$

The swelling only occurs in vertical direction, therefore the expansion coefficient is implemented as orthotropic property with the calculated value in the vertical direction and 0 in the other directions.

Because it is too much effort to model the whole stack with a few hundred cells and because the calculation time would increase dramatically due to the number of contact interactions, a dummy replacement is used to substitute the whole stack and only one cell is implemented to analyse the behaviour. The dummy part gets the properties of steel as material because the biggest part of the single cell is the bipolar plate which is made of steel. The relevant behaviour of the stack is the swelling inside the active area. This will be executed and represented through the dummy part as explained in detail in the next sub-chapter.

The springs in the proposed concepts reach over the symmetry plane. According to the spring manufacturer the width but not the length is in a linear relation with the characteristic curve. Therefore, the 2D stack must be modelled completely because the spring behaviour is only given through the characteristic curve. The whole two-dimensional fuel cell model is shown in Figure 4.11.
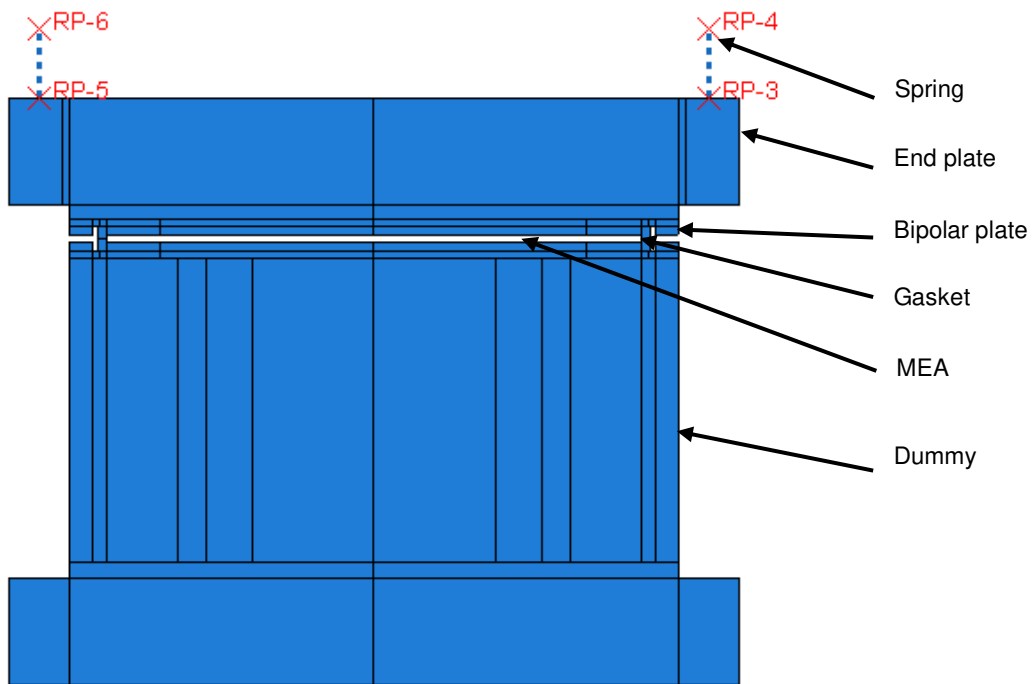
Figure 4.11: Complete fuel cell stack in 2D with dummy

As soon as the 2D model is running and there are no errors occurring during the calculation the fuel cell is also modelled in 3D. Through that, first, the gaps between the springs in the screen plane is taken into account and second, the stress distribution in the MEA can be analysed in the whole plane. The 3D model in Figure 4.12 shows the complete width of the stack because of the already mentioned reason with the springs crossing the symmetry line. However, only one half of the length is considered to safe resources. The effect on the middle spring will be considered by halving the applied force and the characteristic curve as only half the width of the spring is in action.
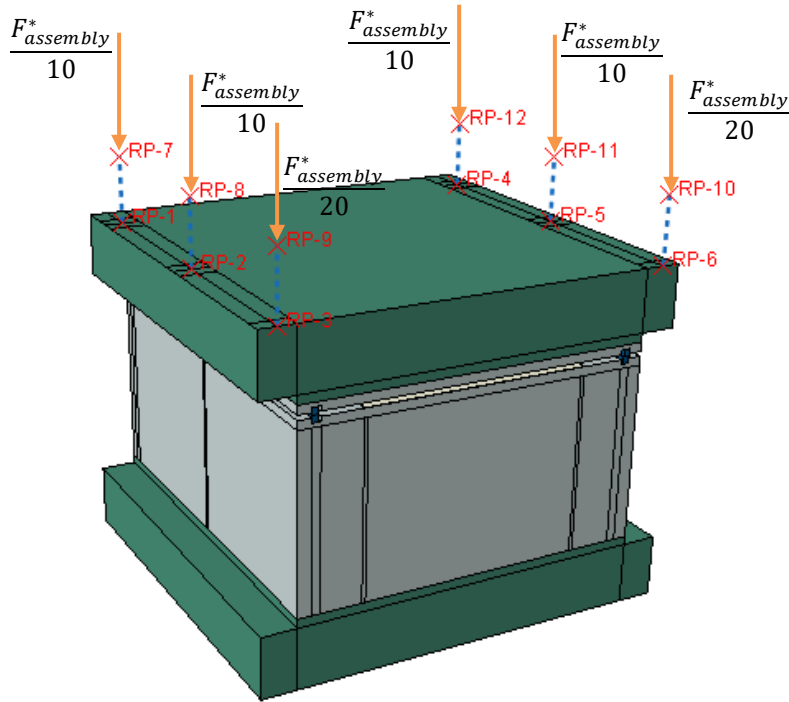
Figure 4.12: 3D fuel cell stack (here with spring system from the disc spring stack reference)

One difference between the 2D and 3D model is the implementation of the gasket. To simplify the boundary conditions all the curved parts are eliminated in the 3D model as visible in Figure 4.13. This changes the necessary force for the gasket compression. The eliminated gasket length is measured, then multiplied with the necessary compression force per centimetre from chapter 3.2.2.2 and the result subtracted from the initial compression force.

$$F_{gasket,frame}^* = F_{gasket,frame} - l_{gasket,frame,radius} \cdot f_{gasket,frame} \qquad 4.11$$
$$= 8\,594\,N - 12.56\,cm \cdot 72\,\frac{N}{cm} = 7\,690\,N$$

$$F_{gasket,manifold}^* = F_{gasket,manifold} - l_{gasket,manifold,radius} \cdot f_{gasket,manifold} \qquad 4.12$$
$$= 9\,735\,N - 27.1\,cm \cdot 87\,\frac{N}{cm} = 7\,377\,N$$

This leads to a total stack compression force of

$$F_{assembly}^* = 43\,176\,N + 7\,690\,N + 7\,377\,N = 58\,243\,N. \qquad 4.13$$

The result is already drawn in Figure 4.12.
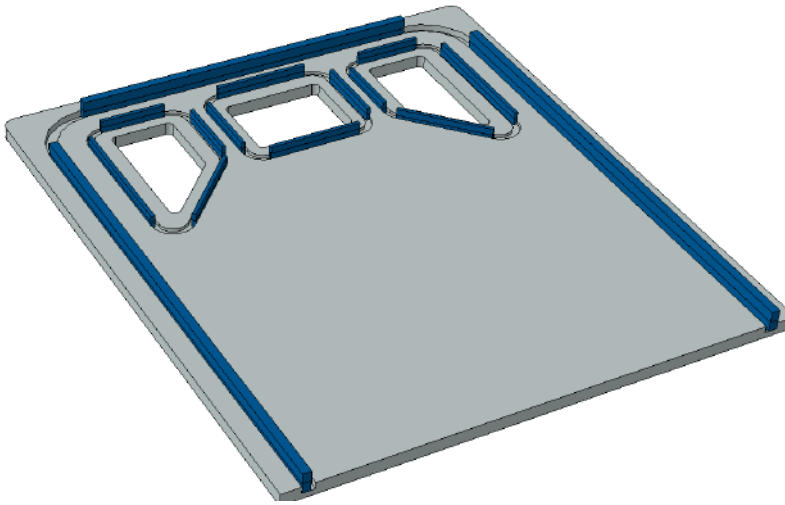
Figure 4.13: Implementation of gasket in 3D

4.2.3   Applied boundary conditions and loads

It is necessary to apply interaction conditions so that Abaqus knows how the parts be-have when they come into contact. This can be done through the option "General Con-tact" with the definition that penetration is not allowed. The general contact option detects all the surfaces that can come into contact automatically.

Furthermore, the springs need to be implemented correctly. The spring geometry itself is not given but only the characteristic curve. That's why both the top point and the bottom point is replaced through a reference point (RP). The points are connected by a wire matching the characteristic of the corresponding spring. An example is shown in Figure 4.14. The distance between the points is equal to the uncompressed spring height.
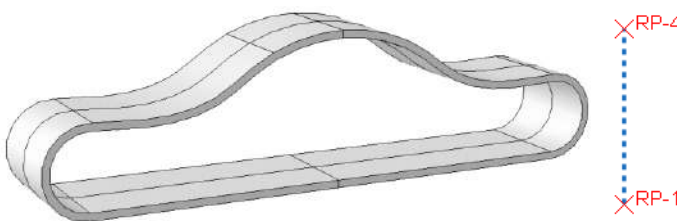
Figure 4.14: Representation of a spring in the model

Since the bottom reference point is representing a whole surface the connection to the end plate is an important implementation. In Figure 4.15 the different variants are shown.

The red area shows the part of the surface where the force flow is entering the end plate. Although the disc spring is round the connection is implemented with a square surface in accordance to the diameter (see top left image in Figure 4.15) to keep the mesh simple. The novel concepts are implemented according to the results in chapter 4.1.2. The bottom point of the spring and the surface belonging to each point are connected through a rigid body constraint that transfers the movement of the reference point to the end plate.
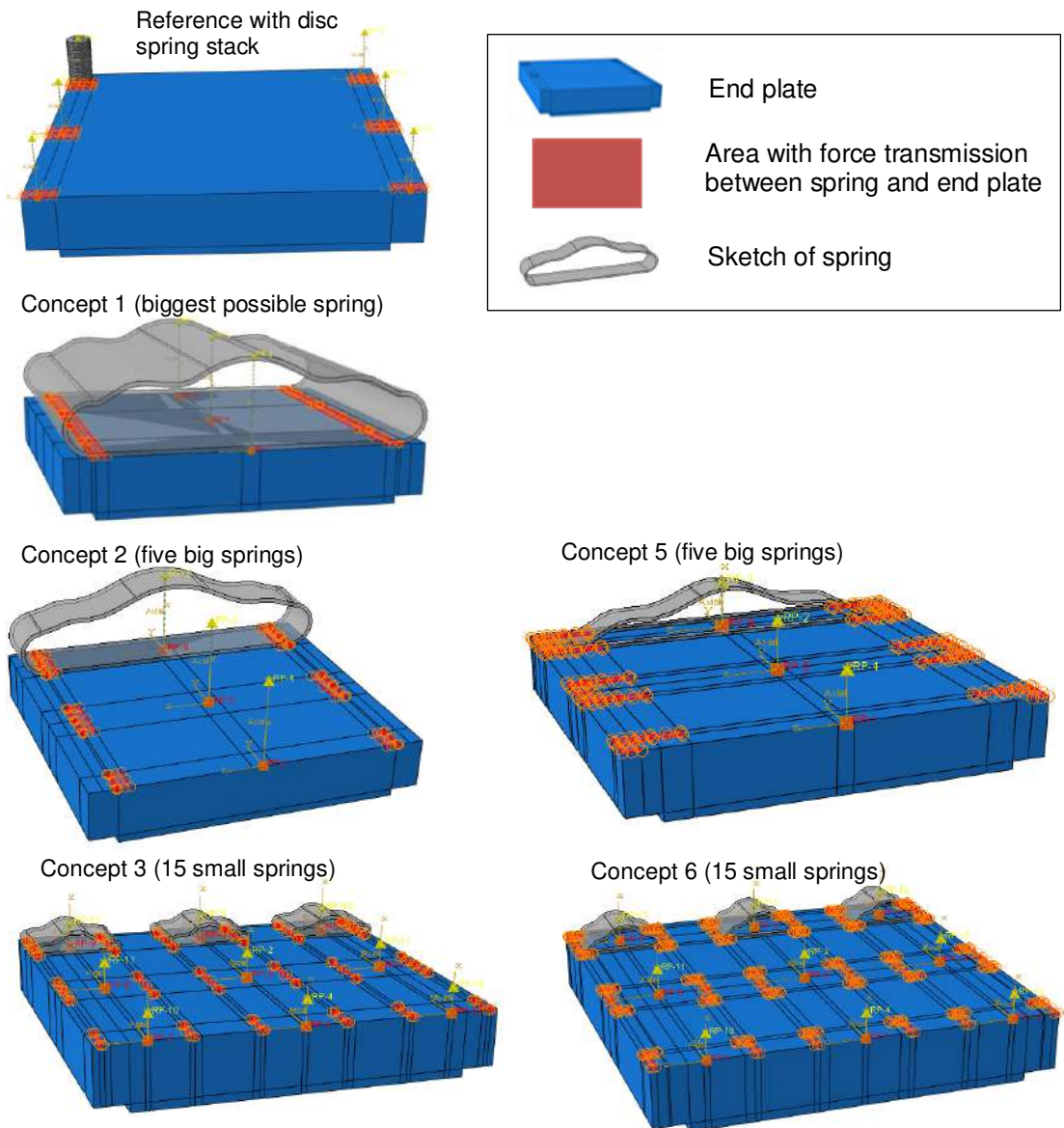
Figure 4.15: Connection between spring concept and end plate with indicated spring sketch

Although the spring of concept 1 is the largest possible spring in size of the end plate it is designed with two and a half spring characteristics over the half model in order to be able to apply the loads at the appropriate place of the assembly belts. The characteristic curve of the spring is divided accordingly by 5, or by 10 with respect to the half spring, to distribute the force correctly.

In the case that the springs are turned by 180° so that the arc is in contact with the end plate the connected area also changes. Representatively the case for spring concept 2 is shown in Figure 4.16.
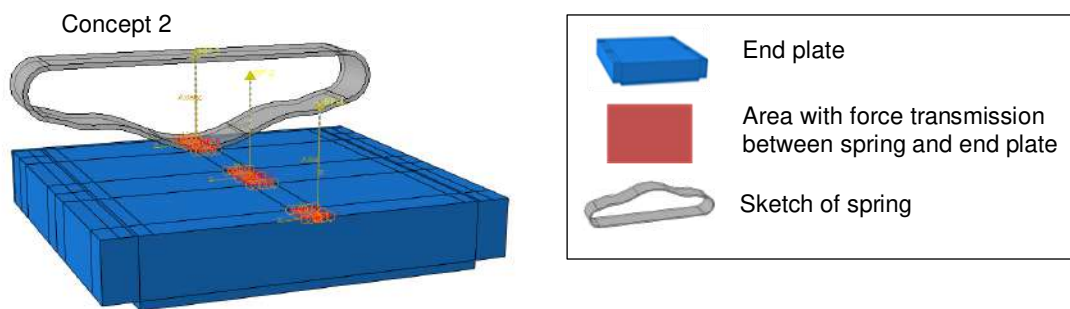
Figure 4.16: Connection between spring and end plate with spring upside down

The following boundary conditions are applied to control the movement of the parts. During all the steps there are five general conditions.

1) Bottom end plate is fixed in all directions

2) Symmetry condition in cutting plane because only half the length is modelled

3) No sideways movement to prevent sliding (there is no friction definition of its own to safe calculation resources)

4) Edges of the MEA are fixed representing sub-gasket

5) Constraint at top of the spring i.e., the top reference point, to allow only vertical compression

As the material properties of the membrane are temperature dependent, a temperature field of 25 °C is applied to the membrane section.

The gasket between the bipolar plates has a few constraints as well. One side of each simplified gasket part is from the beginning in contact with the sealing groove and held there to accelerate the calculation. Without that it would slide back and forth. Also, each end is constrained so that it can't extend. With the complete gasket this wouldn't be necessary but due to the missing radii the gasket would otherwise lengthen erroneously.

The whole simulation is divided into four steps which are described below.

1) Gasket is compressed between bipolar plates

   o Upper end plate with springs and upper BPP are pushed down by 2.4855 mm until gasket is compressed in sealing groove

   o BPP comes into contact with MEA

   o Lower BPP is fixed in its position to prevent further contact calculations to save calculation time

2) Dummy step to establish contact between parts for faster convergence

   o Lower BPP is pushed down by 1 µm, MEA by 10 µm and upper end plate by 5.5 µm

   o Contact force between parts rises and accelerates the following step

3) Assembly force is applied to achieve necessary contact between GDL and BPP and to keep gasket deformed

   o Previous displacements are disabled and replaced through load

   o Total modified stack compression force F* (58 000 N) is applied on top of the springs

      ▪ Model with *disc springs*: 5 800 N on each complete disc spring stack, half the force, 2 600 N, on springs in cutting plane

      ▪ *Concept 1* (single spring) and *concept 2 and 5* (five big springs): 11 600 N on complete springs, 5 800 N applied on halved spring in cutting plane

- *Concept 3 and 6* (15 small springs): 3 866.67 N on each complete spring, 1 933.33 N on halved springs

4) Operation mode, swelling of the stack is happening

- o Forces are deactivated, top of the springs are fixed in their current position to maintain spring compression and thereby assembly force

- o Dummy receives a displacement of 0.96 mm in the active area simulating swelling of the whole stack (see Figure 4.17)

  - 2 mm on each side of the active area are spared because of lamination with sub-gasket where the membrane won't expand

  - Bottom part of dummy is fixed in its position to keep contact between lower end plate and dummy

- o Temperature field on membrane is raised to 85 °C

  - Changes mechanical properties and expands membrane

- o Swelling will also be applied to the area of the gasket on the dummy, because with the swelling of the membrane the gasket will slightly relax.

  - Relaxation of gasket in single cell measured in 2D model (1.81 μm). Multiplied with number of cells (456), total gasket relaxation of 0.83 mm through the whole stack occurs in sealing area
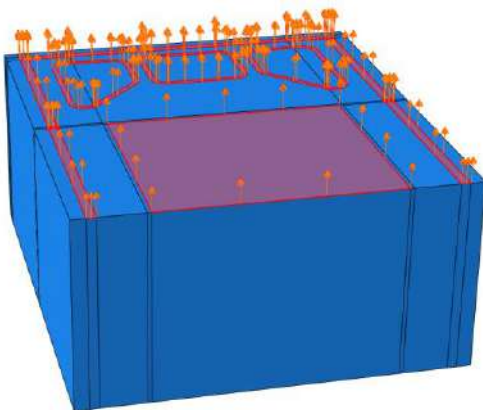
Figure 4.17: Boundary condition for the swelling on the dummy

4.2.4   Meshing

One of the key factors for useful results is the meshing of the parts. In general, it can be said the finer the mesh the more detailed are the results. At the same time the calculation time increases with a higher element number. This means, that only in relevant places a fine mesh is sensible. In the present project the compression of the GDL delivers the desired statement about the effect of the spring. That is why a high number of elements for the area of the MEA is chosen. The thickness of the MEA is represented with only three elements, one for each GDL and one for the membrane, because there is almost no difference of the compression results with a higher element number. The gasket is meshed very finely as well because it undergoes high deformation through the compression. The end plates, the dummy and the BPPs have a coarser mesh because little deformation is expected. In the dummy the mesh becomes finer towards the edges of the swelling area to distribute the stress inside the part better.

The whole 2D model except the gasket is meshed with plane strain elements called CPE4R since the out-of-plane strain is zero. The gasket requires a hybrid form of this element, CPE4RH, due to the hyperelastic material which is assigned to it. Because it is a plane cut through the fuel cell all elements are quadrilateral. To get correct results the thickness of the elements into the screen plane needs to be specified. The default value is 1, it needs to be adapted in the section assignment in order to be consistent with the chosen units. The elements of the end plates have a thickness of 0.454 m, the ones of membrane and GDL 0.224 m and for the BPP 0.45 m. The gasket elements are also assigned to a thickness of 0.45 m for simplicity reasons. The full gasket cannot be represented anyway due to the region around the manifolds which is not represented in the 2D model.

In the 3D model all the parts except BPP and gasket are meshed with C3D8R elements, a hexahedral element with 8 nodes. The gasket has the same hyperelastic material so it again needs the hybrid form of this element, C3D8RH. The BPP cannot be meshed with the hexahedral elements but needs tetrahedral elements because of the manifolds. This element type is called C3D10. The meshed model is shown in Figure 4.18.
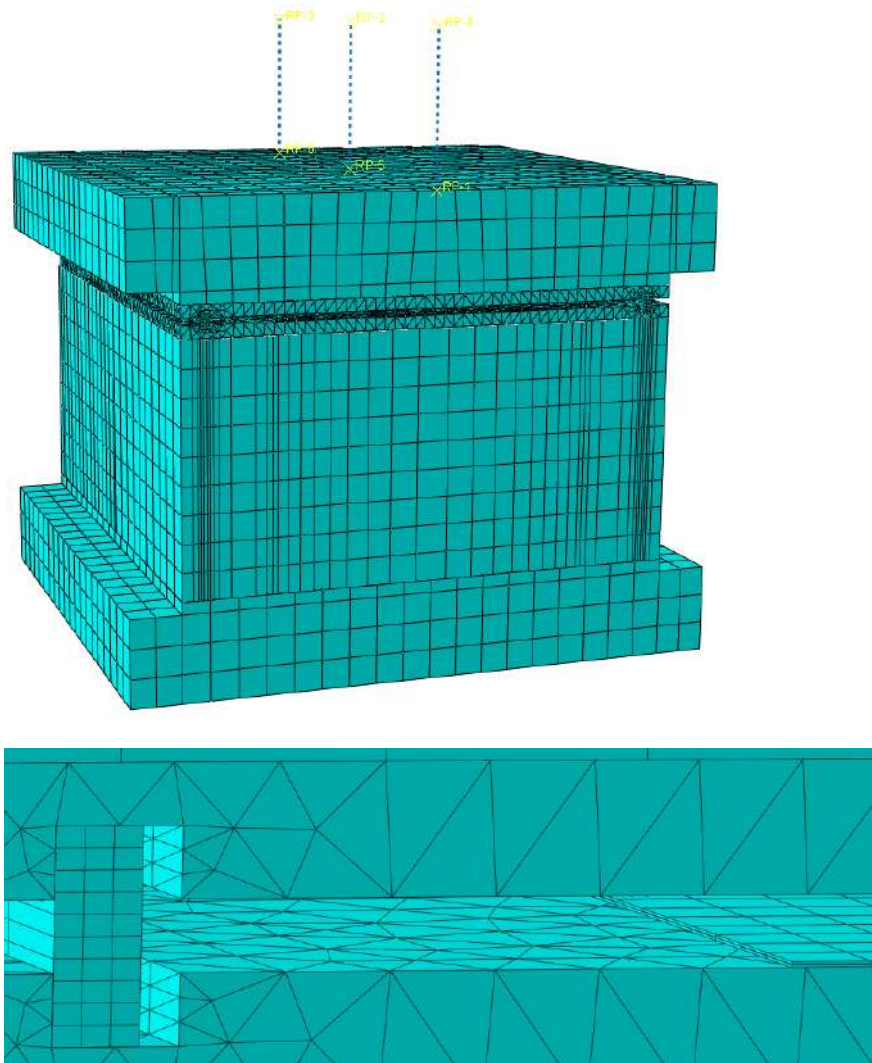
Figure 4.18: Meshed 3D stack with detailed view on gasket and MEA

5 Execution of experiments

Simulation speeds up the process of development but the obtained results need validation in order to confirm the values in a qualitative or quantitative way. The validation is made in an experiment where the model from the simulation is built on a test bench to see, if the applied boundary conditions, loads and the thereby achieved results are correct. In this chapter first three conceptual ideas are presented on how the springs can be tested in an experiment without building up a whole fuel cell stack. Afterwards, the setup with the chosen concept is explained.

5.1 Concept development

The goal is to design a setup in which the spring concepts can be tested to see how they behave during the assembly process and the operation mode. As result the stress distribution across the GDL will be taken as in the simulation model. The experimental model should be quite similar to the simulation model, so there are the springs on the top of the end plate, a single fuel cell with bipolar plate, gasket and MEA, a unit for the stack swelling during operation and a bottom end plate. The parts will be stacked on a press and the assembly pressure is put on with a stamp. The task of the experiment concept development is to come up with an easy solution of how the swelling can be reproduced. There are three ideas that will be explained.

The first idea is to install a unit inside the setup with the effect of a toggle lever press. A principle example is shown in Figure 5.1. This is inserted between the lower end plate and the BPP, whereby its size must correspond to the size of the active area. Assembly pressure is applied and the parts are fixed in position, then the mechanism is actuated so that the toggle extends with the value of the stack swelling. This method has the advantage that the assembly process and the swelling can be done in one pass without having to open and restructure the assembly. Also, the value of the swelling can be achieved quite accurate depending on the design of the toggle lever press. A major disadvantage is the construction effort and the production time, both of which are quite high.

Figure 5.1: Schematic principle of toggle lever press [58]

A second idea is a screwable element underneath the active area to simulate the swelling. A sketch is shown in Figure 5.2. Between the lower end plate and the BPP, a dummy part is placed with a pocket inside in the size of the active area. Here a second part is inserted sitting on a bolt which is lead through a hole in the end plate. A nut on the bolt can be turned to lift the central plate in the amount of the stack swelling. How far the nut needs to be turned can be calculated through the thread pitch. The advantage here is that the construction and production effort is less than in the first proposal. It also is possible to execute all the experiment steps in one pass. On the other hand, the plate in the pocket can tilt during the screwing process and the pressure exerted on the BPP is very punctual which can distort the results of the pressure distribution in the MEA.
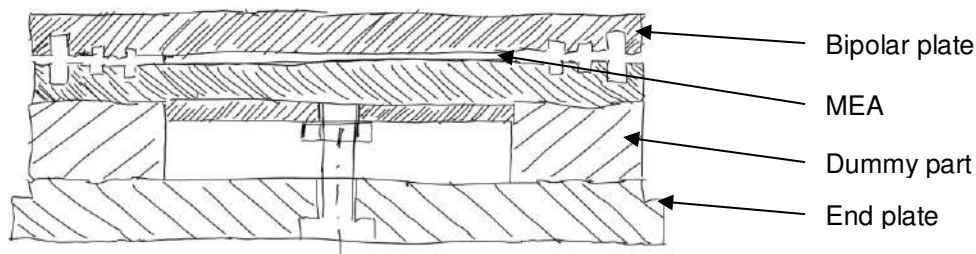
Figure 5.2: Sketch of screwable element

The last concept divides the assembly and the operation process in two separate steps. First, the end plates and BPP with MEA and gasket are assembled with the necessary force. Because the spring characteristic is given the force and the corresponding displacement of the assembled state are known. The parts are disassembled and an extra plate in the size of the active area inserted underneath the BPP to allow bending of the BPP and the EP in case that it occurs. Then a new force is applied on the springs which can be obtained by adding the displacement of the stack swelling i.e., 0.96 mm to the initial assembly displacement. The parts need to be compressed a second time with the corresponding higher force to see the results of the operation mode. A basic sketch of

the spring characteristic is shown in Figure 5.3 with the relevant forces and displacements and their intersections with the characteristic curve.
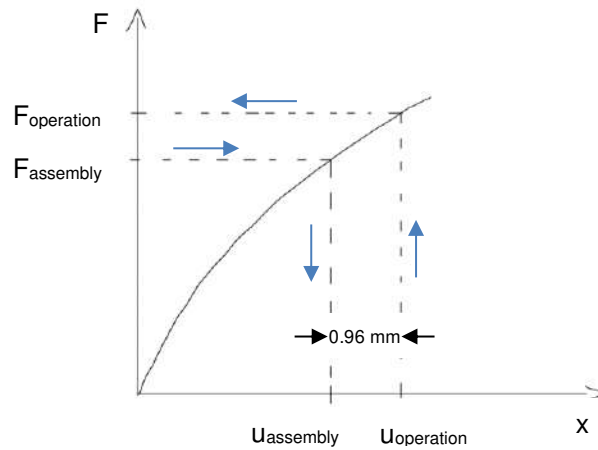
Figure 5.3: Spring characteristic with relevant points

The disadvantage here is that the setup has to be opened between the assembly and the operation mode to insert the extra plate. The advantage is that it is easy and requires little preparation. The advantages and disadvantages of the proposed concepts are summarised in Table 5.1. Due to the simplicity of the third proposal this is chosen to be realized.

Table 5.1: Comparison of experiment concepts

	Advantage	Disadvantage
Toggle lever press	- Assembly and swelling in one step - Swelling value quite accurate	- Very high construction and production effort
Screwable plate	- Construction and production effort is reasonable - Assembly and swelling in one step	- Plate can tilt while adjusting - Exerted pressure very punctual
Force increase based on spring characteristic	- Very easy setup - Few preparations necessary	- Assembly and swelling in two steps

5.2   Experimental setup

The experiment setup is shown in Figure 5.4. The assembly is mounted in a press. On the bottom there is the end plate, followed by a plate representing the expansion. The next part is one half of a bipolar plate with the sealing grooves and the gasket. In the experiment, only the outer frame gasket and the ones around the central manifold channel are implemented because the others are not available. In the centre of the BPP the GDL is positioned, on top is a pressure-sensitive film or alternatively a pressure sensor plate to receive digital results. Above this is the second end plate with the springs. Because the stamp of the press is not big enough to cover all the springs a pressure plate is needed that transfers the force from the stamp to the springs.
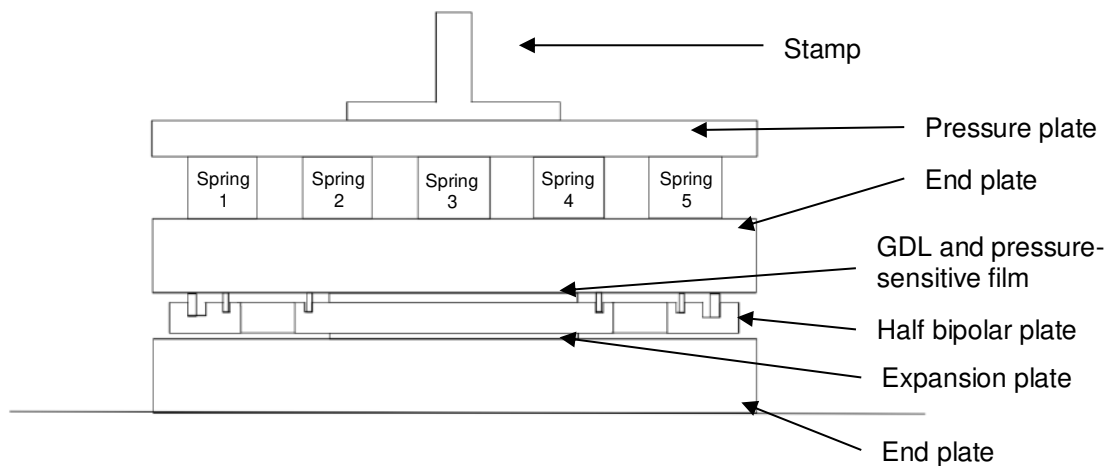
Figure 5.4: Sketch of experimental setup

To keep the springs in their position a guiding element (Figure 5.5) is constructed that can be plugged on the top end plate. For smaller springs the slots can be separated through small plates.
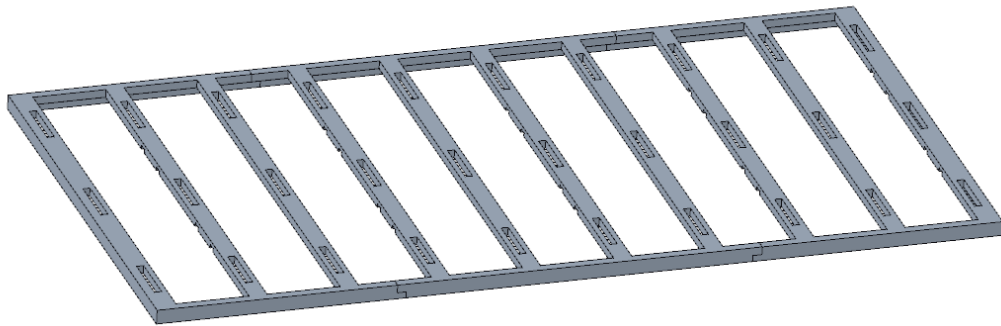
Figure 5.5: Guiding element for springs

The setup where the flat part of the springs is in contact with the end plate is exemplary with variant 3 shown in Figure 5.6. For the alternative with the arc of the spring in contact with the end plate, the setup is shown in Figure 5.7.
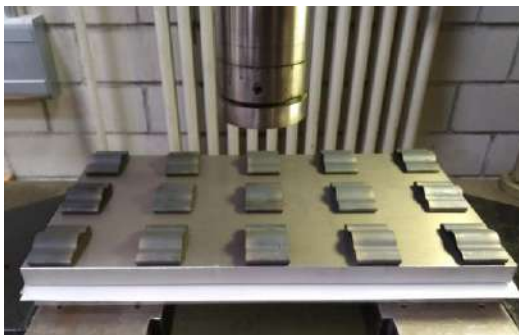
Figure 5.6: Experimental setup with flat part of the springs in contact with EP

Figure 5.7: Experimental setup with arc of the springs in contact with EP

To represent the case with the disc spring stack, some washers are put in the position of the tie rods as shown in Figure 5.8, then the pressure plate is added on top. Through that the force flow is similar as in a stack with tie rods.

Figure 5.8: Washers to represent the case with disc spring stacks on the tie rods

The upper end plate and the pressure plate exert a pressure with their tare weight but because their mass is about 15 kg which is equal to 147 N there is no need to take this into account in comparison to the high forces that are necessary for the compression.

The press has a hydraulic stamp. The force can be read from a pressure gauge but the accuracy is only +-1.5 tons which is equal to about 15 kN. This is why a differentiation between the force of the assembly mode and the force during operation is difficult to realise. Because due to the linear spring characteristic of the tested concepts the qualitative results between assembly and operation don't differ, the decision is taken, to apply the force only once in the range of the assembly force.

Another point to bear in mind is, that the pressure sensor can measure up to 2 MPa. Most values in the simulation are in that range, but the extreme values in the corners go up to 4-5 MPa. Because the sensor software displays a real-time value of the measured pressure, there is direct feedback. This makes it easy to protect the hardware by not increasing the force further when the maximum value is measured. Apart from that it is important to mention that two sensor plates are necessary to cover the complete active area. They are shown in Figure 5.9. This is why in the middle there is a small stripe without results.

Similar to the digital sensor, the pressure-sensitive film is suitable for a pressure range between 0.5 and 2.5 MPa. Pressure below the minimum can't be detected whereas the colour above the maximum value doesn't intensify further. An advantage of the pressure-sensitive film (fuji film) is, that it can be cut in a way that it also covers the complete gaskets as visible in Figure 5.10.
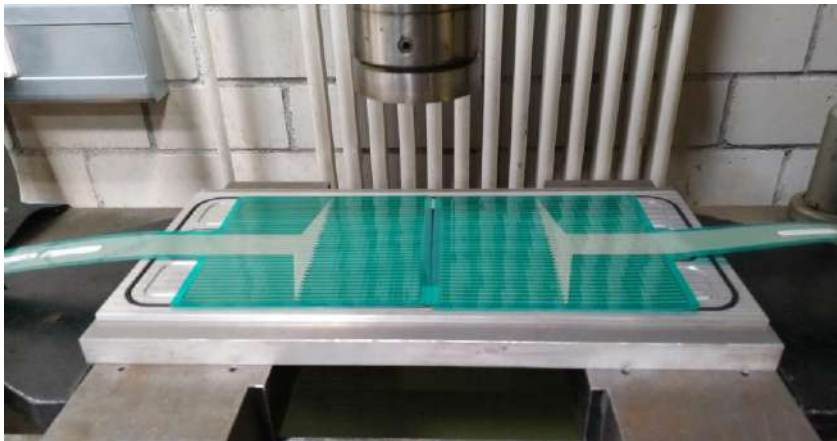
Figure 5.9: Pressure sensors on BPP
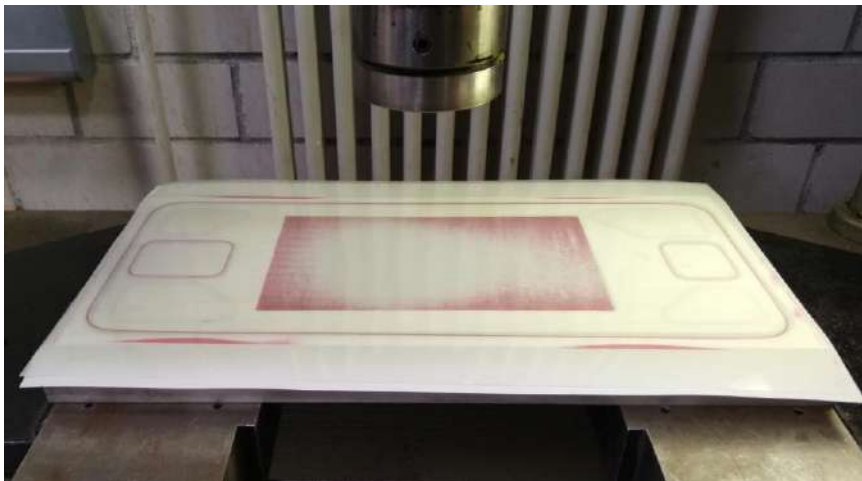
Figure 5.10: Pressure-sensitive film on BPP

6   Results and discussion

To decide, whether the simulated spring concepts bring an improvement in context with the stress distribution along the active area and also with respect to the increase of the stress due to the swelling, the stresses in compression direction in the GDL are measured and compared with each other. First, the results of the simulation of the five proposed spring concepts are presented and explained. The two best spring concepts are produced to be tested experimentally, the outcome of which is presented in the second part. At last simulation and experiment are compared and discussed to draw general conclusions.

6.1   Results of the simulation

As rolled out before, the springs can be implemented with their flat side on the end plate or turned around by 180° with the arc shape on the end plate. First, the results with the flat side down are presented, and then the results with the arc shape down. At last, some parameter changes are made to the model to examine how the behaviour changes.

6.1.1   Flat side of spring in contact with EP
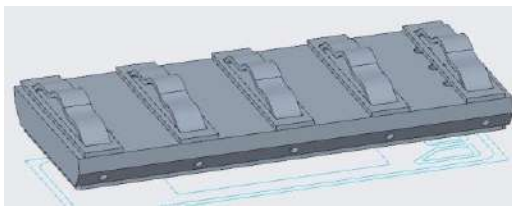
Figure 6.1: Flat side of spring showing to the end plate

The stresses on the GDL surface are distributed over the active area. With the flat side of the spring showing downwards as illustrated in Figure 6.1 and the force flow entering the end plate on its edges, the highest stresses are expected to be as well on the edges of the GDL. This turns out to be a correct consideration, an exemplary stress distribution before the stack swelling is shown in Figure 6.2.

The blue, short arrows show stresses in the range of a little less than 1 MPa, the red, long arrows in the back corners represent a little bit more than 2 MPa. There is a slight dip in the cross-section and a more pronounced one in the longitudinal section. To be

able to compare these in two-dimensional diagrams the stresses in both the cross and longitudinal section are plotted in the middle and on the edge of the GDL as illustrated in Figure 6.3. In the centre dominate the small stresses whereas on the edges the extreme values are found. Because only half the fuel cell is modelled in Abaqus, the middle of the cross-section lies on the front edge of the model. The plots are made after the assembly and also after the swelling to analyse the stress compensation of each spring concept.
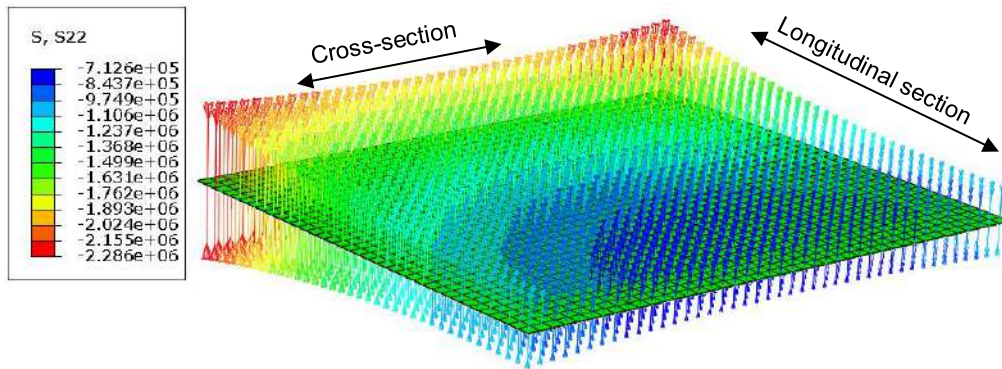
Figure 6.2: Three-dimensional stress distribution in GDL of concept 1 after the assembly
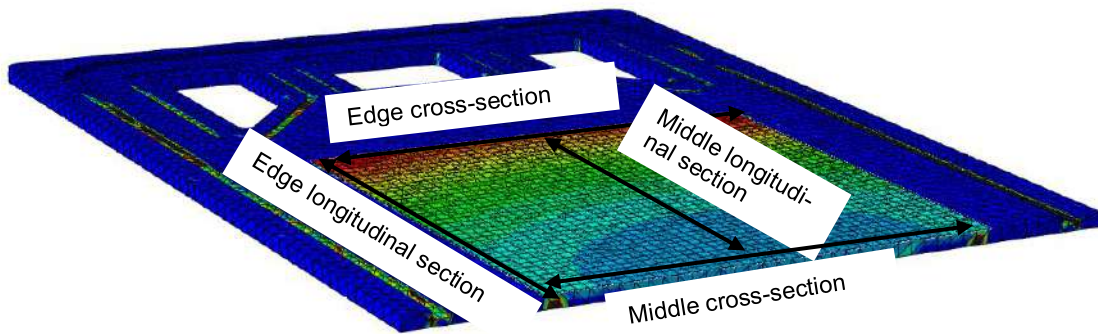
Figure 6.3: Plotting paths for stress curves

The stress distribution in the cross-section in the middle is shown in Figure 6.4 after the assembly and in Figure 6.5. during the operation. As reference the stress distribution of the solution with a disc spring stack is drawn as well. On the one hand it is clearly visible that all the graphs from variant 1 to 6 lie in a similar stress range. The proposed concepts have a flatter course than the disc spring stack and also the increase from assembly to operation is not as high. On the other hand, there are distinctive differences in the course of variant 3 and 6 in comparison to 1, 2 and 5.
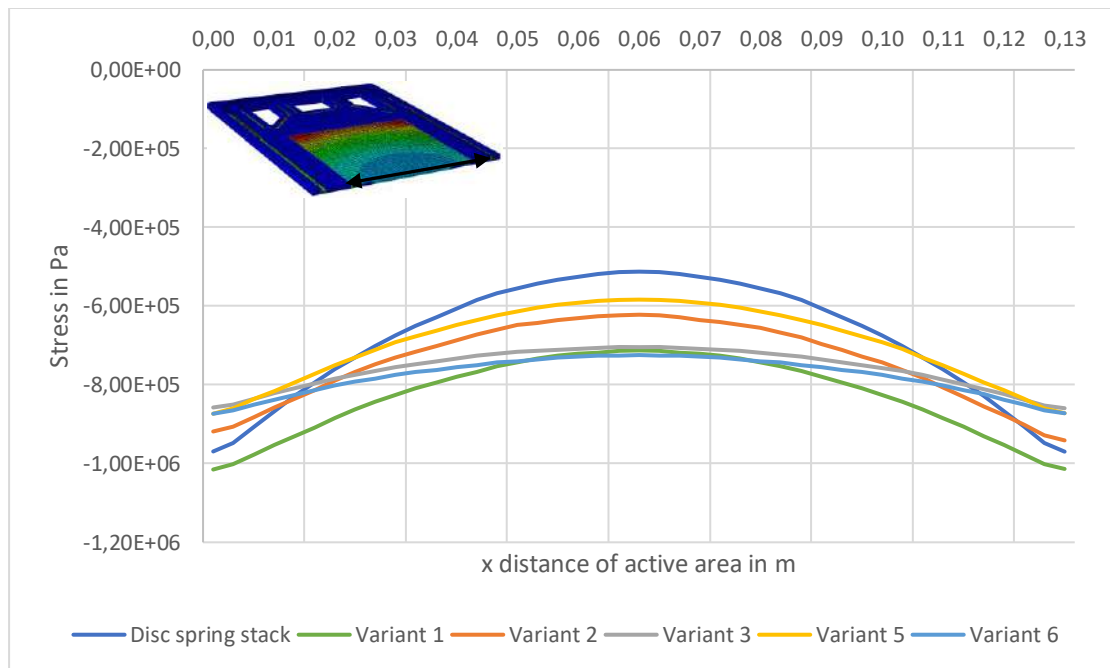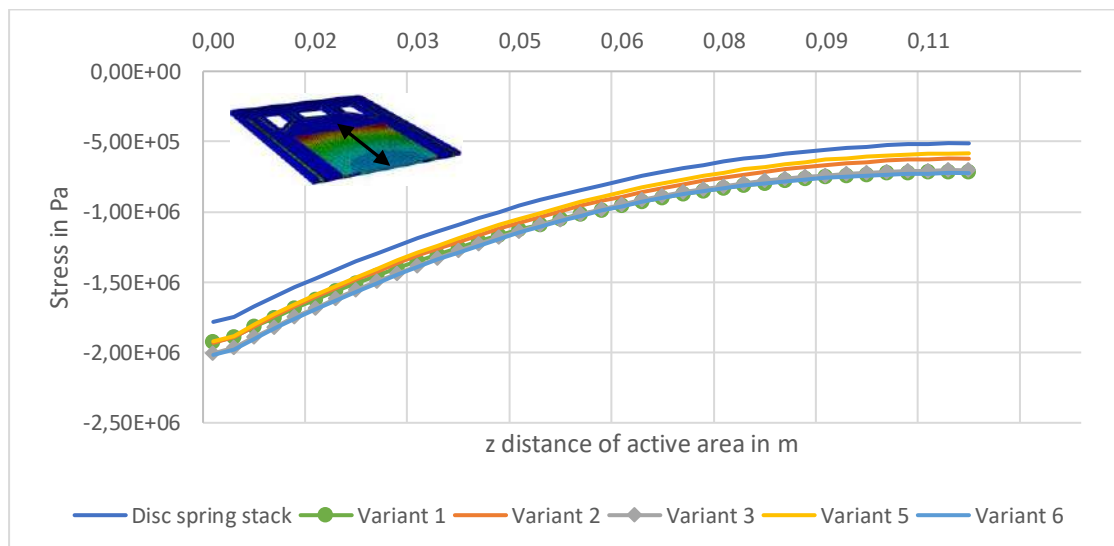
Figure 6.4: Stresses in cross sectional cut in the middle of GDL after assembly
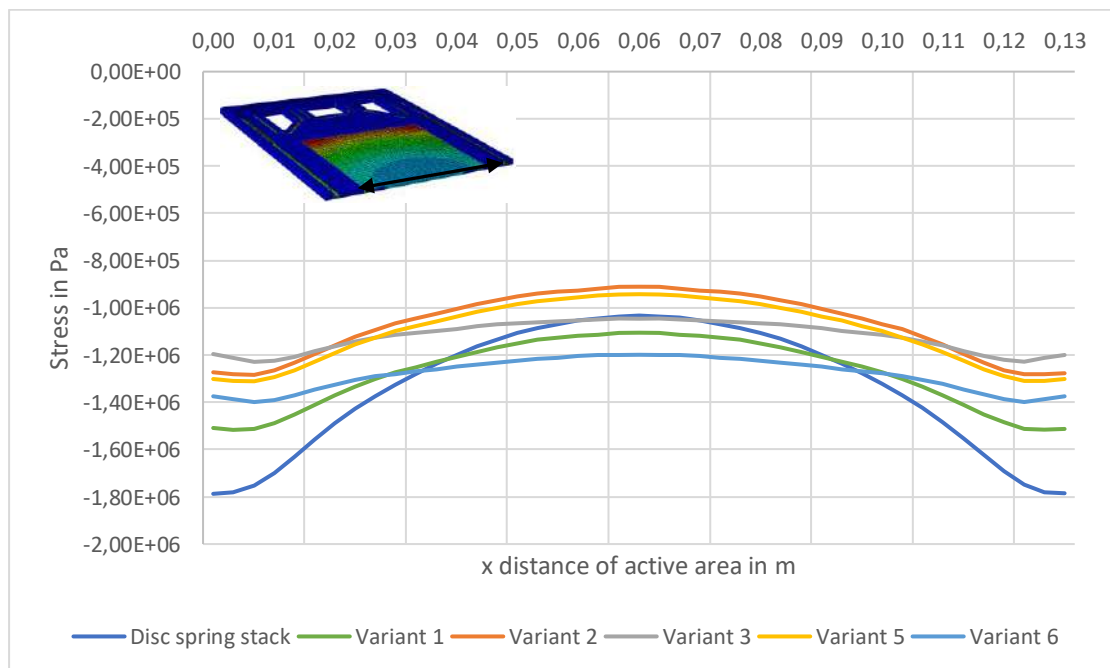
Figure 6.5: Stresses in cross sectional cut in the middle of GDL during operation

In Figure 6.6 on the left the flatness of the stress distribution is shown, which is defined by the difference between maximum and minimum stress. On the right the stress

65

increase is illustrated calculated through the differences of the stress averages of assembly and operation.
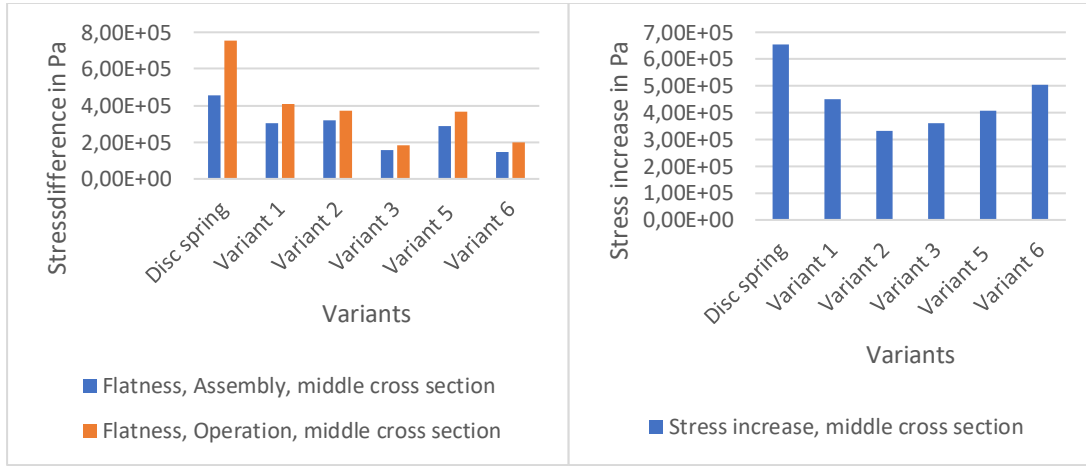
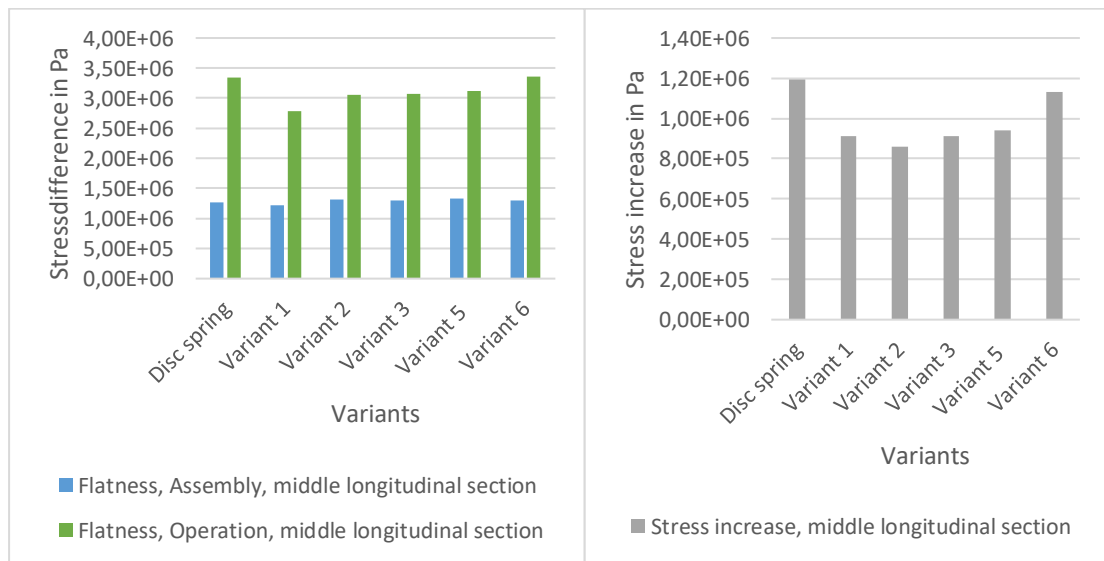
Figure 6.6: Flatness of the stress distribution (left) and stress increase (right) in the middle along the cross-section

First of all, all the new spring concepts have a better distribution than the reference solution with a disc spring stack. Apart from that, it is obvious that the third and sixth concept have the flattest distributions with up to 0.2 MPa stress difference whereas variant 1, 2 and 5 are in a very similar range to each other with around 0.4 MPa during operation. The reason for that is the bending of the end plate over the width based on the torque acting on it. As visible in Figure 6.7 a rough estimation of the torque in concept 1, 2 and 5 is

$$M_{1,2,5} = \frac{F}{2} \cdot 96.9 \, mm = 48.45 \, F \cdot mm \qquad 6.1$$

whereas the torque for concept 3 and 6 is about

$$M_{3,6} = \frac{F}{6} \cdot (24.9 + 65.1 + 114.9) mm = 34.15 \, F \cdot mm. \qquad 6.2$$

The smaller end plate bending in concept 3 and 6 leads to a more even compression of the GDL resulting in a flatter course.
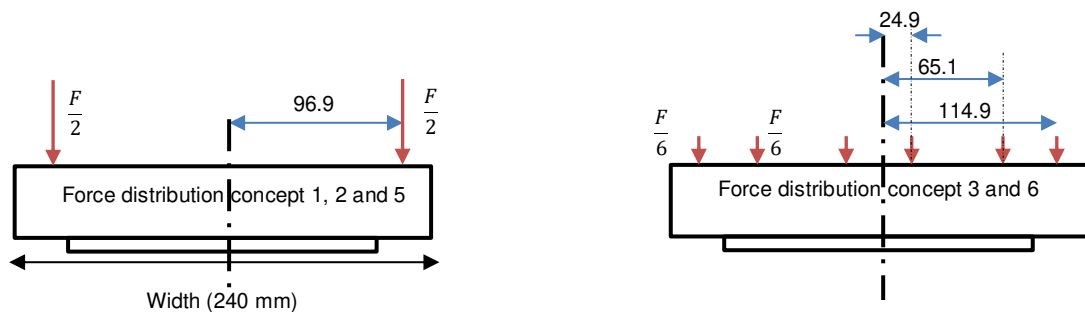
Figure 6.7: Force distribution over end plate

Regarding the stress increase from assembly to operation it is first also important to mention, that the proposed concepts show a smaller increase than the disc spring stack. Variant 2 has the smallest increase which is surprising because regarding the spring characteristics variant 6 has the most degressive course as introduced in Figure 3.13. With a degressive course a smaller force increase and therefore a smaller stress increase in the GDL is expected. A closer look to the values of the spring characteristic gives the explanation. The relevant forces are shown in Table 6.1, a detailed table with all the values can be seen in Appendix A. In concept 2 there is in the assembly a spring compression of 1.99 mm with a force of 11 600 N. With the stack swelling of 0.96 mm the spring compression increases to 2.95 mm leading to a force of 17 300 N during operation. Regarding concept 6, the force per spring increases from 3 866.67 N during the assembly to 6 340 N during the operation. To compare the two concepts the forces of the three springs per row in concept 6 have to be summed up, which is equal to 19 020 N in one row. The higher force of concept 6 during operation explains the rise of the stress.

Table 6.1: Chosen spring forces for disc spring reference and concept 1-6

	Disc spring	Variant 1	Variant 2	Variant 3	Variant 5	Variant 6
Assembly force per spring (N)	5 800	58 000	11 600	3 866.67	11 600	3 866.67
Operation force per spring (N)	10 670	86 920	17 300	5 800	17 680	6 340
Operating force per row (N)	21 340	17 384	17 300	17 400	17 680	19 020

All the concepts behave according to this except concept 1 with the big single spring. Compared to variant 3 and 5 it has a smaller force increase but a greater stress increase

in the middle of the cross-section. As rolled out later in Figure 6.13 and Table 6.2, on the edge concept 1 has the smallest stress increase which also means the end plate bends less. This is because of the big size of the spring and the thereby better distributed force along the length of the stack.

Figure 6.8 and Figure 6.9 give a closer look at the stress distribution in the longitudinal section. It is visible that the qualitative course is very similar to the course in the cross-section with the maximum stress at the edge with values of 2 MPa after assembly and up to 4.5 MPa during operation and the lowest values in the middle of the GDL with 0.5-0.8 MPa after assembly and about 1.5 MPa during operation. The absolute values of all the concepts, including the reference with the disc spring stack, lie very close to each other.

Figure 6.8: Stresses in longitudinal sectional cut in the middle of GDL after assembly
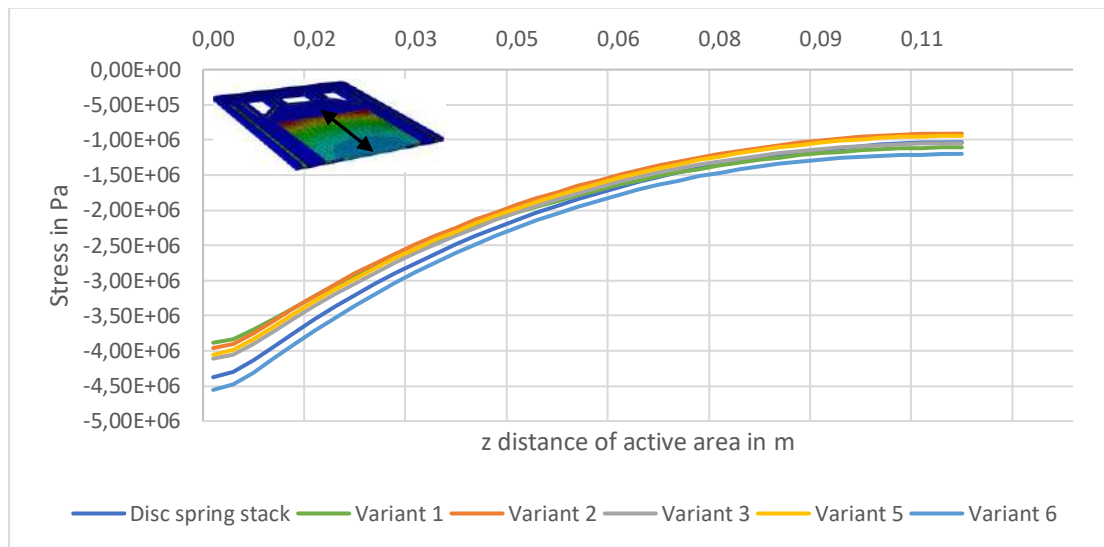
Figure 6.9: Stresses in longitudinal sectional cut in the middle of GDL during operation

Again, the flatness and the increase of stress between assembly and operation are shown in a bar diagram in Figure 6.10 to analyse the difference better.

Figure 6.10: Flatness of the stress distribution (left) and stress increase (right) in the middle of the GDL along the longitudinal section

With respect to the flatness there is no big difference between neither the novel concepts nor the disc spring stack and the absolute values are quite high with values of 1 MPa after assembly and up to 3 MPa during the operation. The reason for this is also the bending of the end plate, this time over the length. As illustrated in Figure 6.11, the end

plate deforms with the assembly load, the position of which is given by the assembly belt position which is the same in all concepts. This explains the similar result range of all concepts. The bending leads to a higher compression of the GDL on its edges which is intensified by the swelling which only happens in the active area in the centre of the end plate. This explains the high absolute values of the stress difference in the longitudinal section.
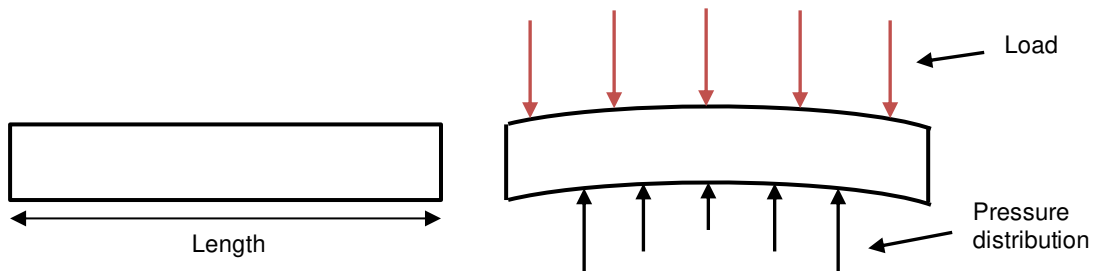
Figure 6.11: End plate shape without load (left) and with load (right)

Regarding the average stress increase from assembly to operation there is a similar qualitative course as in the cross-section. The proposed concepts have a smaller increase than the disc spring with values of 0.86 MPa to 1.13 MPa. Here also the absolute values are higher than in the cross-section. This is because the higher extreme values on the edge lead to a higher average increase.

A look to the stresses on the edge in the cross-section shows very extreme values as well with the disc spring stack reaching values up to 5.4 MPa during operation and the new proposed concepts up to 4.9 MPa. The distribution for both assembly and operation can be found in Figure 6.12. In Figure 6.13 the flatness and the stress increase are shown for the edge of the GDL in the cross-section. The flatness of the concepts 3 and 5 with the 15 small springs is better because of the force flow which is better distributed. The stress increase from assembly to operation shown in the right diagram is quite high with values of around 2 to 2.5 MPa. This is also due to the bending of the end plate as rolled out before.
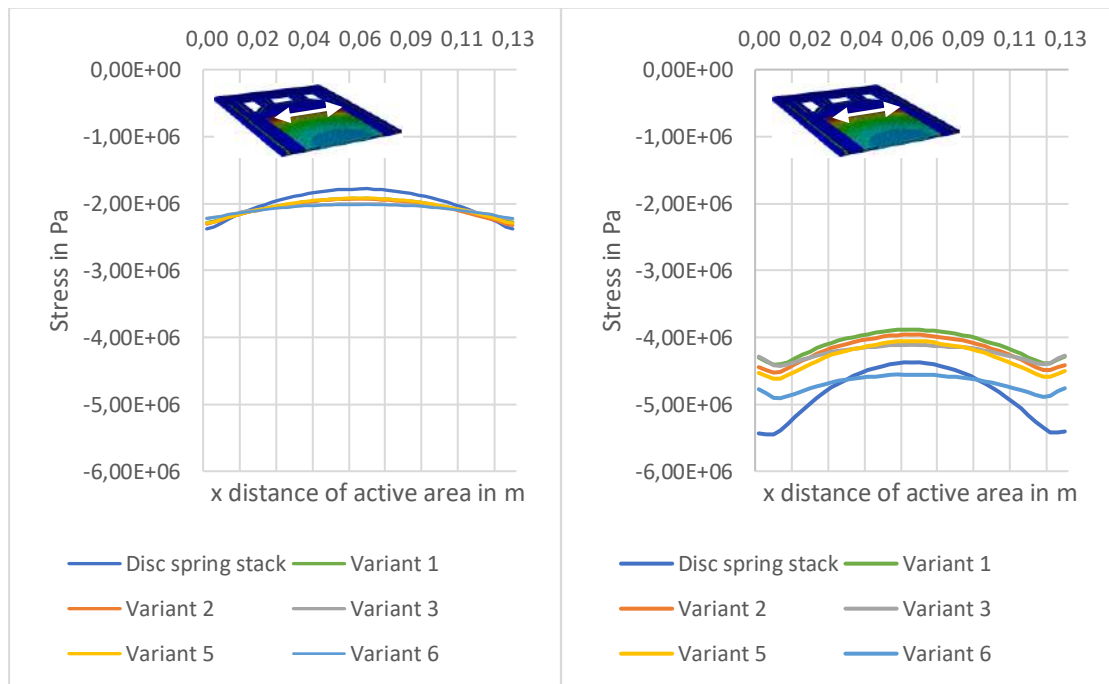
Figure 6.12: Stresses in cross sectional cut on the edge of GDL after assembly (left) and during operation (right)
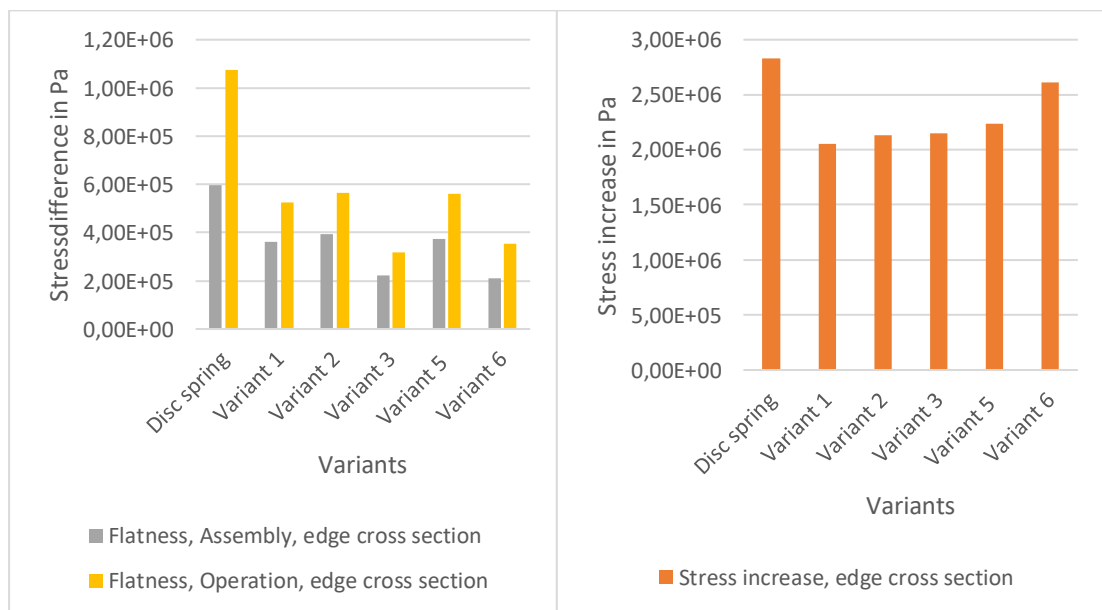
Figure 6.13: Flatness of the stress distribution (left) and stress increase (right) on the edge along the cross-section

To make it clearer the values of the deflection of the end plate after the assembly and during operation are written in Table 6.2. With the higher bending, the edge of the GDL is compressed more leading to the high stress values.

Table 6.2: Deflection of end plate

Deflection in µm	Disc spring	Variant 1	Variant 2	Variant 3	Variant 5	Variant 6
After assembly	84	82	89	88	91	87
During operation	237	207	228	226	230	243

The results on the edge of the longitudinal direction show a very similar result as the middle path on the GDL. This is why the diagrams are not further analysed here but can be seen in Appendix B.

With the flat side of the spring pointing down variant 3 and 6 produce the best results regarding the flatness. With respect to the stress increase from assembly to operation variant 2 shows the best results with exception of the edge in the cross-section, here it is variant 1.

6.1.2   Arc of spring in contact with EP
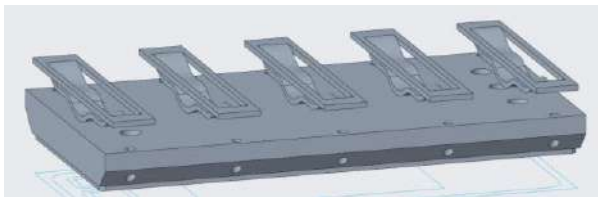
Figure 6.14: Arc of spring showing to the end plate

With the arc of the spring pointing downwards as shown in Figure 6.14 the force flow from the spring to the end plate is changed so that it enters in the middle of each spring. The bending over the width of the end plate is expected to be less. The stress distribution over the GDL is shown in Figure 6.15 exemplary for concept 1. In Figure 6.16 and Figure 6.17 the stress distribution for all the concepts is shown, both in the middle and on the edge of the cross-section.
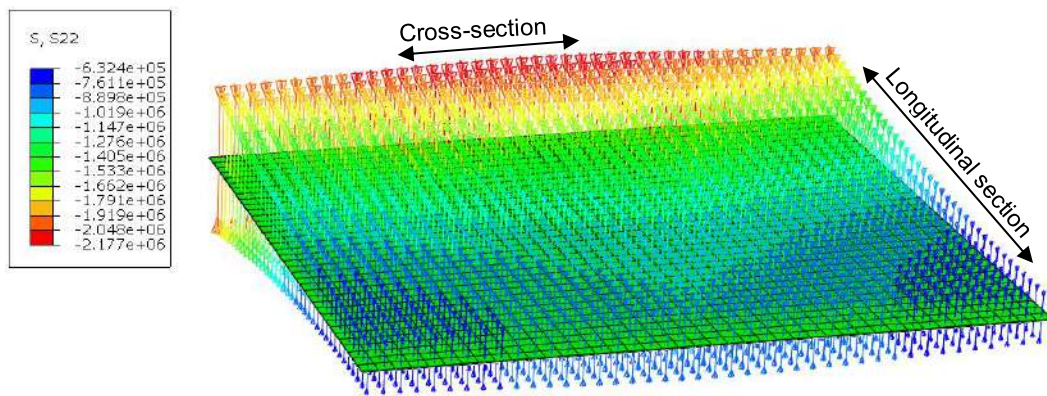
Figure 6.15: Stress distribution of GDL in concept 1 with the arc of the spring in contact with the EP

Compared to before, the highest stress in concept 1, 2 and 5 is now found in the middle of the cross-section. For concept 3 and 6 it is still on the edge. This is due to the number of springs and the force flow entering the first time only in the middle of the end plate and the second time also outside the middle. During the operation (Figure 6.17) the qualitative course of the stress distribution does not change.
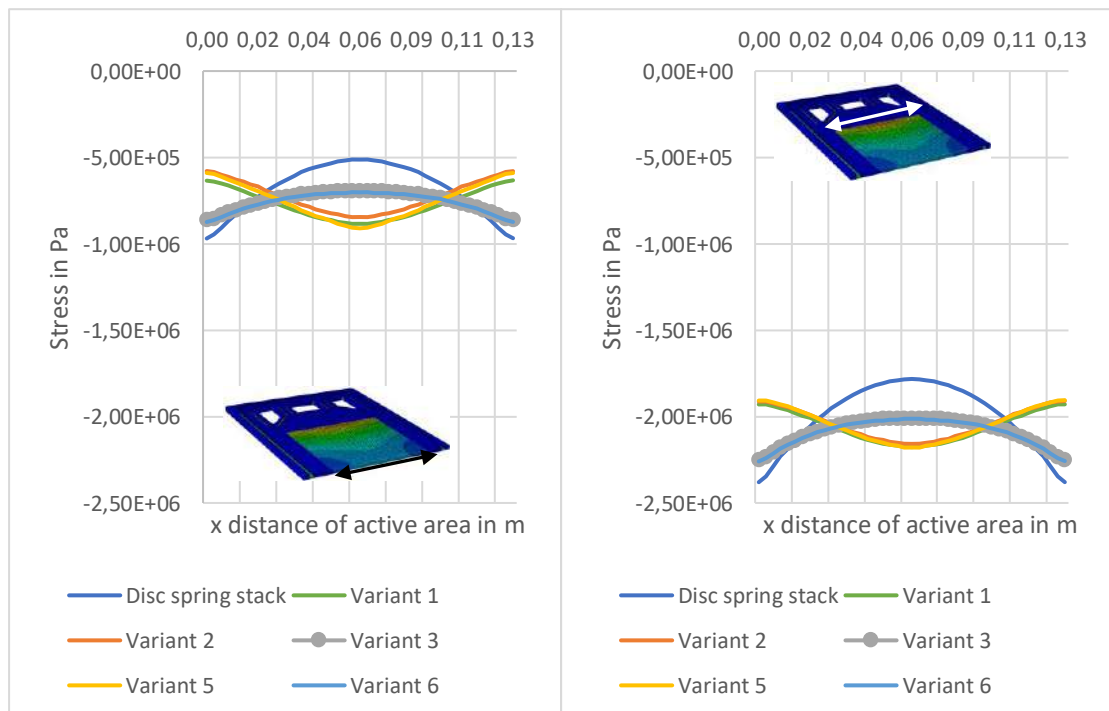
Figure 6.16: Stress distribution with the spring upside down in the middle (left) and on the edge (right) in the cross-section after the assembly
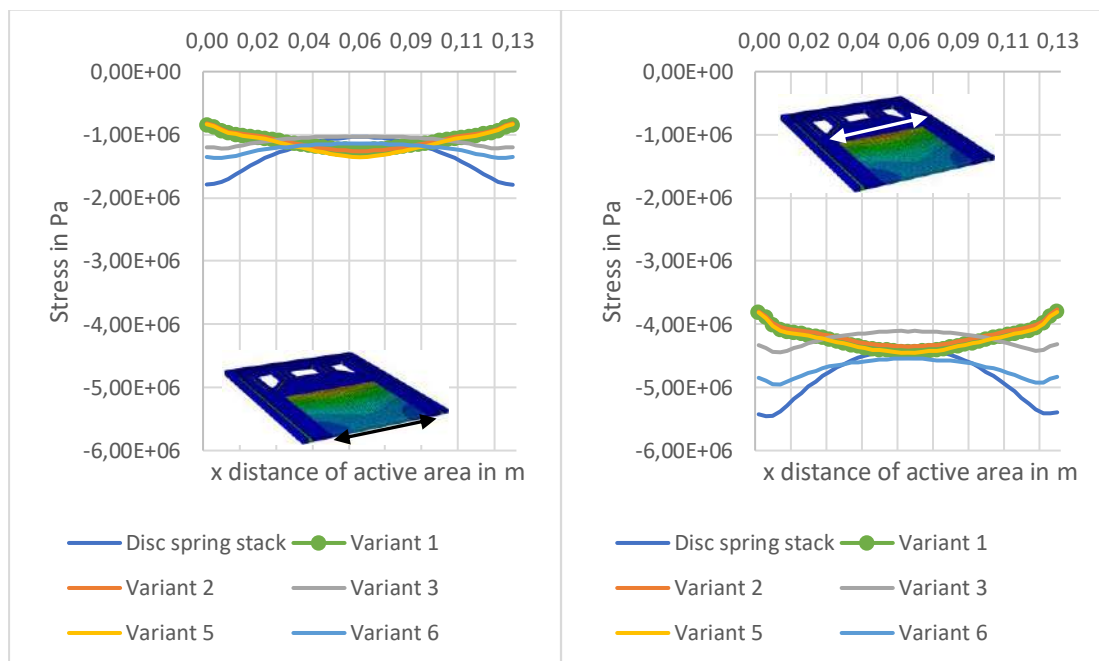
Figure 6.17: Stress distribution with the spring upside down in the middle (left) and on the edge (right) in the cross-section during the operation

The flatness and stress increase are shown in Figure 6.18.
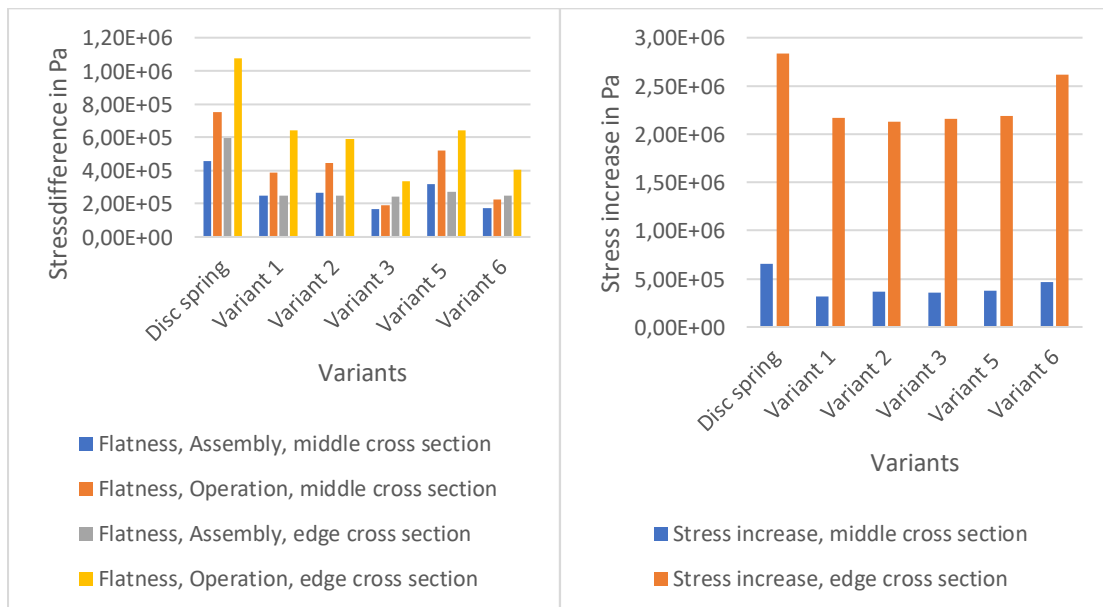
Figure 6.18: Flatness (left), stress increase (right) with spring upside down in cross-section

Still variant 3 and 6 show the best results with about 0.2 MPa difference between the maximum and minimum value reaching up to 0.4 MPa during the operation on the edge

of the cross-section. A comparison of the orientation to the possibility with the flat part to the EP will take part in the discussion part, chapter 6.3.

With respect to the stress increase from assembly to operation variant 1 to 5 are in a similar range again and variant 6 shows worse result due to the higher force increase from the spring characteristic. The stress increase on the edge stays high with 2.1 to 2.6 MPa. This is logical as the bending over the length of the end plate doesn't decrease with the springs turned by 180°. To improve this, different approaches are taken.

As already shown in Figure 6.11 the end plate bulges up with the applied load which is heavily intensified with the stack swelling since only the area of the MEA in the centre of the end plate swells up. The deflection of the end plate is shown in Figure 6.19 with a scale factor of 50 to make it visible.
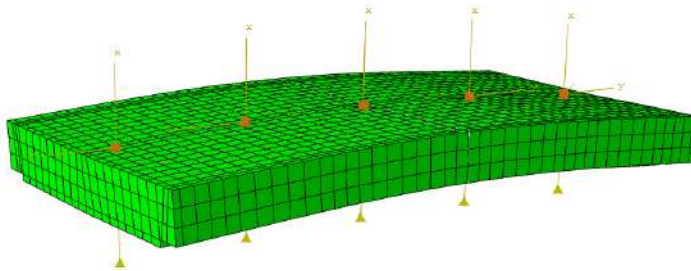
Figure 6.19: Deflection of end plate during operation

The torque produced by the spring forces leading to the deflection increases with a larger lever arm and higher forces. For this reason, a first step to reduce the bending of the end plate and thereby the high stresses on the edge of the GDL is to reduce the lever arms of the forces by moving the springs closer together. The middle one remains in place with the adjacent ones touching it. To maintain the compression force for the gasket around the manifolds the outer springs are kept in their place as illustrated in Figure 6.20. The tests are made exemplary with the springs from concept 2.
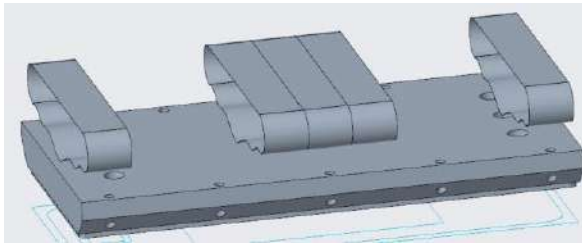
Figure 6.20: New spring position

A second step to reduce the bending of the end plate is to redistribute the force on the springs. Because the MEA is located in the middle, the compression force for the contact between GDL and BPP is changed so that it is exerted only on the three inner springs. The force for the compression of the frame gasket is distributed between all springs whereas the force for the gasket of the manifolds is only applied on the outer springs. This leads to a force of 5 200 N per outer spring and 16 000 N for each inner spring.

The results for the stress distribution in the longitudinal section are shown in Figure 6.21 and Figure 6.22. There is a clear improvement compared to the initial position of the springs in concept 2. By putting the springs closer together but maintaining the force equal for all springs, the stress stays quite constant over the length of the GDL with 1-1.5 MPa. This means the bending of the end plate is reduced so that the extreme stresses on the edge are lower. Also, the difference between the middle (left diagram) and the edge (right diagram) is significantly lower.

A look to the possibility with the force redistributed shows, that the stress increases now towards the centre of the GDL. The end plate doesn't bend outwards any more but receives a small dent in the middle. This is the advantage during the operation, when the membrane swells up. The additional force from the swelling leads to a compensation of the dent from the assembly. This is why the option with the redistributed force shows a very smooth stress distribution in Figure 6.22 with 2-3 MPa over the complete length. The variation with only the springs closer together but the force equally distributed is not as flat but still shows a smoother stress course with a range of 1.4-3.5 MPa than the initial variant 2 (0.8-4.3 MPa). With the force redistributed it is important to mention that the springs are loaded higher than they are originally designed for and the force results are extrapolated from the characteristic curve. An adapted spring design could vary a little bit leading to slightly different results but the qualitative course stays the same.
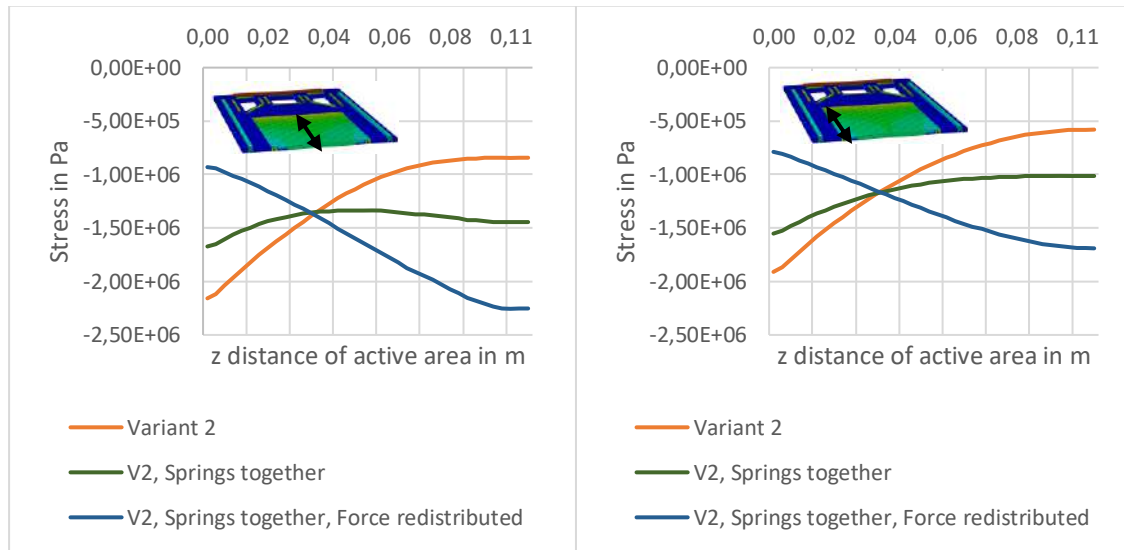
Figure 6.21: Stress distribution of modified concept 2 in the longitudinal section in the middle (left) and on the edge (right) of the GDL after assembly
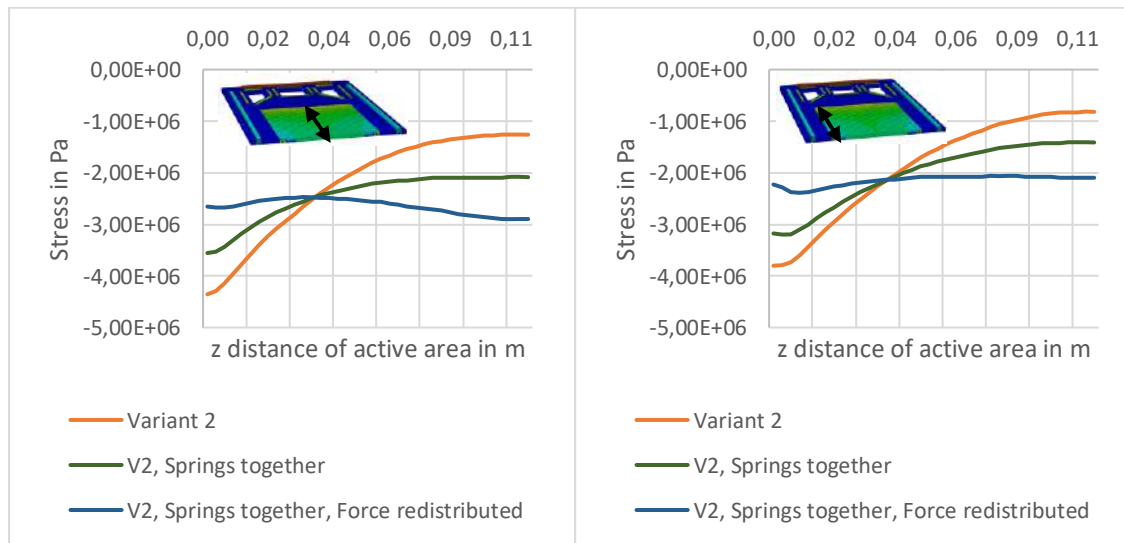
Figure 6.22: Stress distribution of modified concept 2 in the longitudinal section in the middle (left) and on the edge (right) of the GDL during operation

The significant improvement becomes clearer in Figure 6.23 where it is visible that the stress difference both after assembly and during operation is changed from 1.3 MPa to 0.3-0.5 MPa and from 3 to 1.5-1.8 MPa. The average stress increase (Figure 6.23 on the right) stays the same with around 1 MPa because it depends mainly on the spring characteristic and not on the spring position.
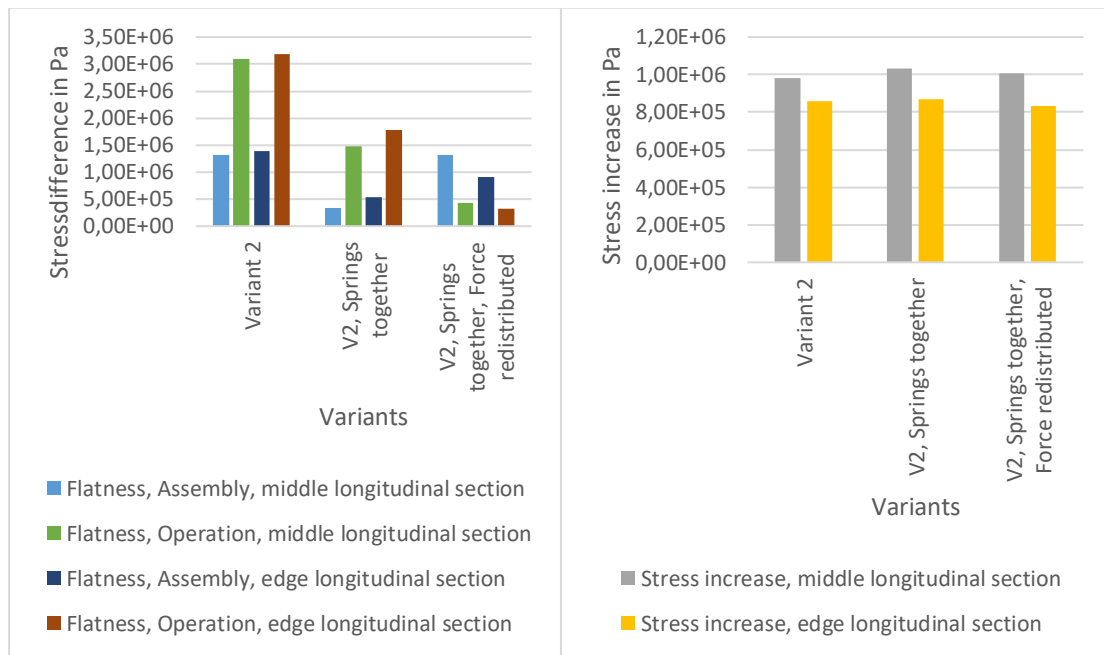
Figure 6.23: Flatness (left) and stress increase (right) with changed spring position in the middle and on the edge of the longitudinal section

The repositioning of the springs leads to a slightly worse stress distribution in the cross-section because the force is concentrated more in the middle. The effect is, however, negligible in comparison to the improvement along the longitudinal section. Detailed diagrams can be found in Appendix B.

When the arc of the spring shows towards the end plate still variant 3 and 6 deliver the best results in terms of flatness. The expectations for an improved flatness in comparison to the spring with the flat side down were higher. Only variant 1 and 2 show slightly better results after the assembly. The force concentration in the middle is so high that the extreme values, that were on the edge of the GDL, are now found in the middle resulting in a very similar flatness only inverted. The reduction of the end plate bending through the change of the spring position produces significant results.

6.1.3   Parameter variation

At last, some parameters of the initial model are changed to see if or what kind of an influence they have on the results of the compression of the GDL. The aspects are chosen with regard to modelling issues and actual changes in the fuel cell stack. There are two changes regarding the modelling issues, the first is the change of the properties of

the MEA. Instead of assigning the membrane and the GDL their individual properties, a common Young's modulus and Poisson ratio are assigned, which could simplify the simulation. The second change concerns the GDL properties. In the original model linear elastic properties are assigned, these are changed now to a non-linear stress-strain curve to better represent the material behaviour. There are as well two changes regarding the actual fuel cell stack properties. The first is the material of the BPP, it is changed from steel to graphite because this is a common material for bipolar plates as well. The other change is the gasket material which is changed from EPDM to Silicon Rubber (SR) because Qiu et al. recommend the usage of SR [59]. The new properties are shown in Table 6.3.

Table 6.3: Properties of changed parameters

	MEA	GDL	BPP	SR
Young's modulus in MPa	21 [60]	See stress-strain curve in Figure 6.24 (right)	10 000 [61]	See stress-strain curve in Figure 6.24 (left)
Poisson ratio	0.01 [60]		0.25 [61]	
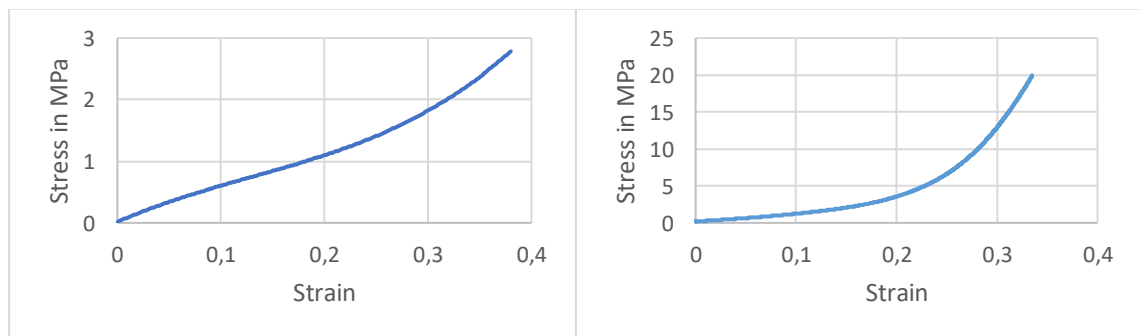
Figure 6.24: Stress strain curve of SR (left), (adapted from [59]) and for non-linear GDL properties (right) [62]

The stress distribution in the middle and on the edge of the cross-section of the GDL with the parameter variations is shown in Figure 6.25. The initial model properties with the flat side of the spring to the end plate are shown in the graph of variant 2 to have a reference. First thing to mention is, that the qualitative course of the graphs doesn't change. The highest stress is on the edge and the lowest stress in the middle. With the change in gasket material, the gasket compression force also changes; the calculation can be found in Appendix C. The silicone rubber shows at the same strain a higher stress than EPDM. This leads to a higher return force against the stack compression thus

leading to less bending of the end plate with a deflection of 206 µm during operation compared to 228 µm with the EPDM material. This is why the stresses on the edge of the GDL are slightly lower, and in the middle slightly higher than in the initial variant.

The changed MEA material has a higher Young's modulus than carbon paper but a lower than Nafion®. Also, the Poisson ratio is a lot lower. This leads to a very high stress on the edge as visible on the right. Because the applied force in comparison to the initial variant didn't change, the compression of the GDL is less in the middle leading to a lower stress level. These results differ significantly from the initial material definition. Because in this project the relevant results are taken directly from the GDL, it is not advisable to define one average property to membrane and GDL. In other cases, this might be valid.

The change of the bipolar plate material leads to the smallest differences. This is because it is a rather stiff part. Since graphite has a lower Young's modulus than steel it is compressed more and the GDL slightly less leading to a little lower stresses.
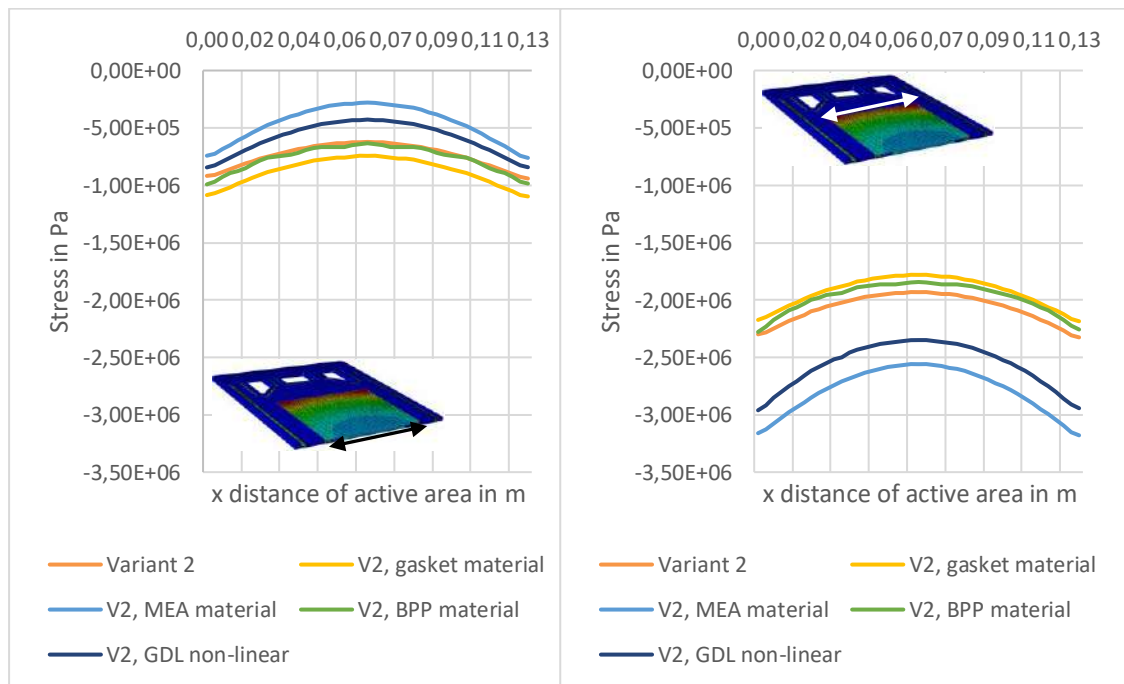
Figure 6.25: Stress distribution in the middle (left) and on the edge (right) of the cross-section of the GDL with changed parameters after the assembly

The last variation is the definition of the GDL. In the initial model it has an elastic definition, now a complete stress-strain curve is assigned (see Figure 6.24 on the right). In the middle of the GDL the stress is lower and on the edge it is higher than in the original

definition. This is because the course of the curve is progressive, with smaller stresses at small strains and higher stresses at high strains than in the elastic definition. The definition of the GDL as non-linear material gives results closer to reality but to investigate the spring behaviour the elastic definition gives a sufficient overview.

The stresses during the operation show the same course than after the assembly only with higher absolute values according to the spring characteristic. This is why the graph is not discussed further but can be seen in Appendix B.

6.2   Experimental results

Two spring concepts are produced by the industrial partner to carry out experiments. These are chosen according to the simulation results. The best flatness along the cross-section is achieved through both variants with 15 small springs whereby concept 3, the design with the welded spring belt shows a better result in terms of stress increase. This is why concept 3 is the first option to be produced. In comparison to all variants, concept 1 and 2 show the best results regarding the stress increase. As the springs in concept 2 can be moved, for example to reduce the end plate bending along its length, whereas concept 1 is fixed, because the spring has the same size as the end plate, concept 2 is the second production option. Due to the manufacturing time, only concept 3 could be tested during the period of this work. This is why only these results are shown and discussed. In Figure 6.26 the springs of concept 3 are shown.

Figure 6.26: Springs of concept 3

The experiments are carried out as described in chapter 5.2. As result the pressure distribution over the active area is shown with the image of the pressure-sensitive film and the digital pressure sensor.

First, the desired pressure distribution is created, shown in Figure 6.27, which is achieved through the compression of the setup without any springs so that the flat plates are pushed down directly by the stamp. The result is a very even distribution over the active area and the gaskets. Both in the cross-section and the longitudinal section the pressure is quite even. The bright spot in the middle comes from tape residue that was pressed into the GDL, also visible in the digital results. The upper side of the active area shows higher pressure because the stamp didn't compress the plates perfectly central. Both scales are given in MPa.
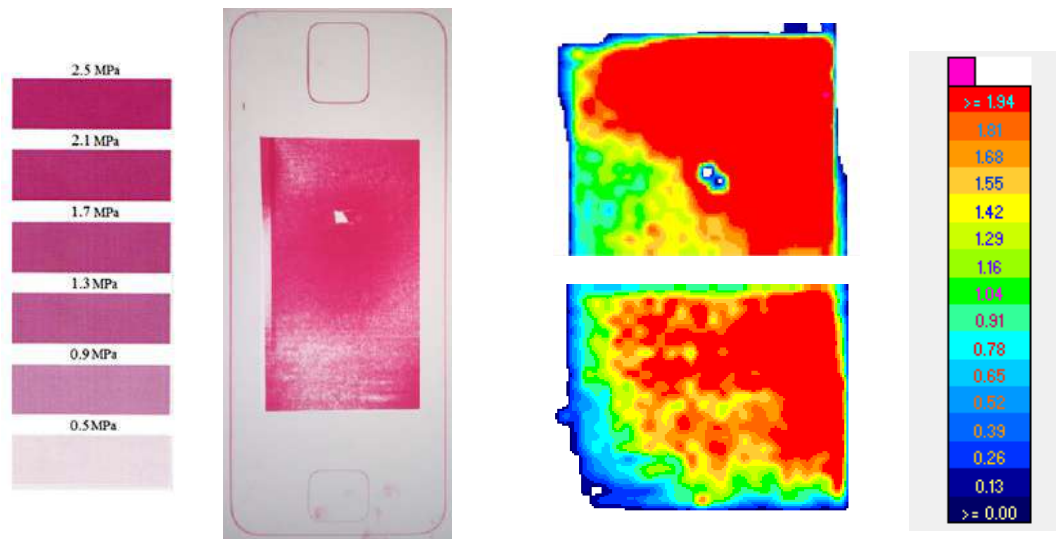
Figure 6.27: Desired pressure distribution (MPa), compression without springs

As first setup in relation to the simulation, the results with the washers on the end plate to represent the disc spring case are presented in Figure 6.28. Here only results with the digital sensor were taken. The black arrows in the following images show the path where the stress distribution was taken from to compare all tests in Figure 6.32. It is always in the cross-section of the GDL on the right hand side.
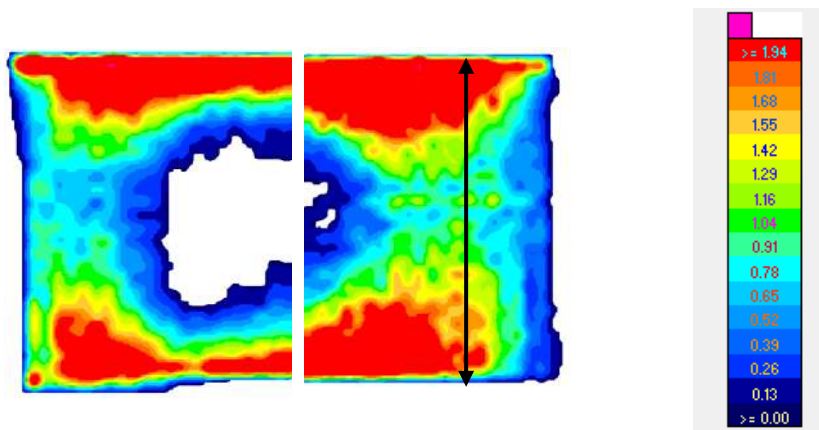
Figure 6.28: Pressure distribution (MPa) that represents the disc spring case

It is visible, that on the top and bottom edges of the GDL is a very high pressure whereas the pressure in the centre is a lot lower. The applied force is about 35 kN, the results are as expected.

In Figure 6.29 the pressure distribution of spring concept 3 with the flat sides of the spring pointing downwards is shown.
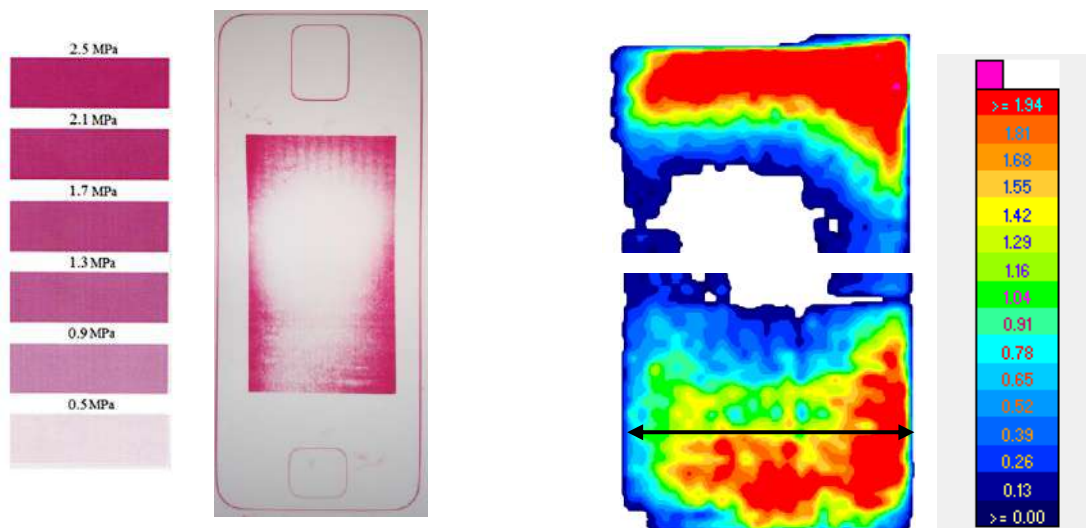
Figure 6.29: Pressure distribution concept 3 (MPa), flat side of spring in contact with EP

On the fuji film the contour of the gaskets is visible with a very even distribution. In the active area the pressure on the edges is higher than in the centre, this can also be seen in the digital results. The distribution is not perfectly symmetric, this is because the stamp

of the press didn't attack exactly in the middle of the end plate. The applied force is between 30 kN (right) and 50 kN (left).

As next possibility, the springs are implemented with the arc of the spring touching the end plate. The results for variant 3 are shown in Figure 6.30.
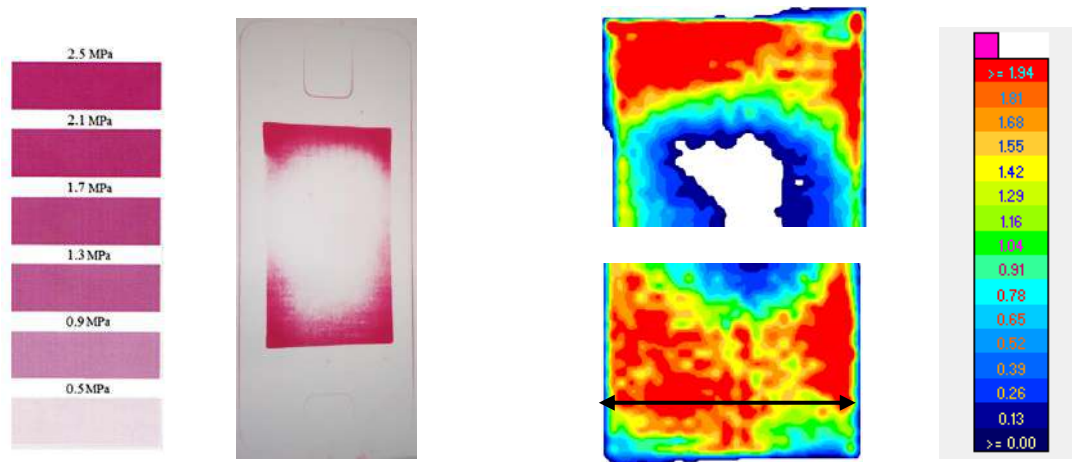
Figure 6.30: Pressure distribution concept 3 (MPa), arc of spring in contact with EP

The results of the pressure distribution in the fuji film are similar as in the first experiment with the flat part of the spring downwards. The pressure on the edge of the GDL is higher than in the centre. The digital results show the same distribution as the fuji paper. The applied force is approximately 35 kN.

The last test is made with the inner spring rows touching each other to improve the stress distribution along the longitudinal section. These results are given in Figure 6.31.
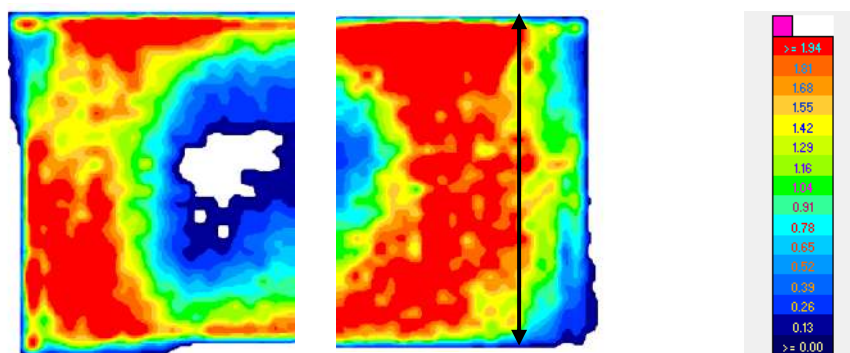
Figure 6.31: Pressure distribution concept 3 (MPa), springs put together, arc of spring in contact with EP

The pressure distribution is similar as before, on the edges is a higher pressure, in the centre it is lower. The difference to the initial spring position is not very distinctive but the area in the middle where no value is recorded is smaller, meaning that the pressure is better distributed. The total force is about 40 kN.

In Figure 6.32 the stress distribution of the experimental results is shown along the path that was indicated in each image above. It is clearly visible that the distribution of the disc spring case shows high stresses on the edge and very low stresses in the middle whereas the distribution of the spring variants is more even. Between the possibilities of positioning the springs it is difficult to describe differences because of the coarse measurement resolution. The improvement from the disc spring case to the new spring concept is well visible.
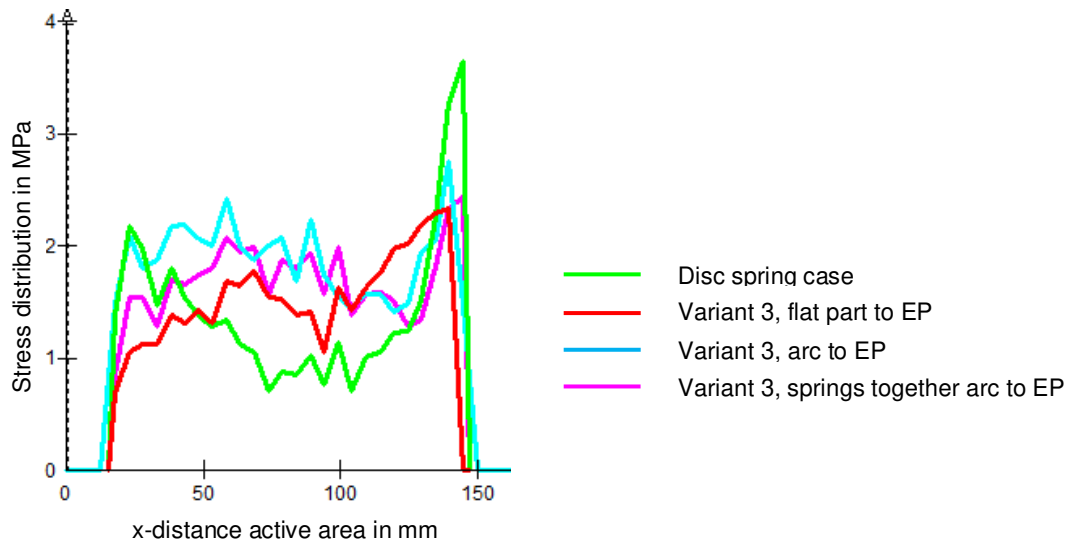
Figure 6.32: Comparison of experimental results

6.3   Discussion

In the discussion part first, the different spring positions and second, the simulative and experimental results are compared to each other. Based on the results a recommendation for the choice of a concept can be given. From Figure 6.33 to Figure 6.35 the simulative results of the different possibilities of positioning the springs are shown with the exemplary results of concept 2. It is visible that both in the flatness and the stress

increase the novel spring concept delivers better results than the reference with the disc spring stack. Between the possibility of positioning the spring with the flat part or the arc towards the end plate there is no big difference. In the cross-section after the assembly the option with the arc showing down shows up to 0.15 MPa better results because the end plate bends less but with the force increasing during operation the results are about 0.07 MPa worse. This is also valid for the other concepts with the big springs (concept 1 and 5). For the concepts with the small springs (concept 3 and 6, not shown in the graphs in this section), changing the spring orientation doesn't make a difference. The expectations for the differences were higher. A reason that the stress distribution doesn't change is, that first the force attacks on the edge of the end plate, and in the second option it is very punctual in the middle, leading to the reversed distribution. As the results of concept 3 and 6 show, an even distribution of force application leads to a more uniform stress distribution.

A look to the stress distribution in the longitudinal section in Figure 6.34 shows that there is no change at all with the varied spring orientation. This comes from the bending of the end plate, induced by the assembly belt position which stays the same in both the options with the flat part and the arc to the EP. This is highly improved with the repositioning of the springs as visible on the very right in Figure 6.34. The stress difference is now in the range of 0.5 MPa after assembly and 1.8 MPa during operation which is a third and a half, respectively, of the value before.
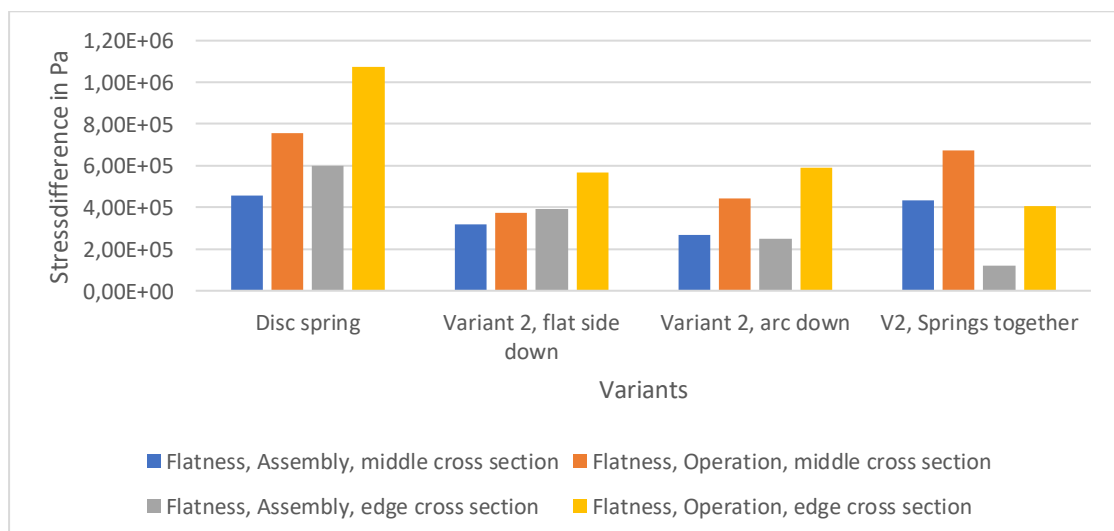
Figure 6.33: Comparison of flatness in cross-section
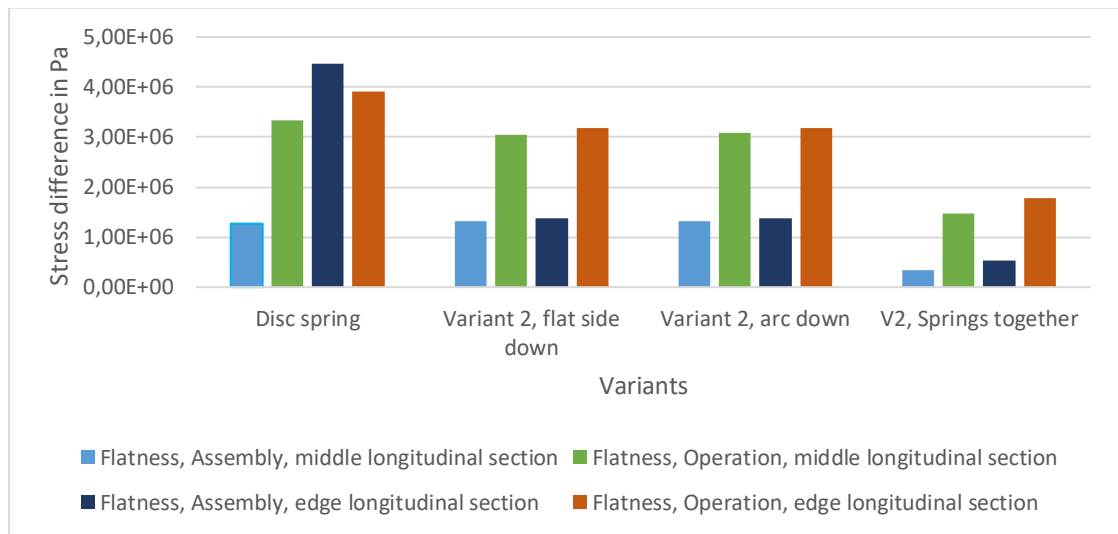
Figure 6.34: Comparison of flatness in longitudinal section

The stress increase (Figure 6.35) doesn't change much with the orientation and position change. It increases by 0.2 MPa in the middle and decreases by 0.25 MPa on the edge when the springs are put together because the deviation from the average value is less. The main trend is, that the increase stays the same because it depends on the spring characteristic.
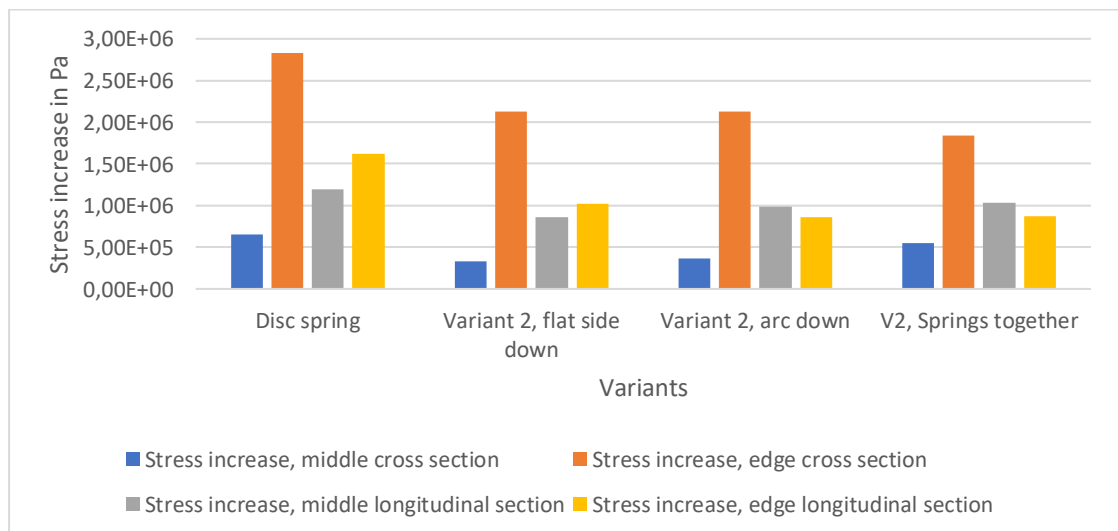
Figure 6.35: Comparison of stress increase from assembly to operation

With the results of all the simulations two statements can be derived. First, the main influence on the stress distribution has the bending of the end plate which is defined by

the force magnitude and the position of the springs that make up the lever arm. Second, the stress increase is defined through the spring characteristic.

Regarding the stress distribution, the concepts 3 and 6 deliver the best results over the width of the stack because they exert the smallest torque. One point to improve this even more could be to put the springs also over the width closer together, which could be investigated in a further simulation.

The end plate bending over the length is very similar for all concepts regardless of the spring orientation. This is because the position of the tie rod or assembly belt is maintained and these define the lever arms over the length. As seen, the stress distribution improves significantly by bringing the springs closer together and thereby minimising the torque. A further improvement can be achieved by optimising the end plate design. The stiffer the end plate the less the bending and thereby the better the stress distribution. This is also discussed in the literature where stiff EP designs with low weight are elaborated [63].

The reduction of the end plate bending is indispensable because with the high stresses on the edges of 4-5 MPa the GDL experiences a too high compression leading to a plastic deformation and permanently deformed gas channels with reduced porosity. This worsens the performance because the concentration losses increase.

The results of the stress increase from assembly to operation are not as satisfactory as those of the stress distribution. Particularly at the edges the value is too high with a 2-2.5 MPa rise. This value depends mainly on the characteristic curve and indirectly partly also on the end plate bending. With a smaller force difference between the assembly force and operation force a smaller stress increase would come along. This requires a revised spring design with a more degressive curve so that the force doesn't change much when the stack swells. The main improvement will be achieved by reducing the maximum force of the spring at the maximum compression point while maintaining the point of assembly. This should be investigated before a production start in industrial scales.

The experimental validation of the springs from concept 3 shows a good accordance between the simulated results and the measured data. This is shown in Figure 6.36. Due to the experiment setup only a qualitative and no quantitative comparison is possible. Imitating the disc spring stack, where the force attacks only on the edge of the EP, very high stress is achieved on the edge of the active area. As visible in Figure 6.36 on the

top the highest stress in the simulation is along the width of the GDL whereas the experiment shows along the length the highest stress. The difference comes through the stamp which applies force only in the centre instead of a force on every single tie rod. However, the uneven distribution becomes clear.

With the springs this is improved, see the bottom image of Figure 6.36. The high contact pressure is spread over a bigger area, but the distribution is not completely uniform yet. This is also a confirmation of the simulative results.
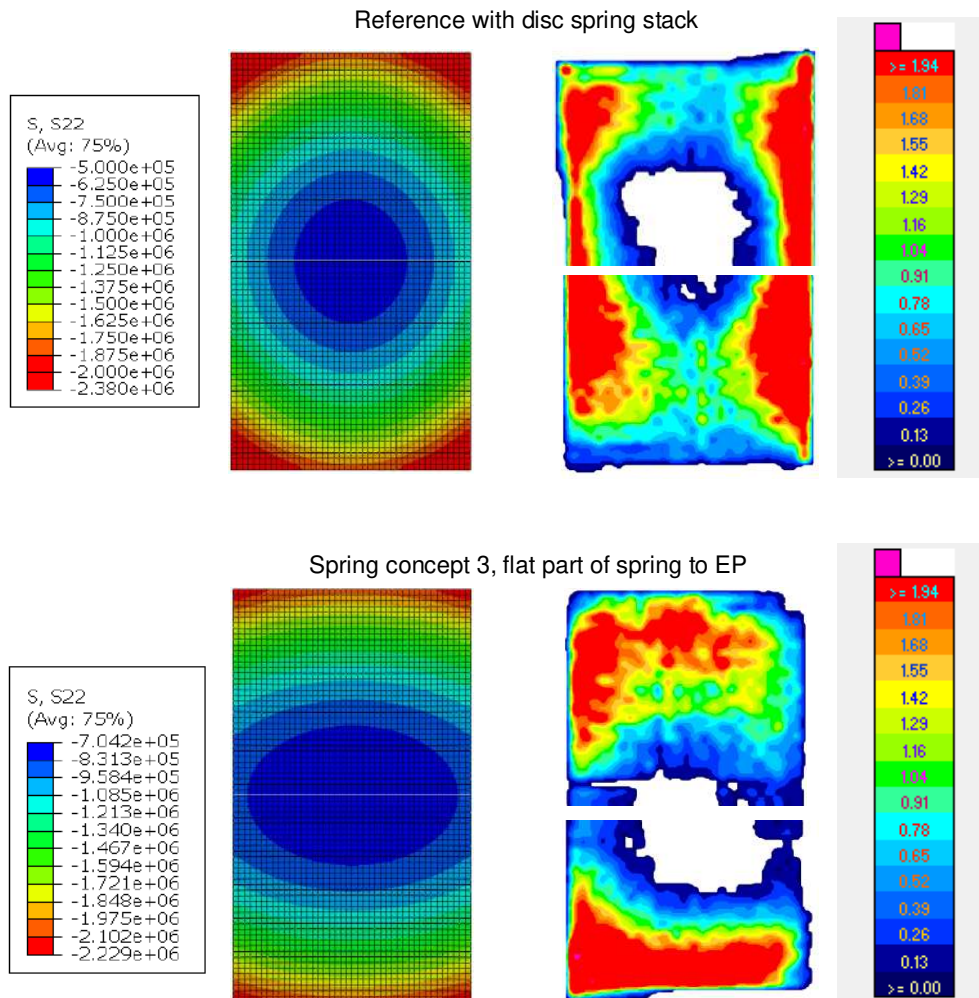
Figure 6.36: Comparison of simulative (left, scale in Pa) and experimental results (right, scale in MPa)

The repositioning of the springs by putting them closer together did show improvement although this was expected to be more significant. Especially the difference in the contact pressure along the longitudinal section was not so distinct in the experiment as in the

simulation. One reason is the already mentioned force flow difference through the stamp versus the individual force attack on each spring in the simulation.

Since the results of the proposed concepts are in all cases better than the results with the use of the disc spring stack, it is recommendable to use the novel spring concept. The best result of the proposed concepts regarding the stress increase shows the second variant (5 big springs with the welded spring belt design). It has a maximum stress rise of 2.13 MPa which is reduced by about 0.3 MPa with the measures taken to reduce the end plate bending. Important factors are that the springs are movable to be able to change the position of the application of load and the improved spring characteristic. However, the stress increase between variant 2 and 3 is almost identical, as emphasized in Figure 6.37, whereas the stress distribution is better by a factor of 2 for variant 3. Therefore, variant 3 gives the best overall results and is the best option.
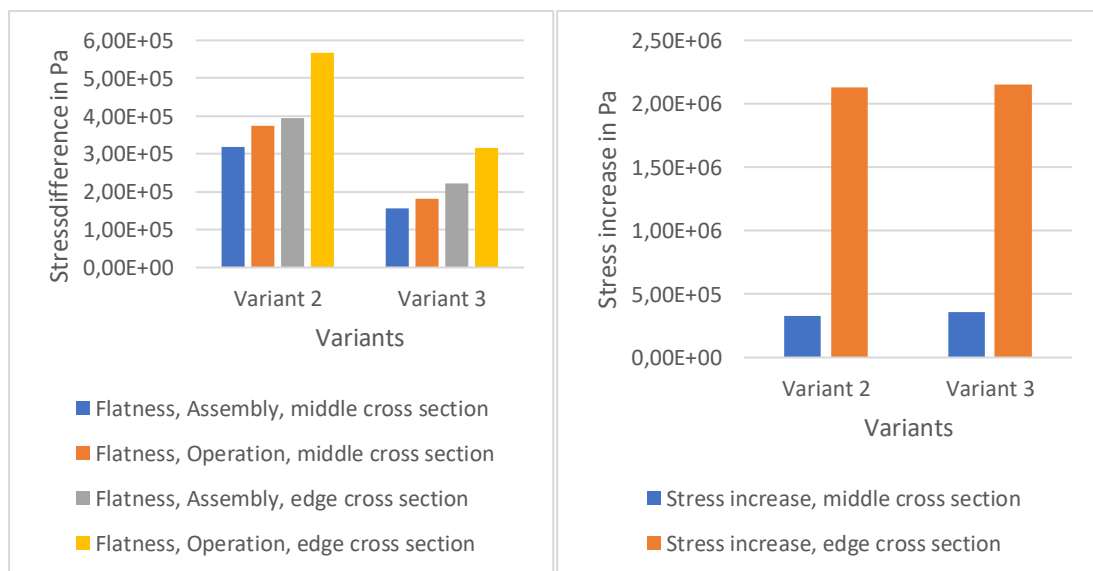
Figure 6.37: Comparison of variant 2 and 3

In case that the active area differs from that of the simulated model, the best stress distribution is still achieved through the minimization of the end plate bending whereby the tightness of the stack should not be neglected but must be guaranteed at all times.

The stress results of simulation and experiment are only measured in one single fuel cell to minimise the modelling effort while a dummy part represents the rest of the stack. The results can still be transferred to all cells of a complete stack because since all cells are stacked on top of each other they are connected in series which means that the

qualitative stress distribution stays the same through the stack. As Bates et al. discovered, the absolute stress values in the GDL vary through the stack with higher stresses in the middle of the stack [64]. This can influence the absolute value of the assembly force to find a good compromise between cells in the middle and near the end plate but cannot be influenced through the spring concept.

With the new concepts from this thesis, the relation between benefits and system complexity is well balanced. There are other solutions from patents that have not been compared in this work. The stress increase over the active area is probably minimised with the solution with the hydraulic pressure pocket because the pressure of the fluid can be adjusted in real-time. A comparison between the new concepts from this thesis and the patented solutions can be made in further projects.

7 Summary and outlook

The task of this master thesis is to propose, simulate and validate new spring concepts for a PEM fuel cell stack. A spring concept is necessary to distribute the assembly forces evenly over the active area of the fuel cell and to absorb the swelling of the stack that occurs during operation. This maintains a constant reaction rate and sustains the stack performance. The swelling happens due to the properties of the membrane. They swell up with increasing temperature and humidity by an amount of up to 14 % according to the data sheet. Since humidity and an increased temperature are unavoidable effects during the operation, it is obligatory to address this challenge. The key part of this problem is the gas diffusion layer, which needs a high contact pressure to minimise ohmic losses while maintaining its porous structure to reduce concentration losses. Both ohmic and concentration losses are influenced by the assembly force but in contrary directions. This is why a compromise regarding the assembly force and its distribution needs to be found which can be achieved through a spring concept.

In current fuel cell stacks, either a patented spring solution is used, or disc springs are stacked on tie rods through which the assembly force is applied. In collaboration with an industrial spring manufacturer, new concepts are elaborated. There are two designs: one with a welded spring belt and a second which can be described as spring with bridge structure. In total eight variations are proposed differing in size and design from which five are found to be feasible and are then investigated in a simulation. The first concept is a single spring as big as the end plate of the fuel cell stack. The second consists of five springs along the length of the end plate covering the whole width of the end plate. The third is similar to the second but with three springs per row so that it contains a total number of 15 springs. These three concepts all use the design with the welded spring belt. There are two more proposals using the spring with bridge structure. They are equivalent to the second and third concept with five and 15 springs respectively.

The proposed spring concepts and the disc spring stack are implemented in a three-dimensional finite element model with the fuel cell stack containing the end plates, one single cell and a dummy part which represents the rest of the stack to reduce the calculation time. The springs are defined by two points with a connection according to the properties of the spring characteristic. The applied assembly force of about 60 000 N compresses the gasket and induces the contact pressure between the parts.

The five novel spring concepts can be implemented in two ways. Either the flat part of the spring touches the end plate or it is turned by 180° so that the arc of the spring is in contact with the end plate. An analysis of the force flow through the springs shows that with the flat side of the spring down, only the outer 10 % of the contact length transmits a force to the end plate for the design with the welded spring band. With respect to the spring design with bridge structure about 30 % of the contact length transmits the force. When the arc of the spring is in contact with the end plate an approximation of the contact length on the end plate of about 20 % of the radius of the arc is acceptable.

The simulation is built up in several steps with the gasket compression and the application of the assembly force. At last the swelling is applied. In total, there are four points of interest for closer analysis. These are in the middle and on the edge of the GDL both in the cross-section and the longitudinal section. With the flat side of the spring down, for all concepts the highest stress in the GDL is on the edges and the lowest in the centre. The disc spring concept as reference increases from 0.5 MPa in the middle and 2.4 MPa on the edge after the assembly to 1.0 MPa in the middle and an extreme value of 5.4 MPa on the edge during the operation. The new proposed concepts all have a better stress distribution with the minimum and maximum stress not so far apart. Both concepts with the 15 small springs show the most uniform distribution with a difference between minimum and maximum stress of only 0.3 MPa in the cross-section because the force flow is distributed better over the end plate. The other concepts reach up to 0.6 MPa difference which is still a good result. Looking at the longitudinal section, there is almost no difference between the concepts. During the operation, the stress differences along one path go up to 3 MPa which is very high. The reason for this lies in the bending of the end plate. Since only the active area swells up, the deflection of the end plate increases from assembly to operation. This effect is particularly strong in the longitudinal section leading to a high compression on the edges of the GDL.

Not only the stress distribution but also the stress increase from assembly to operation is better in the new concepts than with the disc spring stack. The variants are very similar to each other with exception of variant 6, the 15 small springs with the bridge structure. This concept shows worse results because the force difference between assembly and operation point is higher than in the other concepts.

When the springs are rotated so that the arc of the spring is in contact with the end plate, the stress curve in the cross-section depends on the concept. For variant 1, 2 and 5, the concepts with one or five large springs, the stress curve is flipped so that the maximum

stress is now in the middle and the smallest stress on the edge. For variant 3 and 6, the concepts with the 15 small springs, the course of the curve stays the same as before with maximum stress on the edge and minimum stress in the middle because the force flow still enters at various points along the end plate width and not only directly in the middle. The flatness doesn't change significantly. The best values are still achieved through the concepts with the 15 small springs. With respect to the stress increase it stays the same as before because the spring characteristics are also the same.

To improve the extreme stress values on the edge of the GDL, the bending of the end plate needs to be reduced. A good result is achieved by changing the position of the springs. With the three inner springs touching each other, the bending is reduced to such an extent that instead of a difference of 1.4 MPa after the assembly and 3.2 MPa during the operation now only 0.5 MPa and 1.8 MPa respectively are present. A further improvement during operation can be achieved if the force is no longer equally distributed over the springs, but is concentrated more in the active area. As a counterpoint, this may require change in the spring design due to higher loads.

The best results regarding the two factors stress distribution and stress increase shows variant 3 with the 15 small springs in the welded spring belt design. The equivalent variant 6 with the spring with bridge structure is not suitable because of the high stress increase from assembly to operation. Variant 1, 2 and 5 all show a similar stress increase, but the first two show a better stress distribution. Because variant 1 is the spring in the size of the end plate and is therefore quite inflexible, variant 2 gives more possibilities, for example changing the spring position to reduce end plate bending. This is why variant 2 and 3 are selected for production and experimental validation.

Due to the production time only variant 3 could be tested during the duration of the thesis. The experimental results show a qualitative confirmation of the simulated results. The springs give an improvement in comparison to the disc spring stack but the pressure distribution over the active area is not completely uniform. The behaviour regarding the stress increase could not be tested because the force of the test bench could not be adjusted fine enough. But, since the tested spring shows a very linear behaviour, the results can be transferred to the complete working range.

The springs of concept 2, which have not yet been tested, can be tested with the same setup used for concept 3. The force will be applied through the spring plate. As the expected difference to concept 3 is small regarding the pressure distribution, the force

application must be optimised. This is because it is difficult to set the force value precisely without electronic control.

In conclusion, the proposed spring concepts all show a better result than the reference with the disc spring stack with respect to the stress distribution over the active area and regarding the stress increase from assembly to operation. A statement in relation to other spring solutions found in patents cannot be made since no detailed data is available. The interaction between spring concept and end plate design has become more important as the bending of the end plate determines the compression of the GDL around the edges. The stiffer the end plate and the more distributed the force flow, the more uniform the contact pressure.

Further improvement can be made through an adapted end plate design both regarding weight saving and higher stiffness. Regarding the stress increase, the spring characteristic delivers the key point. The smaller the difference between the point of the assembly force and the force during operation the smaller the stress increase in the GDL. This could be improved through another change of the spring design. Regarding the relation between benefit and system complexity, the novel spring concepts are a simple possibility to improve the stress distribution and to handle the changes due to operation conditions.

Appendix A

Table Appendix A.1: Spring characteristic variant 1

Deflection (mm)	Force (N)
0	0
0.09825	3149.1
0.1965	6291.1
0.29475	9425.7
0.393	12553
0.49125	15673
0.5895	18785
0.68775	21890
0.786	24987
0.88425	28076
0.9825	31157
1.0807	34230
1.179	37296
1.2773	40353
1.3755	43402
1.4737	46442
1.572	49474
1.6703	52498
1.7685	55513
1.8498	58000
1.8668	58519
1.965	61517
2.013	62978
2.061	64437
2.125	66379
2.189	68318
2.253	70253
2.317	72183
2.381	74110
2.445	76034
2.509	77953
2.573	79868
2.637	81779
2.701	83687

2.765	85590
2.8098	86920
2.829	87489
2.893	89385
2.925	90331

Table Appendix A.2: Spring characteristic variant 2

Deflection (mm)	Force (N)
0	0
0.105	325.12
0.21	912.18
0.315	1526
0.42	2150.6
0.525	2780.9
0.63	3414.7
0.735	4050.6
0.84	4688
0.945	5326.8
1.05	5966.1
1.155	6605.6
1.26	7243.9
1.365	7881.1
1.47	8517.8
1.575	9153.8
1.68	9789.2
1.785	10423
1.89	11056
1.98	11600
1.995	11687
2.1	12317
2.148	12606
2.196	12892
2.26	13274
2.324	13655
2.388	14036
2.452	14417
2.516	14796
2.58	15175
2.644	15554

2.708	15932
2.772	16309
2.836	16685
2.9	17061
2.94	17298
2.964	17436
3.028	17811
3.06	17998

Table Appendix A.3: Spring characteristic variant 3

Deflection (mm)	Force (N)
0	0
0.084	170.73
0.168	380.69
0.252	600.31
0.336	820.75
0.42	1040.9
0.504	1260.5
0.588	1479.4
0.672	1697.3
0.756	1914.1
0.84	2129.4
0.924	2342.4
1.008	2550.7
1.092	2756.1
1.176	2958.9
1.26	3158.8
1.344	3356
1.428	3550.2
1.512	3741.5
1.568	3866.67
1.596	3929.9
1.68	4115.3
1.728	4219.8
1.776	4323.4
1.84	4460
1.904	4594.7
1.968	4727.7
2.032	4858.8

2.096	4988.1
2.16	5115.6
2.224	5241.3
2.288	5365.1
2.352	5487
2.416	5607.1
2.48	5725.3
2.528	5812.2
2.544	5841.7
2.608	5956.2
2.64	6012.8

Table Appendix A.4: Spring characteristic variant 5

Deflection (mm)	Force (N)
0	0
0.143	1447.3
0.286	2850.9
0.429	4200.2
0.572	5500.7
0.715	6753.6
0.858	7960.4
1.001	9122.4
1.144	10241
1.287	11317
1.326	11600
1.43	12352
1.526	13025
1.622	13680
1.718	14318
1.814	14939
1.91	15539
2.006	16116
2.102	16674
2.198	17213
2.286	17676
2.294	17718
2.39	18172

Table Appendix A.5: Spring characteristic variant 6

Deflection (mm)	Force (N)
0	0
0.043	504.33
0.086	987.75
0.129	1449.9
0.172	1890.9
0.215	2311.3
0.258	2712
0.301	3093.8
0.344	3457.4
0.387	3803.7
0.395	3866.67
0.43	4133.4
0.526	4812.6
0.622	5416.2
0.718	5873.5
0.814	6161.2
0.91	6356
1.006	6439.8
1.102	6459.1
1.198	6442.2
1.294	6391.9
1.355	6341.5
1.39	6313

Appendix B

Spring with flat part down:
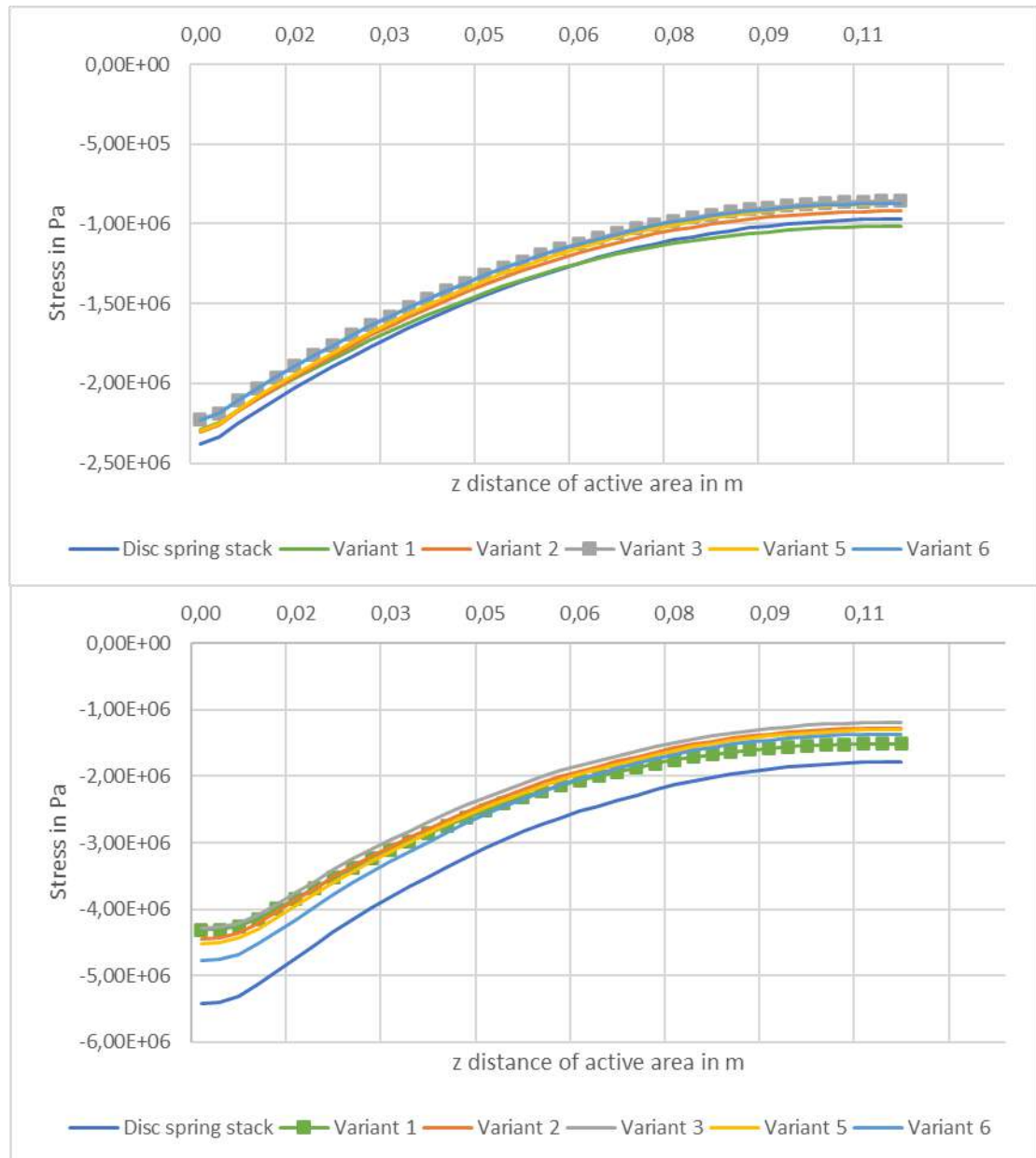
Figure B.1: Stresses in longitudinal sectional cut on the edge of GDL after assembly (top) and during operation (bottom)
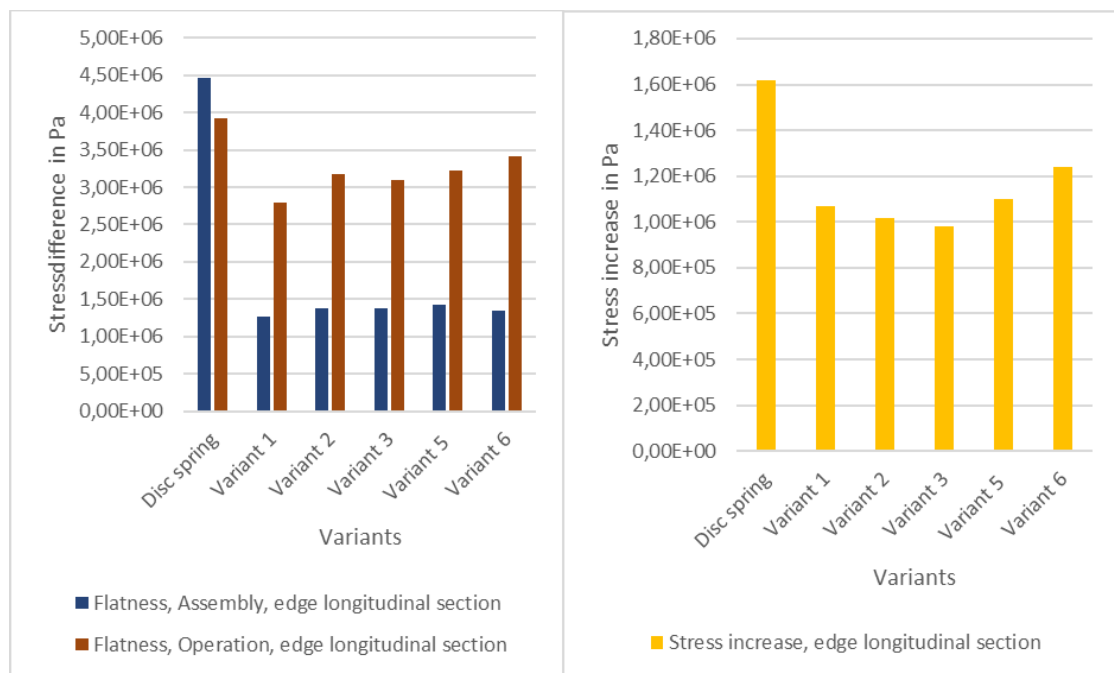
Figure B.2: Flatness of the stress distribution (left) and stress increase (right) on the edge along the longitudinal section

Spring upside down:
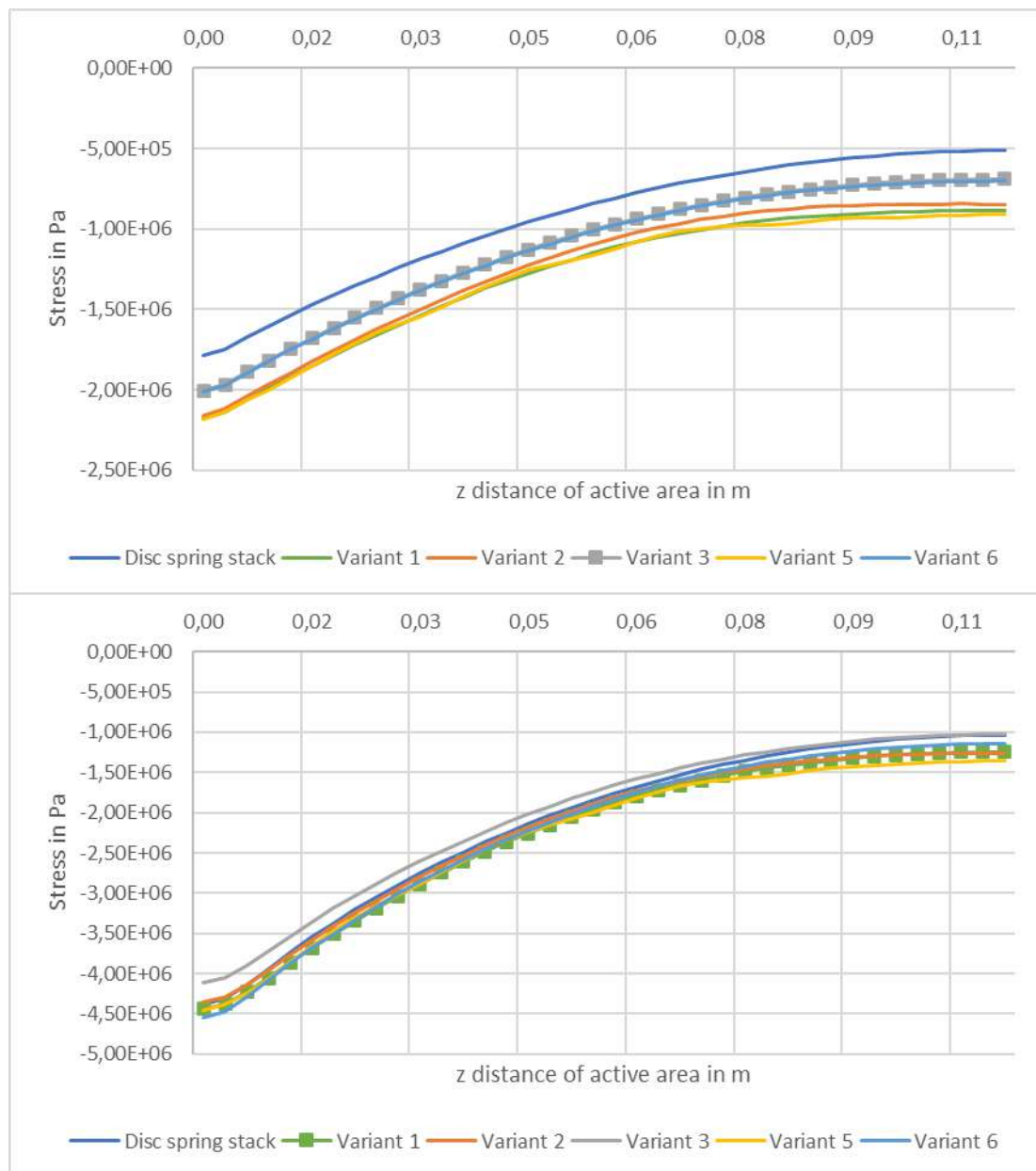
Figure B.3: Stress distribution with the spring upside down in the middle along the longitudinal section after assembly (top) and during operation (bottom)
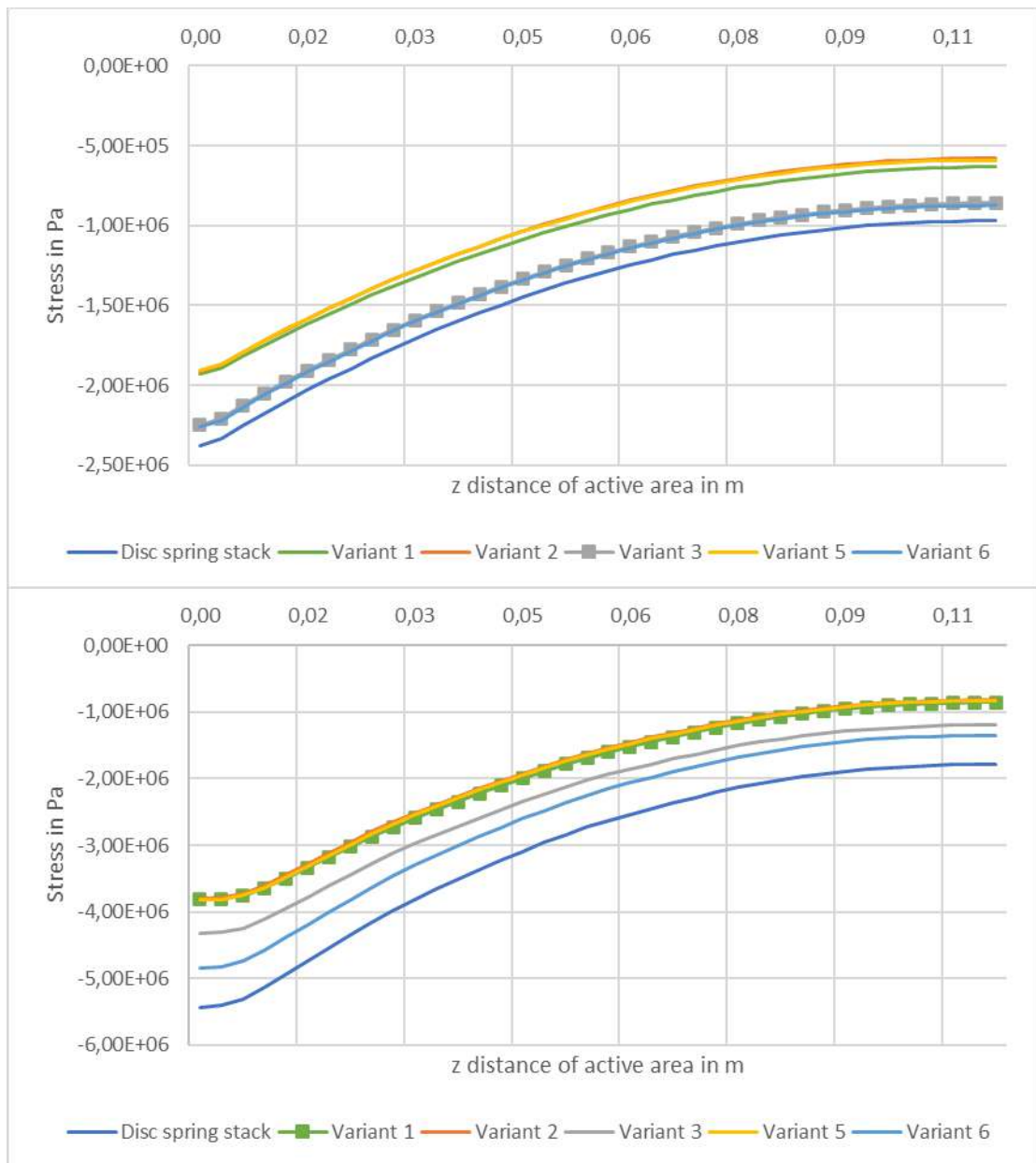
Figure B.4: Stress distribution with the spring upside down on the edge along the longitudinal section after assembly (top) and during operation (bottom)
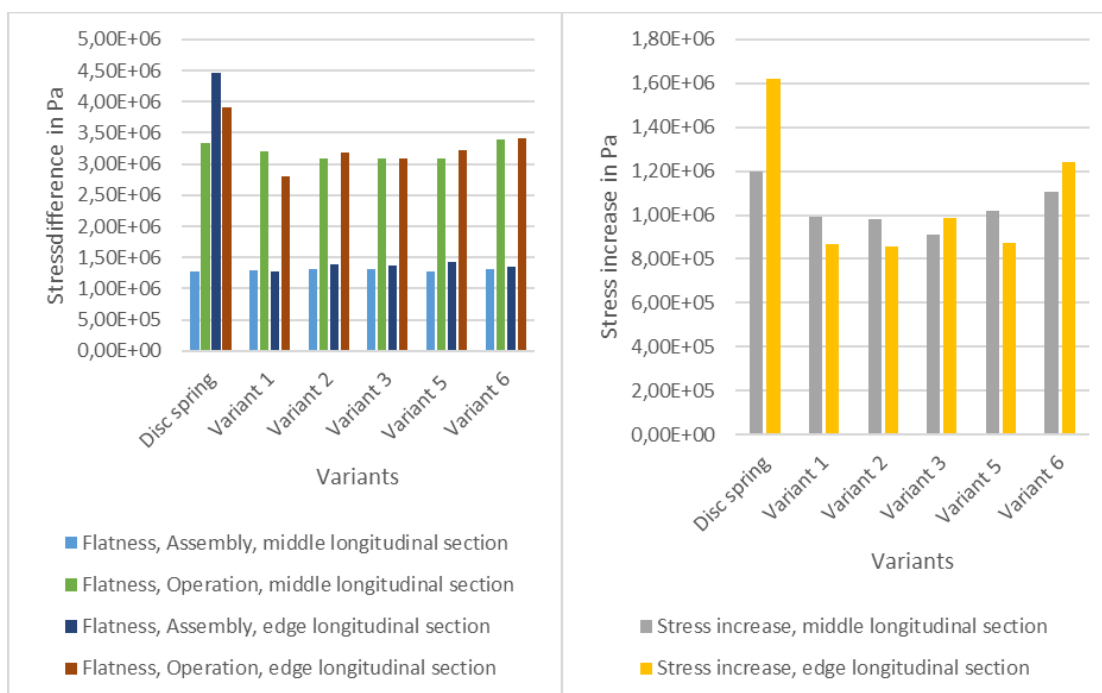
Figure B.5: Flatness of the stress distribution (left) and stress increase (right) with spring up-side down along the longitudinal section

Spring position changed:
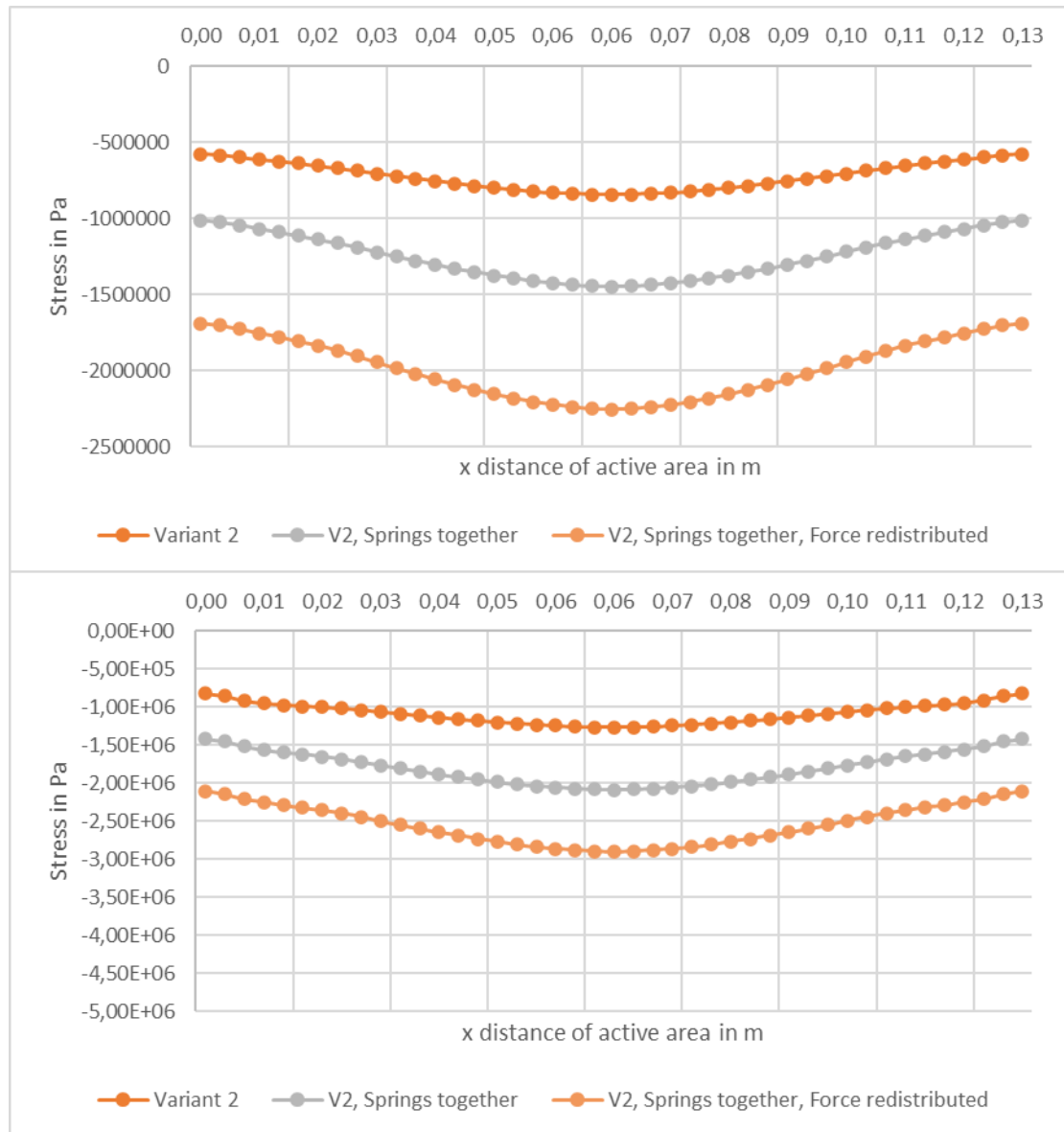
Figure B.6: Stress distribution of modified concept 2 in the cross-section in the middle of the GDL after assembly (top) and during operation (bottom)
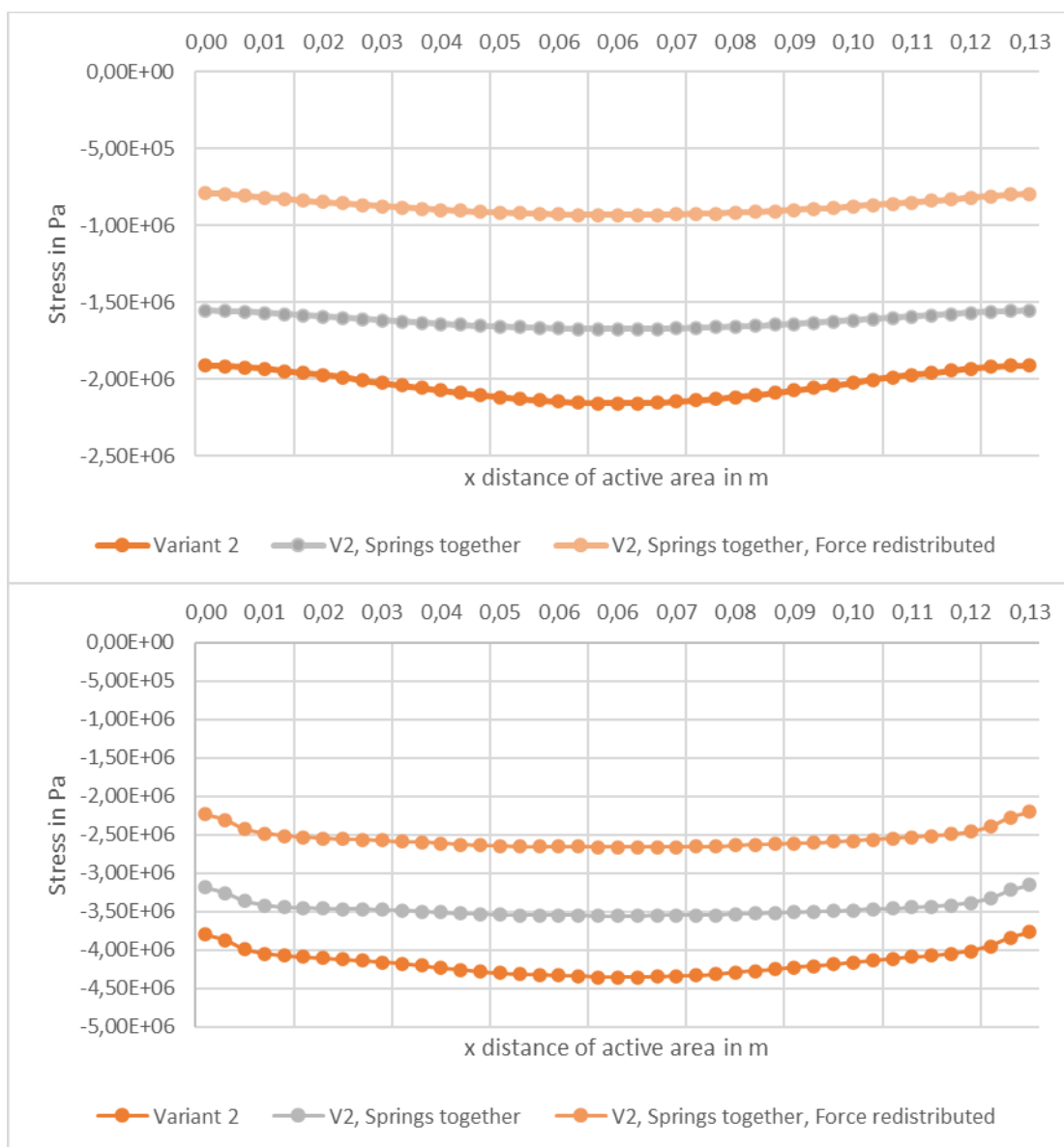
Figure B.7: Stress distribution of modified concept 2 in the cross-section on the edge of the GDL after assembly top) and during operation (bottom)
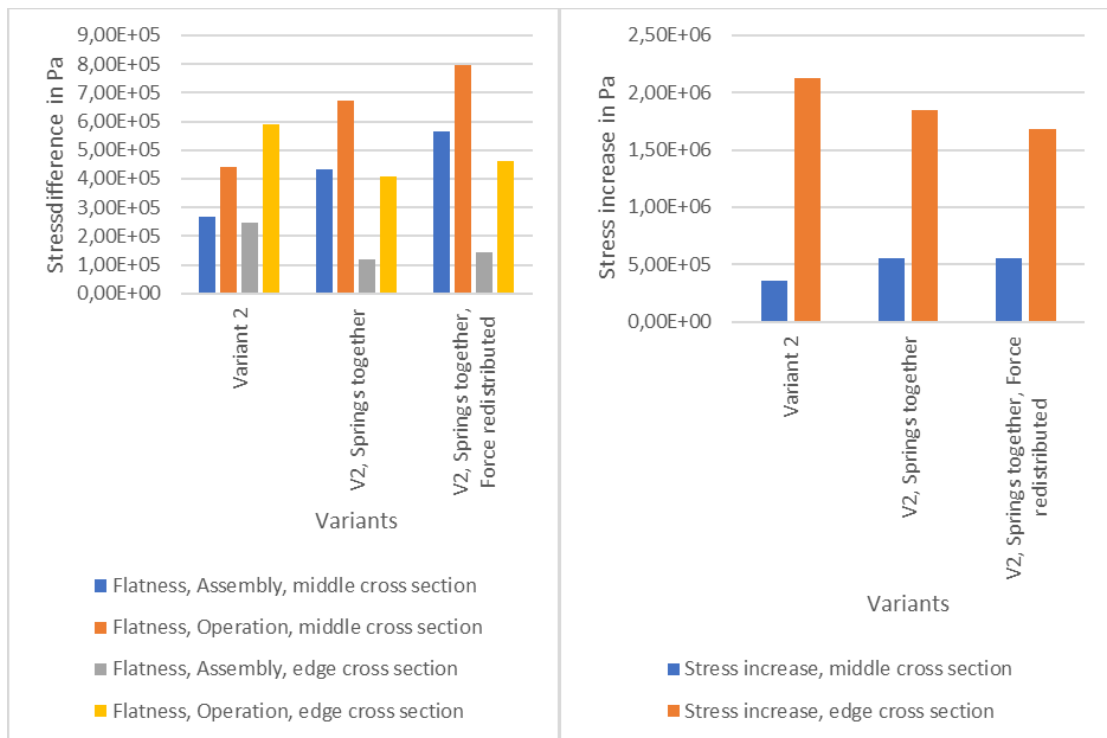
Figure B.8: Flatness of the stress distribution (left) and stress increase (right) with modified concept 2 in the cross-section

Parameter variation:
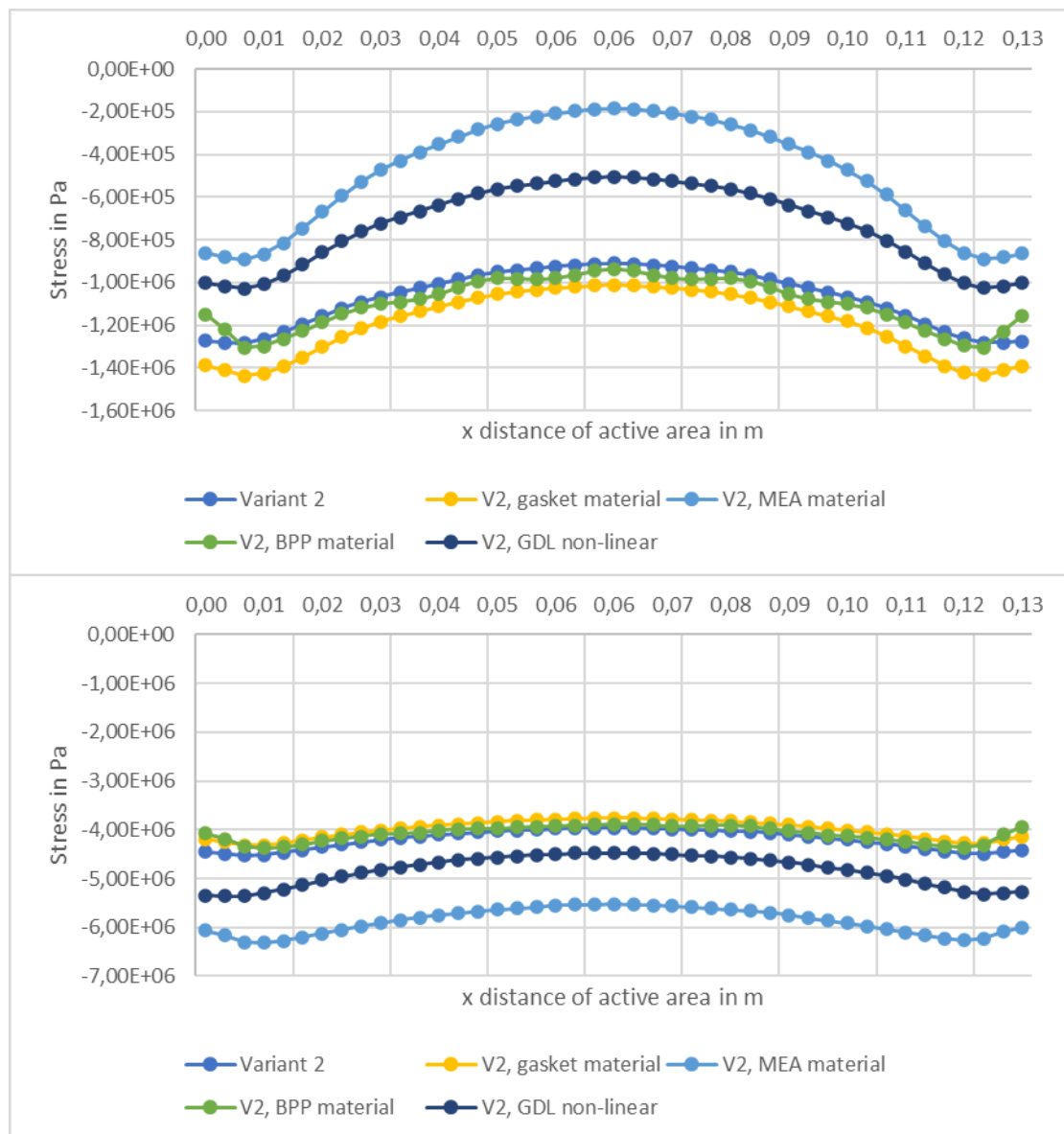
Figure B.9: Stress distribution of parameter variation in the cross-section in the middle of the GDL (top) and on the edge (bottom) during operation

Stiffness change of small springs:
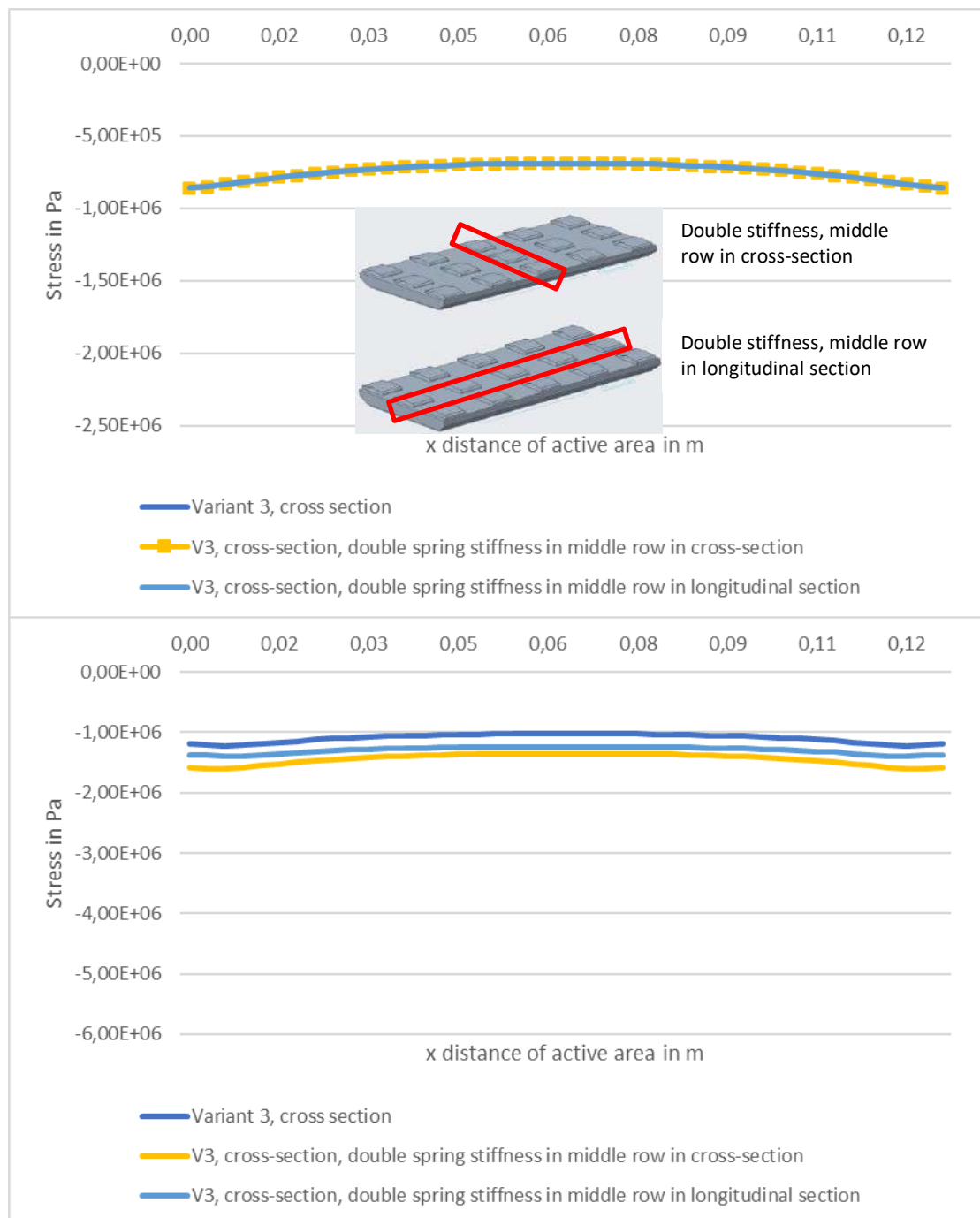
Figure B.10: Stress distribution of stiffness variation in the cross-section in the middle of the GDL after assembly (top) and during operation (bottom)
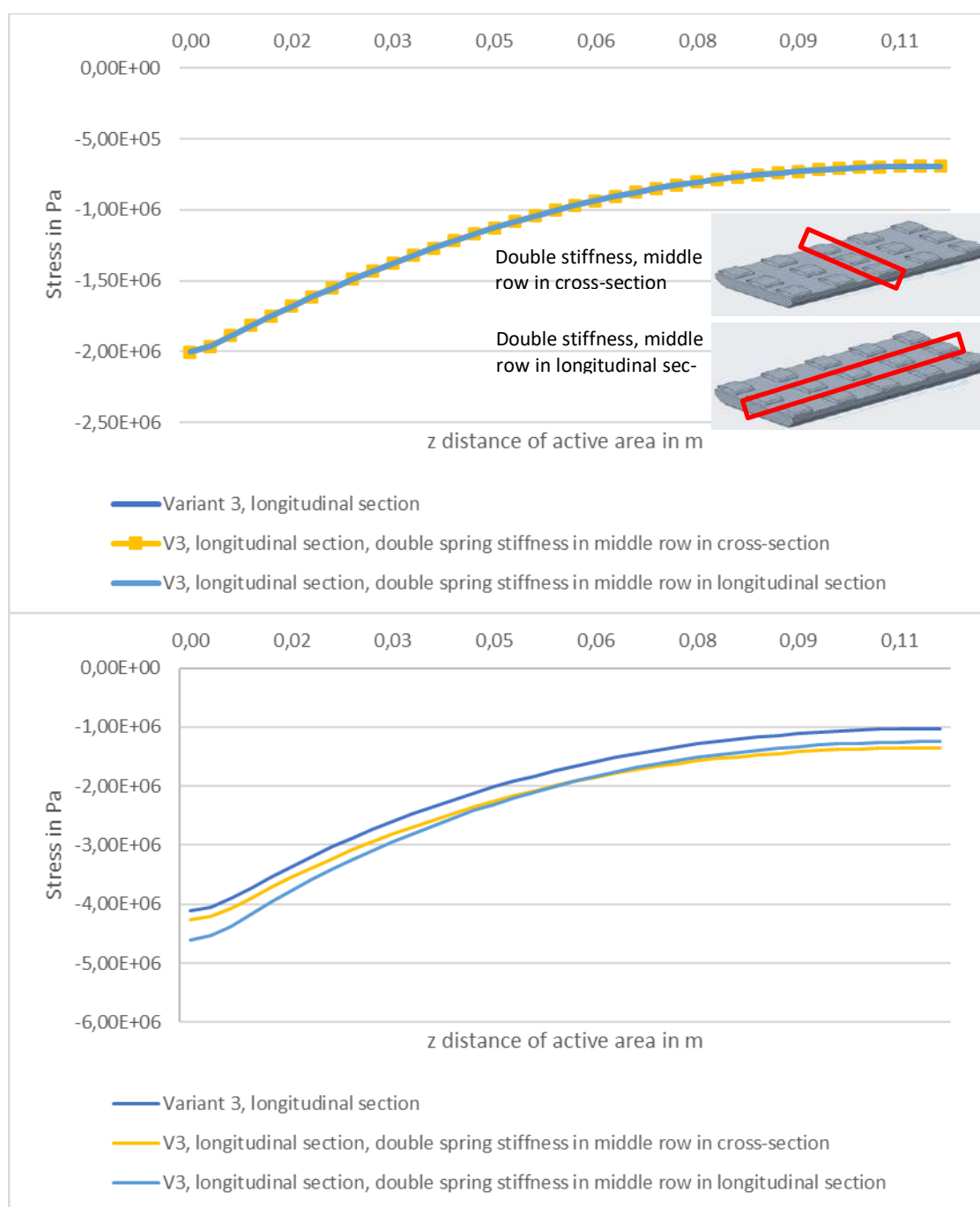
Figure B.11: Stress distribution of stiffness variation in the longitudinal section in the middle of the GDL after assembly (top) and during operation (bottom)

Appendix C

Calculation for new spring force with SR as gasket material

Frame gasket, measured stress when gasket is compressed: 2.4 MPa

$$f_{gasket,frame} = \sigma_{gasket,frame} \cdot A_{gasket,frame} = 2.4 \; MPa \cdot 10 \; mm \cdot 4.8 \; mm = 115.2 \; N \qquad \text{Appendix C.1}$$

Manifold gasket, measured stress when gasket is compressed: 5.1 MPa

$$f_{gasket,manifold} = \sigma_{gasket,manifold} \cdot A_{gasket,manifold} = 5.1 \; MPa \cdot 10 \; mm \cdot 2.9 \; mm \qquad \text{Appendix C.2}$$
$$= 147.9 \; N$$

The total length of the frame gasket is 119.36 cm, of the manifold gasket 111.9 cm. Through that the total force for the compression of the gasket is

$$F_{gasket,frame} = f_{gasket,frame} \cdot l_{gasket,frame} = 115.2 \frac{N}{cm} \cdot 119.36 \; cm = 13\,750 \; N \qquad \text{Appendix C.3}$$

$$F_{gasket,manifold} = f_{gasket,manifold} \cdot l_{gasket,manifold} = 147.9 \frac{N}{cm} \cdot 111.9 \; cm = 16\,550 \; N \qquad \text{Appendix C.4}$$

$$F_{gasket,total} = F_{gasket,frame} + F_{gasket,manifold} = 13\,750 \; N + 16\,550 \; N = 30\,300 \; N \qquad \text{Appendix C.5}$$

With simplified gasket from FEM model (Without gasket radius):

$$F^*_{gasket,frame} = l^*_{gasket,frame,radius} \cdot f_{gasket,frame} = 106.8 \; cm \cdot 115.25 \frac{N}{cm} = 12\,303 \; N \qquad \text{Appendix C.6}$$

$$F^*_{gasket,manifold} = l^*_{gasket,manifold,radius} \cdot f_{gasket,manifold} = 84.8 \; cm \cdot 147.9 \frac{N}{cm} \qquad \text{Appendix C.7}$$
$$= 12\,542 \; N$$

List of figures

List of tables

List of abbreviations

Abbreviation	Meaning
BPP	Bipolar plate
EP	End plate
EPDM	Ethylene propylene diene monomer rubber
FEM	Finite Element Model
GDL	Gas diffusion layer
IPEK	Institute for product development (Institut für Produktentwicklung am KIT)
MEA	Membrane electrode assembly
PEMFC	Polymer electrolyte membrane fuel cell
PFSA	Perfluorosulfonic acid
PTFE	Polytetrafluoroethylene
RH	Relative humidity
RP	Reference point
SR	Silicon rubber

References

[1] M. Klell, H. Eichlseder, and A. Trattner, *Wasserstoff in der Fahrzeugtechnik: Erzeugung, Speicherung, Anwendung,* 4th ed. (ATZ/MTZ-Fachbuch). Wiesbaden, Heidelberg: Springer Vieweg, 2018.

[2] Bundesministerium für Bildung und Forschung, *Nationale Wasserstoffstrategie: Grüner Wasserstoff als Energieträger der Zukunft*, 2023. Accessed: May 4, 2023. [Online]. Available: https://www.bmbf.de/bmbf/de/forschung/energiewende-und-nachhaltiges-wirtschaften/nationale-wasserstoffstrategie/nationale-wasserstoffstrategie.html

[3] European Commission, "A hydrogen strategy for climate-neutral Europe," Brussels, 2020. Accessed: Jun. 16, 2023. [Online]. Available: https://eur-lex.europa.eu/legal-content/EN/TXT/?uri=CELEX:52020DC0301

[4] European Commission, "The European Green Deal," Brussels, 2019. Accessed: Jun. 16, 2023. [Online]. Available: https://eur-lex.europa.eu/legal-content/EN/TXT/PDF/?uri=CELEX:52019DC0640

[5] D. Degler, U. Schelling, and F. Allmendinger, "Brennstoffzellen," in *Energietechnik: Systeme zur konventionellen und erneuerbaren Energieumwandlung. Kompaktwissen für Studium und Beruf* (Lehrbuch), R. Zahoransky et al., Eds., 9th ed. Wiesbaden, Heidelberg: Springer Vieweg, 2022, pp. 299–339.

[6] P. Kurzweil, *Brennstoffzellentechnik: Grundlagen, Materialien, Anwendungen, Gaserzeugung,* 3rd ed. Wiesbaden: Springer Vieweg, 2016.

[7] K. Song *et al.,* "Assembly techniques for proton exchange membrane fuel cell stack: A literature review," *Renewable & sustainable energy reviews*, no. 153, 2022, Art. no. 111777, doi: 10.5445/IR/1000139461.

[8] S. Asghari, M. H. Shahsamandi, and M. R. Ashraf Khorasani, "Design and manufacturing of end plates of a 5kW PEM fuel cell," *International Journal of Hydrogen Energy*, vol. 35, no. 17, pp. 9291–9297, 2010, doi: 10.1016/j.ijhydene.2010.02.135.

[9] R. Banan, A. Bazylak, and J. Zu, "Combined effects of environmental vibrations and hygrothermal fatigue on mechanical damage in PEM fuel cells," *International Journal of Hydrogen Energy*, vol. 40, no. 4, pp. 1911–1922, 2015, doi: 10.1016/j.ijhydene.2014.11.125.

[10] The Chemours Company FC LLC, "Nafion N115, N117, N1110 Ion Exchange Materials," Fayetteville, 2016.

[11] D. Führen *et al.,* "Wertschöpfungskette Brennstoffzelle Metastudie," Berlin, 2022. Accessed: Apr. 25, 2023. [Online]. Available: https://www.now-gmbh.de/wp-content/uploads/2022/08/NOW_Wertschoepfungskette-Brennstoffzelle.pdf

[12] C. Carral, N. Charvin, H. Trouvé, and P. Mélé, "An experimental analysis of PEMFC stack assembly using strain gage sensors," *International Journal of Hydrogen Energy*, vol. 39, no. 9, pp. 4493–4501, 2014, doi: 10.1016/j.ijhydene.2014.01.033.

[13] T. Agaesse, "Simulations of one and two-phase flows in porous microstructures, from tomographic images of gas diffusion layers of proton exchange membrane fuel cells," Toulouse, 2016. Accessed: Apr. 26, 2023. [Online]. Available: https://www.researchgate.net/publication/314087767_PhD_manuscript_-_draft_-_Simulations_of_one_and_two-phase_flows_in_porous_microstructures_from_tomographic_images_of_gas_diffusion_layers_of_proton_exchange_membrane_fuel_cells

[14] C. Spiegel, *Designing and building fuel cells*. New York: McGraw-Hill Professional, 2007.

[15] Y. Wang, D. F. Ruiz Diaz, K. S. Chen, Z. Wang, and X. C. Adroher, "Materials, technological status, and fundamentals of PEM fuel cells – A review," *Materials Today*, vol. 32, pp. 178–203, 2020, doi: 10.1016/j.mattod.2019.06.005.

[16] Fraunhofer IPT and WZL der RWTH Aachen, "Technologischer Deep-Dive | Die Membran-Elektroden-Einheit der PEM-Brennstoffzelle," Oct. 2022. Accessed: Apr. 10, 2023. [Online]. Available: https://www.now-gmbh.de/wp-content/uploads/2022/10/Deep-Dive_MEA.pdf

[17] Y. Tang, A. M. Karlsson, M. H. Santare, M. Gilbert, S. Cleghorn, and W. B. Johnson, "An experimental investigation of humidity and temperature effects on the mechanical properties of perfluorosulfonic acid membrane," *Materials Science and Engineering: A*, vol. 425, 1-2, pp. 297–304, 2006, doi: 10.1016/j.msea.2006.03.055.

[18] S. Escribano, J.-F. Blachot, J. Ethève, A. Morin, R. Mosdale, and J.-F. Blachot, "Characterization of PEMFCs gas diffusion layers properties," Rep. 1, 2006, doi: 10.1016/j.jpowsour.2005.08.013.

[19] L. Jörissen and J. Garche, "Polymerelektrolytmembran-Brennstoffzellen (PEFC) Stand und Perspektiven," in *Wasserstoff und Brennstoffzelle: Technologien und Marktperspektiven*, J. Töpler and J. Lehmann, Eds., 2nd ed. Berlin, Heidelberg: Springer Vieweg, 2017, pp. 263–313.

[20] Z. Zhang, J. Zhang, L. Shi, and T. Zhang, "A Study of Contact Pressure with Thermo-Mechanical Coupled Action for a Full-Dimensional PEMFC Stack," *Sustainability*, vol. 14, no. 14, p. 8593, 2022, doi: 10.3390/su14148593.

[21] P. Jendras, K. Lötsch, and T. von Unwerth, "Strömungssimulation zur Optimierung von Flussfeldern in PEM-Brennstoffzellen," Technische Universität Chemnitz, Chemnitz, 2017. Accessed: Apr. 26, 2023. [Online]. Available: https://monarch.qucosa.de/api/qucosa%3A20723/attachment/ATT-0/

[22] J. Haußmann *et al.,* "GDL and MPL Characterization and Their Relevance to Fuel Cell Modelling," Rep. 17, 2015, doi: 10.1149/06917.1279ecst.

[23] T. Lochner, R. M. Kluge, J. Fichtner, H. A. El‐Sayed, B. Garlyyev, and A. S. Bandarenka, "Temperature Effects in Polymer Electrolyte Membrane Fuel Cells," *ChemElectroChem*, vol. 7, no. 17, pp. 3545–3568, 2020, doi: 10.1002/celc.202000588.

[24] RISE. "Optimizing production process for bipolar plates." https://www.ri.se/en/what-we-do/projects/optimizing-production-process-for-bipolar-plates (accessed Apr. 26, 2023).

[25] Carbongraphiteplate. "Fuel Cell 100Mpa Graphite Bipolar Plate High Strength." https://www.carbongraphiteplate.com/sale-13303267-fuel-cell-100mpa-graphite-bipolar-plate-high-strength.html (accessed Apr. 26, 2023).

[26] A. Kampker, P. Ayvaz, C. Schön, P. Reims, and G. Krieger, "Produktion von Brennstoffzellensystemen," Aachen, 2020, doi: 13140.

[27] E. Alizadeh, M. M. Barzegari, M. Momenifar, M. Ghadimi, and S. Saadat, "Investigation of contact pressure distribution over the active area of PEM fuel cell stack," *International Journal of Hydrogen Energy*, vol. 41, no. 4, pp. 3062–3071, 2016, doi: 10.1016/j.ijhydene.2015.12.057.

[28] C. Carral and P. Mélé, "A numerical analysis of PEMFC stack assembly through a 3D finite element model," *International Journal of Hydrogen Energy*, vol. 39, no. 9, pp. 4516–4530, 2014, doi: 10.1016/j.ijhydene.2014.01.036.

[29] P. Irmscher, *Mechanische Eigenschaften von Polymer-Elektrolyt-Membran-Brenn-stoffzellen* (Energie & Umwelt/Energy & Environment 478). Jülich: Forschungszentrum Jülich GmbH Zentralbibliothek, 2019.

[30] M. Ahmad, R. Harrison, J. Meredith, A. Bindel, and B. Todd, "Validation of a fuel cell compression spring equivalent model using polarisation data," *International Journal of Hydrogen Energy*, vol. 42, no. 12, pp. 8109–8118, 2017, doi: 10.1016/j.ijhydene.2017.01.216.

[31] H. Kikuchi, S. Sugiura, and Y. Wariishi, "Fuel cell stack," US 2002/142209 A1.

[32] B. Andreas-Schott, G. W. Fly, J. A. Rock, and I. R. Jermy, "Fuel cell stack compression retention system with external springs," US 7807316 B2.

[33] J. Yang, "Fuel cell with uniform compression device," US 2002/0110722 A1.

[34] J. Scholta and F. Häußler, "Generischer Brennstoffzellenstack: Konzeption einer generischen Brennstoffzelle, die eine Vergleichbarkeit der vorwettbewerblich erzielten Forschungsergebnisse ermöglicht," Zentrum für Sonnenenergie- und Wasserstoff-Forschung, Frankfurt am Main, 2020.

[35] X. Wang, Y. Song, and B. Zhang, "Experimental study on clamping pressure distribution in PEM fuel cells," *Journal of Power Sources*, vol. 179, no. 1, pp. 305–309, 2008, doi: 10.1016/j.jpowsour.2007.12.055.

[36] E. Borgardt, *Mechanische Eigenschaften von katalysatorbeschichteten Membranen für die Polymer-Elektrolyt-Membran Elektrolyse* (Energie & Umwelt/Energy & Environment 533). Jülich: Forschungszentrum Jülich GmbH Zentralbibliothek, 2021.

[37] Freudenberg. "Power für nachhaltige Energie: Dichtungslösungen für die gesamte Energiewertschöpfungskette." https://www.fst.com/de/sealing/maerkte/energy/hydrogen/ (accessed May. 4, 2023).

[38] Z. Zhang *et al.,* "Arrangement of Belleville Springs on Endplates Combined with Optimal Cross-Sectional Shape in PEMFC Stack Using Equivalent Beam Modeling and FEA," *Sustainability,* vol. 14, no. 23, 2022, doi: 10.3390/su142315928.

[39] A. Bendzulla, *Von der Komponente zum Stack: Entwicklung und Auslegung von HT-PEFC-Stacks der 5 kW-Klasse* (Energie & Umwelt/Energy & Environment 69). Jülich: Forschungszentrum Jülich GmbH Zentralbibliothek, 2010.

[40] Solon Manufacturing Co. "Washers for hydrogen fuel cell stacks." https://www.solonmfg.com/hydrogen-fuel-cells (accessed May. 4, 2023).

[41] Spirol. "Pre-stacked disc springs for fuel cells & electrolyzers." https://ca.spirol.com/assets/files/disc-fuel-cell-electrolyzer-flyer-us.pdf (accessed May. 4, 2023).

[42] Schnorr. "Wasserstoff." https://www.schnorr-group.com/de/green-technology/green-energy/wasserstoff (accessed May. 4, 2023).

[43] B. Seth, J. Knaier, S. Knecht, and J. Haußmann, "Investigation of scaled-down fuel cell system components by means of the IPEK X-in-the-loop approach," 19th Syposium on Fuel Cell and Battery Modeling and Experimental Validation (ModVal), Duisburg.

[44] W. L. Gore & Associates Inc., "Driving fuel cell industry change," Elkton, 2023. Accessed: May 18, 2023. [Online]. Available: https://www.gore.com/system/files/2023-03/AES02-R1-Fuel-Cell-Portfolio-DSH-EN-JUN22-e.pdf

[45] Toray. "Torayca Carbon Paper für Brennstoffzellen." https://toray-cfe.com/de/produkte/carbon-paper/ (accessed May. 18, 2023).

[46] S. Melito. "Gasket Compression Explained." https://www.elastoproxy.com/enclosure-gasket-compression/ (accessed May. 18, 2023).

[47] CMC Klebetechnik GmbH. "Technisches Datenblatt CMC 61325." https://nx5412.your-storageshare.de/s/gnHdEFMgaGQRnYB (accessed Jun. 30, 2023).

[48] T. J. Mason, J. Millichamp, T. P. Neville, P. R. Shearing, S. Simons, and D. J. Brett, "A study of the effect of water management and electrode flooding on the dimensional change of polymer electrolyte fuel cells," *Journal of Power Sources*, vol. 242, pp. 70–77, 2013, doi: 10.1016/j.jpowsour.2013.05.045.

[49] A. Albers, N. Bursac, and E. Wintergerst, "Produktgenerationsentwicklung - Bedeutung und Herausforderungen aus einer entwicklungsmethodischen Perspektive," 2015.

[50] Spirol, "Tellerfedern," München, 2020. Accessed: May 26, 2023. [Online]. Available: https://de.spirol.com/assets/files/dsc-tellerfedern-konstruktionsrichtlinien-de.pdf

[51] Y. Liu, M. Kohrn, M. Wick, and S. Pischinger, "Optimization of the bipolar plate rib structure in proton exchange membrane fuel cells with an analytical method," *International Journal of Hydrogen Energy*, vol. 47, no. 40, pp. 17683–17698, 2022, doi: 10.1016/j.ijhydene.2022.03.108.

[52] Y. Tang, M. H. Santare, A. M. Karlsson, S. Cleghorn, and W. B. Johnson, "Stresses in Proton Exchange Membranes Due to Hygro-Thermal Loading," *Journal of Fuel Cell Science and Technology*, vol. 3, no. 2, pp. 119–124, 2006, doi: 10.1115/1.2173666.

[53] M. Zhang, Y. Liu, Y. Qin, T. Zhang, X. Han, and Y. Wang, "Effects of membrane swelling on structural deformation and performance of proton exchange membrane fuel cell," *International Journal of Green Energy*, pp. 1–7, 2022, doi: 10.1080/15435075.2022.2155967.

[54] Y. Zhou, G. Lin, A. J. Shih, and S. J. Hu, "Assembly pressure and membrane swelling in PEM fuel cells," *Journal of Power Sources*, vol. 192, no. 2, pp. 544–551, 2009, doi: 10.1016/j.jpowsour.2009.01.085.

[55] M. Fiedler, K. Kittner, and B. Awiszus, "Production of Metallic Bipolar Plates Made of Stainless Steel by Incremental Hollow Embossing Using Rollers," in *The 28th Saxon Conference on Forming Technology SFU and the 7th International Conference on Accuracy in Forming Technology ICAFT*, 2022, p. 15, doi: 10.3390/engproc2022026015.

[56] P. Yi, L. Peng, X. Lai, and J. Ni, "A Numerical Model for Predicting Gas Diffusion Layer Failure in Proton Exchange Membrane Fuel Cells," *Journal of Fuel Cell Science and Technology*, vol. 8, no. 1, 2011, Art. no. 011011, doi: 10.1115/1.4002312.

[57] P. A. García-Salaberri, M. Vera, and R. Zaera, "Nonlinear orthotropic model of the inhomogeneous assembly compression of PEM fuel cell gas diffusion layers," *International Journal of Hydrogen Energy*, vol. 36, no. 18, pp. 11856–11870, 2011, doi: 10.1016/j.ijhydene.2011.05.152.

[58] L. Butenschön. "3 technische Kenngrößen, die bei keiner Lagerauswahl fehlen sollten." https://blog.igus.de/3-technische-kenngroessen-die-bei-keiner-lagerauswahl-fehlen-sollten/ (accessed Jun. 5, 2023).

[59] D. Qiu, P. Liang, L. Peng, P. Yi, X. Lai, and J. Ni, "Material behavior of rubber sealing for proton exchange membrane fuel cells," *International Journal of Hydrogen Energy*, vol. 45, no. 8, pp. 5465–5473, 2020, doi: 10.1016/j.ijhydene.2019.07.232.

[60] L. F. Peng, D. K. Qiu, P. Y. Yi, and X. M. Lai, "Investigation of Thermal Influence on the Assembly of Polymer Electrolyte Membrane Fuel Cell Stacks," *AMR*, vol. 512-515, pp. 1509–1514, 2012, doi: 10.4028/www.scientific.net/AMR.512-515.1509.

[61] A. Kusoglu, A. M. Karlsson, M. H. Santare, S. Cleghorn, and W. B. Johnson, "Mechanical behavior of fuel cell membranes under humidity cycles and effect of

swelling anisotropy on the fatigue stresses," *Journal of Power Sources*, vol. 170, no. 2, pp. 345–358, 2007, doi: 10.1016/j.jpowsour.2007.03.063.

[62] R. Schweiss *et al.,* "Powering up fuel cells: Our gas diffusion layer," SGL Carbon GmbH, Meitingen, 2021.

[63] J.-S. Kim *et al.,* "Fuel Cell End Plates: A review," *International Journal of precision engineering and manufacturing*, vol. 9, no. 1, pp. 39–46, 2008.

[64] A. Bates *et al.,* "Simulation and experimental analysis of the clamping pressure distribution in a PEM fuel cell stack," *International Journal of Hydrogen Energy*, vol. 38, no. 15, pp. 6481–6493, 2013, doi: 10.1016/j.ijhydene.2013.03.049.